Structural and Flow Relationship of Microfluidics Pulsating High and Low Frequency Jets

A Thesis

by

Muhammad Ikhlaq

Submitted to the
Graduate School of Science and Engineering
In partial fulfillment of the requirement for
the degree of

Master of Science

In the
Department of Mechanical Engineering

Özyeğin University
June 2015

Structural and Flow Relationship of Microfluidics Pulsating High and Low Frequency Jets

Approved by:

Associate Professor Mehmet Arık, Advisor
Department Mechanical,
Engineering
Özyeğin University

Assis Prof Dr. Özgür Ertunç
Department of Mechanical,
Engineering
Özyeğin University

Assis Prof Dr. Güney Güven Yapıcı
Department of Mechanical,
Engineering
Özyeğin University

Assis Prof Dr. Altuğ Başol
Department of Mechanical,
Engineering
Özyeğin University

Assis. Prof. Dr. Sezer Seckin Erder
Department of Mechanical,
Engineering
Istanbul University

Date Approved: 23 June 2015

To my family, friend and teacher

ABSTRACT

Synthetic jets are being investigated last several years. Researchers have been interested in its unique applications for a wide range of flow control to thermal management of electronics applications. Synthetic jets are made up of actuators such as piezoelectric, magnetic, or linear piston technology etc.

Piezoelectric synthetic jets are investigated and found relationship between its structural and flow parameter like deflection, frequency and resonance with velocity and heat transfer enhancement. In order to find a relationship some numerical and experimental techniques are being used. For experimental result and fully-automated experimental setup made using high end equipment like Laser Vibrometer, Hotwire anemometer and 3D robot. Four different type of measurement were made on synthetic jet actuators deflection, heat transfer, velocity measurements and power consumption. The heat transfer enhancement factor of each of these jets with respect to natural convection is measured over a 25.4x25.4 (mm) vertical heater. Finally, power consumption of the low and high frequency synthetic jets were measured and compared. It is found that disk deflection and operating frequency are directly related to heat transfer enhancement factor, if the Helmholtz frequency of a cavity has no effect on the performance of a jet.

For numerical analysis commercially available software are used like Ansys and Comsol. Eigen frequency and transient deflection is modeled using Comsol 4.0 and different mode shapes and deflection measurements using PZD module of Comsol. A 3-D computational fluid dynamics model was constructed using Ansys CFX to determine the flow and temperature fields of a meso-scale central orifice synthetic jet at a nozzle-to-target surface spacing of y/d = 2, ReD_j = 1400 and f = 500 Hz. Unlike the majority of

previous computational studies, rather than specifying the boundary conditions at the nozzle, the flow inside the synthetic jet device was solved by specifying the time dependent boundary conditions on the vibrating diaphragm and utilizing the moving mesh technique. Local surface pressure and heat transfer coefficient distributions were determined and discussed. It was found that the pulsating flow at the nozzle exit for a round jet generates vortex rings and these rings seem to have some considerable effects on the target surface profiles. Finally figure out the design parameters for Synthetic jet actuator for the optimum performance.

ÖZETÇE

Son zamanlarda sentetik jetlerin uygulanması üzerine araştırmalar yapılmaktadır. Sentetik jetlerin kendilerine özel sağladıkları geniş akış kontrolü ile elektroniklerde termal performansın artırılması konusunda araştırmacıların ilgisini çekmektedir. Sentetik jetler basit olarak piezo elektrik yada magnet gibi tetikleyiciler ile yapılmaktadır.

Geliştirilen piezo elektrik sentetik jetler için yapısal ve akış parametreleri (bükülme, frekans, akış hızına göre rezonans, ve ısı atımında performans artışı gibi) arasında bir ilişki elde edilmiştir. Özellikle ısı atımında performans artışı hedeflenen sentetik jetlerde ki bu etkin parametreler arasındaki ilişkinin en doğru şekilde kurgulanabilmesi için sayısal ve deneysel methodlar kullanılmıştır.

Deneysel methodların uygunlanması için lazer titreşim cihazı, sıcak kablo ile hız ölçer ve 3 boyutlu robot gibi üst düzey cihazlar eşliğinde deneysel sistem kurulmuştur. Sentetik jetlerde bükülme, ısı atımı, akış hız ölçümü ve enerji tüketimi olmak üzere dört tür hesaplama yapılmıştır. Yapılan jetlerin ısı atım performans faktörü, daha önceden kayıpları hesaplanmış olan 25.4x25.4 (mm)'lik dikey bir ısıtıcı yüzeyinden hesaplanmıştır. Son olarakta, düşük ve yüksek frekansta çalıştırılan jetlerin enerji tüketimleri hesaplanmış ve kıyaslanmıştır.

Sayısal method Ansys ve Comsol programları ile yapılmıştır. Zamana bağımlı bükülme testleri Comsol da yapılırken, 3 boyutlu akış ve termal dağılım simülasyonları (Jet nozulu ile ısıtıcı yüzeye arası başluk oranı y/d = 2, ReDj = 1400 ve f = 500 Hz için) Ansys CFX'te yapılmıştır. Bölgesel basınç ve ısı atım katsayısı elde edilmiş ve titreşimli akışların (pulsating flow) jet nozul çıkışında vorteks halkası oluşturduğu ve bu vorteksin önemsenecek boyutta sonuca etkisi gözlemlenmiştir. Sonuç olarak bir sentetik jet tetikleyicisinin performans sağlayabileceği dizayn parametreleri ortaya çıkartılmıştır.

ACKNOWLEDGEMENT

Financial support for the research project was provided by a Turkish National Science Foundation (TUBITAK) under the contract number 112M154. First, I would like to thank my advisor, Associate Professor Dr.Mehmet Arık. His continual guidance and support gave me the motivation and encouragement that made this work possible. I would also like to express my gratitude especially Dr.Mehmet Baris Dougroz, Enes Tamdogan, Omidreza Ghaffari and to other members of ART group. Author also wants to thank Professor Aydın Doğan being collaborator of this project.

Finally, thanks go to my family and friends, from the Turkey and from Pakistan, for always encouraging me to pursue my interests and for making that pursuit possible, Special thanks Almighty Allah and His beloved Prophet (Peace Be Upon Him) who hold my hand trough out my life and gave me beyond my expectation and my teacher Muhammad Ashraf who gave me the new way of thinking

TABLE OF CONTENTS

LIST OF FIGURES

LIST OF TABLES

NOMENCLATURE

S	Strain	
s	Compliance	(1/Pa)
σ	Stress	(N/m^2)
G^k	Converse piezoelectric effect	
K	Transpose of a matrix	
M	Electric field strength	
B	Stress field strength	
C	Electric charge density	
f	Frequency	(Hz)
f_d	Structural resonance frequency	(Hz)
f_h	Helmholtz resonance frequency	(Hz)
E	Modulus of elasticity	(GPa)
r	Position from center of diaphragm	(m)
R	Radius of diaphragm	(m)
L	Radius of cavity	(m)
l	Thickness of diaphragm	(m)
N	Flexure rigidity	($Pa.m^3$)
c	Speed of sound	(m/s)
H	Cavity height	(m)
d	Orifice/Nozzle diameter	(m)
V	Applied voltage	(Volts)
Z	Distance between jet and heater	(m)
D	Deflection	(m)
D_j	Maximum deflection of diaphragm	(m)

V_c	Cavity volume	(m3)
A	Area of orifice	(m2)
h	Heat transfer coefficient	(W/m2-K)
k	Thermal conductivity	(W/m-K)
m	Mass	(kg)
t	time	(s)
T	Temperature	(K, ^{0}C)
T_{amb}	Ambient temperature	(K, ^{0}C)
Cp	Pressure coefficient, $c_p = \frac{P-P_{amb}}{0.5\rho u_j^2}$	
P	Pressure	(Pa)
Pst	Stagnation pressure	(Pa)
u_r	Velocity in radial direction	(m/s)
$\bar{u}_j$	Average jet exit velocity	(m/s)
x	Streamwise coordinate	(m)
y	Wall-normal direction (2d)	(m)
Q_{total}	Total heat given to heater	(Watt)
Q_{heater}	Heat from front surface	(Watt)
Q_{loss}	Heat from plexiglas	(Watt)
Nu	Nusselt number	
Re	Reynolds number	
St	Stokes number	
Stk	Strouhal number	
COP	Coefficient of performance	
EF	Enhancement factor	

M, F	Constants	

Greek Symbols

$\alpha,\beta, \gamma, \kappa, \nabla$	Coefficient for correlation	
μ	Kinematic viscosity	(m^2/s)
ρ	Density	(Kg/m^3)
ϵ	Permittivity	(F/m)
ν	Poisson ratio	
ω	Operating frequency	(Radian)
φ	Phase angle	(Degrees)

CHAPTER I

1. INTRODUCTION

1.1. Motivation

Continuous advancement in computing power of electronic devices with reduction in overall size because of advance technologies available for manufacturing leads towards the very heat fluxes [1]. The endlessly increasing heat flux requires development of novel thermal management technologies. Liquid cooling method like spray and evaporative cooling are being used for high flux thermal problems, and they can have high potential for further cooling of the equipment. Air cooling still is the choice of many cooling application because of low cost and availability.

For the last several years, synthetic jets also known as Zero-Net Mass Flux(ZNMF) systems have been examined as a substitute for fan as air blowing devices and shown as an extremely effecting for thermal cooling of electronics with occupying smaller space. Figure 1, shows the schematic diagram for a synthetic jet flow. A periodic ejection and suction through an orifice backing by a cavity, cyclic motion with respect to time of a diaphragm which is one side wall of the cavity. A distinct feature of these kinds of jets is their working fluid. They are using local air surrounded them as a working fluid. No need for an extra environmental condition for these devices. Distinct from typical jets, synthetic jets are by default produce flow without adding any mass to the system and there is no need for the complex sanitation for it [2], and their exclusive qualities make them first choice fluidic actuators for many application from thermal management to flow control applications.

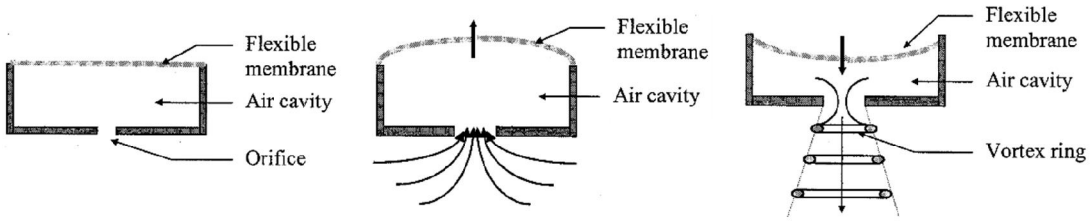

Figure 1: General flow behaviors in a standard synthetic jet [3]

Over the last few years, synthetic jets were evaluated experimentally and computationally for a broad range of time and length scales for different Reynolds numbers, formation frequencies, slit widths, and stroke lengths. Effects of the orifice shapes were also examined closely. The velocity and vorticity field observed for different for long side of jet orifice and for small side. The aspect ratio effect is also examined for the development of synthetic jet. Detailed literature review is made in following section for synthetic jets and piezoelectric actuators

1.2. Literature Review for Piezoelectric Actuator

Some classes of crystalline material have properties of piezoelectricity such as Rochelle salt and Tourmaline which are natural crystals of Quartz. These materials can also be manufactured into Lead Zirconate Titanates (PZT) and ceramics such as Barium Titanate and or plastics such as PolyVinyliDene Fluoride (PVDF). Vvoltage is produced proportional to the pressure from the crystalline structure of the piezoelectric material when a mechanical pressure is applied. On the contrary, when an electric field is deployed, deflection is produced and creating the dimensional change in material. Piezoelectric materials can thus be used as either an actuator or a sensor. Their applications range from simple buzzers and furnace igniters to cell phones, vibration

dampening and medical imaging devices. New designs, materials, and refined fabrication process for manufacturing have improved the performance of these devices.

The constant advancement in the field of piezoelectric materials, has been beneficial for the improvement of synthetic jets [4]–[8]. When equated with other typical possible control devices (i.e. speakers and air pumps), piezoelectric actuators have priority for having less response time, shrunk in weight and size, good availability and low prices [4]–[8]. Chen et al. [9], [10] have achieved a peak air jet velocity of around 40 m/s using a 23 mm diameter 7BB-50M-1 Murata piezoelectric attached with 50mm brass shim powered with a sine wave at 1160 Hz. It is shown in their study that for some asymptotic cases peak to peak displacement of actuators may be scaled.

Studies such as the ones mentioned above and many others that utilize a sinusoidal wave drive input require high frequencies relatively match to the actuator's frequency resonance or the cavity's Helmholtz frequency. Helmholtz frequency is the natural frequency that fluid tends to oscillate into and out of a container dependent on the area opening, cavity volume and length of the opening port. The high frequency which is required to form a synthetic jet physically bound the deflection amplitude of the diaphragm and consumes more power that in turn limits the amount of displaced air volume. Furthermore, the operating frequency is limited to a narrow resonance peak to give enough actuator displacement. The performance of three piezoelectric actuators is currently being explored by Mossi et al [5]–[8] they are the Bimorph, Thunder@ and RFD. Circular actuators with a diameter of 6.35 cm and with a piezoelectric active element of PZT-5A (Lead Zirconate Titanate) are the same as those actuators. Simple design and characteristics of free displacement made piezoelectric actuator to implement in attractive designs. The focus of their study was based on the two actuators, Bimorph

and Thunder. The Bimorph model T2 16-A4NO-573X is manufactured by Piezo Systems Inc., havea maximum capacitance of 130nF and made up of two bounded layers of piezoelectric material with nickel electrodes with a thickness of 4.1 mm. A unimorph made up of three layers 0.254 mm thick of stainless steel, PZT-5A and copper sandwich with layer of polyamide between each material [5]–[8]. Many studies are available on synthetic jets, Bimorphs, and Thunder actuators.

1.3. Literature Review of Synthetic Jets

As the size of electronic devices has continued to shrink and circuit densities have increased accordingly, thermal management of these devices has become more challenging. This problem is expected to worsen in the foreseeable future. Thus, within the next decade, spatially averaged heat fluxes in microprocessor devices are projected to increase by a several times higher, so that a number of different techniques have been studied, and there are still new technologies getting investigated for better solutions on thermal management problems especially in microprocessor devices.

In the past, thermal management was often addressed through the use of forced convective air cooling, either un-aided or in a combination with various heat sink devices and accomplished through the use of fans. However cooling systems having fan embedded was found to be undesirable [11] because of interference of electromagnetic fields and noise generated. Moreover, the use of fans also requires relatively large moving parts, and corresponding high power inputs, in order to achieve the desired level of heat transfer. Thereafter, thermal management systems have been developed which utilize synthetic jet ejectors, which are more energy efficient [12], and also offer reduced levels of noise and electromagnetic interference. Thus the idea of synthesizing a turbulent flow

became an interesting area for researchers. Thereafter a number of studies have been done on the formation of synthetic jets, vortices generation and actuator strategies.

Previously, an overview of generating fluid streams is summarized by Lighthill in 1978 under two different methods [13]. Pressure wave transmission through compressible flow is one of the methods. The viscous effect at the boundary can generate streaming motion and to the generation of vortices within the fluid without addition of fluid into the system. An application of mechanism of fluid mixing where primary consideration is mixing efficiency and cost synthetic jet become suitable choice. Thus, the fluid streams of mixing properties have been simultaneously examining the behavior of pulsating jet flows, which are called as 'fully pulsed jet' and which is superimposed oscillations periodic flow on a continuous mean stream. So that a synthetic jet can also be considered as a special case of jet flow created by pulses and mean of a velocity is zero since only pulsing action is generating flow

Moreover, a zero net mass flow jet also created using circular piezoelectric actuators were investigated by James, Jacobs and Glezer in 1996 [14]. In Glezer's work, a water submerged piezoelectric diaphragm was used to produce synthetic jet flow. However, at the diaphragm surface cavitation bubbles were formed that caused the oscillation. Synthetic jet was only generated when the amplitude of those oscillations was high. The bubble formation and collapsing caused the formation of periodic jet. For similar Reynolds number, typical jet has more dispersion as compare the synthetic jets, but they found self-similar mean profiles for both.

Another research done again by Glezer with Smith in 1997, they showed that partially closed cavity with an opening (orifice) with an internal actuator can enhance the formation of synthetic jet [15]. They mentioned that behavior of flow can be manipulated

by using pairs of synthetic on one or the other side of flow. Generation of pluses in the shear layer with unstable frequencies with higher magnitude can generate amplifies nonlinear disturbance. Thereafter, centerline velocity's evolution was investigated by using hotwire probes by Kral et al. in 1997 [16]. The jets were investigated numerically. They examined the behavior of fully pulsed and steady jet was compared with 2D turbulent and laminar zero net jets. Time-averaged momentum for the pulse jet is used for half period only in order to classify the jets. Flow inside the cavity was not computed instead of that a periodic velocity boundary condition was applied at the orifice and different velocity distributions at orifice were examined. A sequence of laminar vortex pairs were observed from the computed flow structure identified from the vorticity fields at low source Re numbers. Although, the only mean velocity profiles agreed qualitatively with the experimental results of Glezer and Smith. Thereafter the domain of synthetic jet simulations were extended to three dimensions in an attempt to match more closely the physics of the fluid mechanism in the experiments of Smith & Glezer [15].

Two-dimensional studies are been presented by Smith & Glezer [15] and Smith in 1999 [17], over a flat plate with an orifice. Synthetic jet formed normal to the orifice. The jets are created by the advection of train of subsequent time-periodic counter rotating vortex pairs. Vortices are generated at the outlet of orifice entertain by the diaphragm. Conventional jets and synthetic jets are quite similar at the far field, and substantial difference can be seen only at the near field region [18]. In particular, owing to the suction flow, the time-averaged static pressure near the exit plane of a synthetic jet is calculated as lower than the ambient pressure, thus it is clarified that both the streamwise and cross-stream velocity components reverse their direction during the actuation cycle.

In 2003, miniaturized synthetic jet (micro jet) technology was studied by Dan S. Kercher et al. [19] to explain the feasibility of small synthetic jets in the area of microelectronic devices for thermal management. Different aspects of synthetic jet cooling were discussed and turbulent jet was produced with a classification of excitation elements. Thereafter, number of geometries, driving elements, turbulent jets and different configurations were tested and optimized. A Comparison of cooling fan was also pointed out with respect to pulsating jet. The synthetic jet in use consists of a cavity, bounded on one side by an orifice, and on the other side by a flexible membrane. When flexible membrane is vibrated by a suitable driver, air is drawn into the cavity through the same orifice and ejected out of the cavity through the same orifice, forming a series of vortex rings which propagate away from the orifice, each under its own self-induced velocity. A typical construction of synthetic jet is enclosed by an orifice plate with a flexible membrane on the other side with a spacer between them. Flexible membrane driven by using different drivers can be selected on according to application. Vibration of membrane draws air through the orifice. A series of vortex rings forms and travel away from the orifice with some own self-induced velocity. As a result, commercially available electronic fans are analogous to the synthetic jet cooler, but devices based on synthetic jet can have less local hot-spots as compare to conventional fans.

However, piezoelectrically generated synthetic jet flows are investigated by Robert Bryant et al in 2005 [20]. Piezoelectric diaphragm is a good choice for the synthetic jets, since they have small in size, fast response time, and low power consumption as compared to other actuators. In Bryant study a bimorph diaphragm is used as the actuator. The aim of the study is to analyze the feasibility of these devices to create change in flow over bluff body. Measurements were made in a cross flow over a body for which a model

based on an airfoil section is constructed and equipped with two synthetic jet cavities. The actuators are driven using a signal generator. Driving frequency, waveform type, and applied voltage are set as 80 Hz, sawtooth waveform and with a 150 Vpp, which were previously determined. Meanwhile, synthetic jets were positioned in cross flow, some additional parameters like wind speed, orifice size and synthetic jet location. Orifice size is the most important parameter and has ability to alter results considerably. In order to minimize the effect of these parameters for examination, they used flow visualization techniques Flow visualization study reveals the reduction of turbulent regions and also wake size changed. Observed effect of those changes was too small for the pressure sensors. They placed the model at an angle of six degree measured according to flow direction in order to amplify the effect of synthetic jets. This configuration enhance the effect of micro jets and results were in the limits and measureable and also boundary layer profiles was captured. Synthetic jets affected the upstream pressure distribution significantly and had minimal affect at downstream. Moreover, the jet effect was seen very strong at 36m/s compared to measurements they made on other speeds. Although a small reduction of the reverse regions are shown in the higher and lower speeds, those were not significant compare to 36m/s speed case.

Thereafter a different type of actuator designed and manufactured in 2005 by Yuanchang Liang et al [21]. It is made up of a special shape memory alloy named as FSMA, where F used for ferromagnetic and that is electromagnet actuators. Circular FSMA oscillates and produces the high momentum air flow. This particular technology is especially designed for the airplane wing's active flow control. These active flow control devices are able to enhance the aerodynamic performance and reduce jet noise. Synthetic jets brought significant improvement in active flow control. Currently, many synthetic

jets are constructed and used in airplane wings for active flow control and results are satisfactory for many applications. But it is thought that results may not be much effect at high Mach numbers [22], [23].

In 2007, Mahalingam focused on the thermal performance prediction using synthetic jet ejectors [12]. A two-dimensional synthetic jet was used to induce secondary flow in the channel. Thermal performance was predicted by a network resistance model. Modeling results was compared with the experimental data available for the synthetic jet integrated with a heat sink and also synthetic jets with in the channels. Two heated wall approximated as the channel and experiments was performed for different distances between the wall and for different aspect ratios. Constant heat flux was applied throughout the wall. The synthetic jet was placed alongside of the walls, where height and length were fixed to get results for different aspect ratio and width of channel.

Synthetic jets was modeled using Lumped Element method (LEM) in 2003 by Gallas et al [24]. Each component of system is considered as an element of electric circuit in Lumped Element Modeling using conjugate power variables. Similarly synthetic jet's different component was modeled. Q_{out}/V_{AC} is considered as frequency response of a synthetic jet while volume flow rate was considered as an applied voltage. Different geometry and material properties dependence was analyzed using LEM model circuit to have physical insight. Gallas also compared LEM with experiment. LEM model gave description that synthetic jet is coupled oscillator of 4th order. Piezoelectric diaphragm and Helmholtz resonator are first and second resonators respectively. An easy examination showed that three different cases related to a single oscillator. First case related to an incompressible fluid like water or when working fluid was a gas. The compliance of piezoelectric diaphragm is much larger than compare to cavity's acoustic

compliance. Second case resemble to a rigid piston or occurs when cavity's acoustic compliance is bigger that compared to the diaphragm's compliance. For the mentioned configuration synthetic jet acts like a Helmholtz resonator. In the last case, the compliance of the cavity is adjusted to give the same resonance as the diaphragm. A part from the LEM and experimental studies, design of cavity of a synthetic jet was examined by Uttukar et al. [25] numerically. Different configurations were studied related to cavity aspect ratio and the placement of piezoelectric diaphragm on the flow produced by a jet. Vortex dynamics, velocity profiles and other dynamical characteristics of the jet for various cases were examined and that allowed extracting some insight effect on the performance of jet.

Various applications of synthetic jets were examined by different researchers. Heat transfer and acoustic performances of a synthetic jet was modeled by Arik et al. [26]. An analytical model was developed that captured the coupled heat transfer, acoustic and structure dynamics physics, but that was also simple enough to investigate different parameters that affect the performance of synthetic jets for the physics behaviors mentioned above. A comparison of results is discussed in detail with experimental findings. Structural part of the disk and elastomeric wall was modeled using Ritz solution approach. The heat transfer coefficient calculation was utilized, a correlation intended for steady jets used with success there for pulsating jets when the exit velocity is modified to include the mean velocity of only the ejection portion of the pulsating jet cycle. Moreover, an attempt to predict sound with a model of acoustic impedance was made. They found discrepancy when compared the disk velocity and exit velocity. Navaratnam et al. [27] did a computational study using moving grid and observed turbulent boundary and synthetic jets interaction. Synthetic jet was modeled in a cross flow.

In 2008 Arik et al. [28] studied the local heat transfer coefficient for impingement cooling of a high frequency synthetic jet over a flat plate. Study was focused on meso scale high frequency synthetic jet's global and local heat transfer coefficients. Experiment have been performed with a square orifice of 1 mm, thickness of 2 mm and diameter of 12.5 mm. Operating frequency of synthetic jet was 4500 Hz that was also jet's resonance frequency. 30 and 50 volts were applied. Local temperature distribution was measured using IR (Infrared) camera named as thermal imaging, local radiative and convective heat transfer coefficients was calculated as a result of experimental findings. Ample amount of enhancement in heat transfer performance was observed that can make synthetic jet a potential candidate for cooling of electronic devices. On a different perspective of synthetic jets, an experimental investigation was carried out in 2009 by Mohammad et al [29] The actuator consists of a loudspeaker inside a cavity covered with an aluminum plate with a slot. In the experimental study, they investigated different slots and cavity volumes for which 5 different speakers were investigated. Results clarified that velocity magnitudes up to 40m/s is reached. Although there are a large number of sophisticated synthetic jets, in this study a simple loud speaker is investigated. It is also clearly emphasized that the aim of the research is to present a simple prototype model that can produce enough power and easy to manufacture for testing purposes. Measurements were performed by a hot-wire probe which was equipped with a tungsten wire. The manufactured actuator consists of a rectangular wood cavity, loudspeaker and an aluminum plate with a cut slot in the middle. The cavity is able to adjust by moving the loudspeaker. At the end, the velocity profiles for the most interesting slots are presented. It is clear that the wider slot looks more like a plug profile. Further it was shown that the cavity volume did not have any effect of the maximum velocity achieved. This is a kind

of feature desired on manufacturing. Thus, while the aim of this experiment was not to obtain any quantity or accurate measurements, idea of getting of magnitude of the maximum velocities and momentum by a simple actuator is presented.

Another important parameter for the performance of jet is Helmholtz resonance studied by Duncan [30]. They showed that how Helmholtz Resonance interacts with laminar boundary layer of active and nominally inactive micro-jets. They developed the method for the numerical simulation. Two different numerical simulations were run and first model showed interaction of boundary layer for active micro-jet actuator and results showed that the criterion was correct. They also found that boundary condition for actuator as predetermined wall was not appropriate, since interaction of boundary layer affect the net pressure around the exit of orifice and also had affect over the outflow. In the second simulation, 2D Tollmien–Schlichting waves, given driving frequency was different than Helmholtz resonance. It can be inferred from the results of simulation that for that particular set of configuration the actuators become a source of 3D Tollmien–Schlichting waves. Another computational study by David et al. [31] validated the behavior of piezoelectric through a tridimensional model showed satisfactory results. After validation an axisymmetric model of the complete (fluid and piezoelectric) synthetic jet actuator was implemented using COMSOL.

Gopi. and Mohseni [32] worked on experimental and theoretical study of axisymmetric and rectangular synthetic jets. In 2009 Gopi et al. [33] studied an experimental and theoretical examination of axisymmetric synthetic jet. Flow field of round orifice synthetic jet was observed in still air. They tried to find the similarity between the continuous turbulent jet and synthetic jets. They detected that synthetic jets flow can be modeled as turbulent jet by using the assumption of similarity analysis.

Synthetic jet was simulated using two methods. Schlichting method is used for the solution of cylindrical coordinate boundary layer equation and spherical coordinate Navier Stokes equation was solved using Landau-Squire method. Virtual viscosity coefficient of synthetic jet was used instead of continuous turbulent jet. Flow form orifice was measured using a hotwire anemometer. Centerline velocity separated the two different regions. First region in which periodic coherent vortex ring just started to interact named as developing region while in developed region turbulence (similar to continuous turbulent jet) was generated because of breakdown of vertical structure for round central orifice jet. The extent of the developing region is seen to scale with the stroke length while changing from one actuator to another. In the developed region, with the decaying of centerline velocity self-similar behavior of center-line velocity was exhibited and validated through experiments. The assumption of equivalence between turbulent jet and synthetic jet is considered on the basis of the same momentum flux. Periodic vertical structures introduces initially brought the mixing and also attributed was enhanced by eddy viscosity and resulting the transition to turbulence and breakdown of vortices. In another study, .Mohseni studied the synthetic jet energized by the piezoelectric actuators in quiescent air. They observed the flow field of synthetic jet in a rectangular channel [32]. Four different regions were observed separated through the centerline velocity. Periodical vertical structures interact and exist in the first region. Synthetic jet behavior found like a two-dimensional continuous planer jet in the second region. Third stage is transition stage where jet deviates from its two-dimensional behavior and sending effects because of narrow edges. In the last, it is decaying like a round jet and appears as an axisymmetric jet. They showed the systematic modeling of the synthetic jet as turbulent continuous jet, from decaying rate and spreading of vortices

they calculated eddy viscosity of synthetic jet. Proposed hypothesis was validated by observing the flow field; they also infer that continuous turbulent jet eddy viscosity is less than the equivalent synthetic jet.

In 2009 Mangesh.et al. [34], [35] analyzed the heat transfer and frequency response of synthetic impingement jet. Effect of frequency was investigated for the synthetic jet flow. Average of the velocity over an excitation cycle shows the upper bound and lower bound for the formation of a synthetic jet and it indicates that two frequencies of resonance. Hot wire anemometer had been used to measure the velocity of the synthetic jet. Synthetic jet had been made such a design that it was able to change the cavity depth, orifice diameter and operating frequencies of the diaphragm. Validations of results were done with the prior literature. Heat transfer measurements were made for the average heat transfer coefficient over the impinged surface. Effect of axial distance was observed over the heated surface. Distribution of static pressure, RMS and mean velocity were also quantified for the radial direction. They conducted the experiment for various factors for different ranges, Reynolds number, axial distance between the jet and heater, orifice diameter and orifice plate length. They found 11 times more heat transfer as compared to natural convection case at the best configuration of parameter mentioned above. The Nusselt number behavior of continuous jet was found to be closer to synthetic jet. Thickness of orifice and diameter of orifice plate has affected over average heat transfer coefficient. It is also shown that cavity depth has a minimum effect over average heat transfer coefficient. At the resonance of the cavity it is found that maximum heat transfer occurs. Coefficient of heat transfer initially increases and then decreases with respect to axial distance. Maximum heat transfer location depends on their specific parameters. They mentioned five non dimensional functions on which Nusselt number depends on.

Those functions are (Re, Pr, z/d, L/d, R/d). Experimental data for different cases was fit into the equation in order to correlate the Nusselt number. They mentioned a general correlation with Nusselt number values are decreasing with respect to those parameters.

Another computational study was performed in 2009 for jet based electronic cooling module in Deepak et, al [36]. Unsteady behavior of synthetic jet using a 2D transient numerical simulation, they used SST turbulence model and also observed the flow within the cavity and diaphragm movement. Selected ranges of parameters were modeled and examined computationally. Appropriate boundary conditions were applied to get full characteristics of fluid flow and heat transfer. The successive formation of vortex shedding of synthetic jet was captured correctly by a computer simulation. They found the amplitude of oscillated diaphragm and its frequency has high impact over the thermal performance of synthetic jet. Localized cooling was generated through periodicity of vortices at heated surface. They observed that a 30% more cooling is resulted from the synthetic jet as compared to a continuous jet, 20 to 120 times for different range of variables with respect to the natural convection. Their study showed clearly an extraordinary thermal performance of synthetic jet for the microelectronics applications. In another computational study has been presented by Amit. et al. [37] to examine the characteristics of synthetic jet for their orifice and cavity parameters. They examined the central orifice synthetic jet computationally by the assuming it as an axisymmetric jet. They performed the mesh sensitivity analysis before inferring the results, later they compared with prior available experimental results. They mimicked the moving boundary with a sinusoidal velocity inlet boundary condition. Their simulation showed that height of orifice and height of cavity has the least effect over the maximum velocity output, but showed some effect on the velocity with respect to time.

Persoons et al. [38] examined mechanism of heat transfer for small spacing between target surface and synthetic jet in 2009. Impinging synthetic jet flow structures and convective heat transfer characteristics were compared and relationship was found between them. Jet to surface spacing was 2 and the range of dimensionless stokes length was between 1 and 22, Re number was between 1000 to 4300. The experimental data for heat transfer showed power law curve fitting relationship for fixed stroke length between Nusselt and Reynolds numbers. Average heat transfer over time and phase locked flow field was shown for central orifice synthetic jet for small spacing between target surface and jet. Particle Image Velocimetry (PIV) method was used in order to characterize the flow field and effect of Reynolds number and L_0/D was closely measured. Two separate regions of flow were observed for constant jet to surface spacing. A thermal imaging camera was used for capturing heat transfer and localized Nusselt numbers. Later Persoons et al [39] presented the overall relationship for Nusselt number at the stagnation point for circular central orifice axisymmetric jet [40].

In order to operate and design the synthetic jet and reduced order general model was also studies by Persoons. [39]. Piezoelectric and electromagnetic actuations were model by considering their general lumped parameters. He found a close agreement with experimentally measured cavity pressures. Those can be obtained via calibration or estimation from pressure loss correlations and the governing acoustic radiation impedance. The model had been validated experimentally for circular and rectangular orifices. The effect of nozzle damping on the nonlinear system response is discussed. Analytical expressions are given for the two resonance frequencies characterizing the system response as a function of the diaphragm and Helmholtz resonance frequencies, also optimal design of an impinging synthetic jet actuator was discussed in term of

thermal acoustic efficiencies. Two key contributions of this paper are demonstrating how the nozzle flow dynamics affect the system response and in turn, the optimal operating frequency and amplitude, as well as the characterization of the nozzle dynamics with two empirical parameters K and β, which can be easily estimated or calibrated. This study has only considered synthetic jets issuing into a quiescent fluid. In cross flow conditions, the model is expected to hold, at least for moderate ratios of cross flow to jet velocity magnitude; however, this requires a further validation.

Another computational study is done for synthetic jets by Rusovici et al [41]. A coupled analysis is done using finite element technique. Ansys multiphysics module was used. They performed fully coupled analysis that is uniqueness of their work. They coupled the electrical domain with structural, structural domain with fluid flow. They gave excitation voltage to piezoelectric actuators. They also analyzed the acoustic-structural-piezoelectric model, but FSI for the piezoelectric actuators are more expensive that the acoustic one. They concluded the finite element modeling had a good agreement with experiments, with a relative error of 10 percent or less.

A study about predicting the heat transfer from unsteady synthetic jets is presented by Arik and Icoz [42]. It is mentioned that there are a number of research findings have shown the implementations of synthetic jets on heat transfer applications; however, there exists no correlations to analytically predict the heat transfer coefficient for such applications. A series of experiments they carried and a closed form correlation was developed for the prediction of coefficient of heat transfer including the variable geometrical parameter of jet, position, and operating conditions for impinging flow. The proposed relationship was shown to estimate the synthetic jet impingement heat transfer

within 25% accuracy for a wide range of operating conditions and geometrical variables. Following points are mentioned as a result of their experiments.

Transition in synthetic jet flows is studied in 2012 by Tesar etal [43]. They mentioned that this paper is the continuation of various studies that are already presented and it was analyzed experimentally for an axisymmetric jet using single equation turbulence model. They observed the spectrum of velocity and they tried to find the place where transition occurs for the flow regime of synthetic jet. They found an important point that transition in turbulence can be decreased as the operating point come closer to the resonance frequency. Tesar et al also examined the synthetic jet embedded in the impinging annular jet [44]. Annular impinging jet was controlled using synthetic jet. Experimental study had done on the control and generation of an impinging jet. Twelve synthetic jets were place in the radial direction for control in the body of a nozzle. They observed that this control enhance the mass and heat transfer and also flow field was changed by using these synthetic jets. Stagnation point heat transfer had the increase of 20% for medium spacing between the jet nozzle and wall.

In 2013, Yang et al [45] looked at the effect of vortex ring interaction with the wall of a synthetic jet. Two-dimensional particle image velocimetry (PIV) was used to investigate the interaction of vortices with a stationary wall. Both evolutions of vortical structures and statistical characteristics of flow fields at different orifice-to-wall distances were presented. They found that different orifice-to-wall distances have different effects in terms of the vortex strength and impinging speed when the vortex rings are approaching the wall. The secondary vortex ring can be observed within the shear layer only when the dimensionless orifice-to-wall distance is close to or less than the dimensionless stroke length. An appropriate orifice-to-wall distance plays a vital role in the sense of

impingement effect. The statistical analysis of the flow field indicated that a wall jet forms after impingement, while both the decay rate of the maximum radial velocity and the spreading rate of the half-width decreased with the increasing orifice-to-wall distance. The non-dimensional wall jet velocity profiles for different orifice-to-wall distances all exhibited self-similar behaviors, which is well consistent with the theoretical solution of the laminar wall jet.

A Small piezoelectric pump was investigated for heat transfer with a small flow rate (1 L/min) and pressure difference of 2kPa by Andrew et al [46] in 2012. They tried to build the experimental setup like the setup is being used for the impinging jet. They placed the jet normal to the heated surface. A constant flux heater made through thin sheet or copper was used and also in order to capture the temperature distribution over a heat IR camera was used. Distance between heater surface and jet and amplitude of vibrating diaphragm was correlated with heat transfer in order to have insight knowledge of these parameters over the performance of a synthetic jet. Peak heat transfer took place at the center of the heater. In each case, maximum heat transfer found at the stagnation point irrespective of amplitude and frequency of piezoelectric diaphragm. In order to predict the Nusselt number a relationship is developed using experimental data. In order to have high heat transfer an optimum distance between heater and nozzle should find. This distance calculation found the function of area of heater and nozzle.

Another study on steady and unsteady air impinging heat transfer for electronics cooling application Arik et al [47] in 2013 is presented. They investigated the steady jet flow and pulsating flow by synthetic jets that can be used in applications requiring significant amounts of heat removal from electronics components. To mimic a typical electronics component, a vertical 1x1 inch heated area was used for heat removal. The

impingement heat transfer, in the form of Nusselt number, is reported for periodic and steady Reynolds numbers from 100 to 3000. The effect of distance between target plate and jet on the impingement heat transfer is also investigated. Important results inferred from this study are as follows,

- As the Reynolds number increases heat transfer increases for both periodic and steady jet.
- Nusselt number was more affected by the distance between heater and nozzle.
- For Reynolds number less than 400, constant steady and synthetic jet showed comparable heat transfer. At low Re number, air flow from synthetic jets is only weakly turbulent. Under these conditions, the heat transfer response of both jet types is similar.
- At peak jet-to-heater spacing 30% more cooling is observed by synthetic jet compare to steady jet.

Youmin et al [48] studied the synthetic jet actuator synthetic jet actuator compare the heat sink cool by natural convection also synthetic jet embedded into heat sink. Two synthetic jet arrays with one agitator were investigated into to one channel heat sink experimentally and computationally. Their results can be extended to a full heat sink having number of channels and fins. They compared their results with heat sink having flow in the channel only with flow with synthetic jet and agitator. They found a rise of 82.4% in the heat transfer after using of jet and agitator.

Another study on modeling and experimental validation of the frequency response of synthetic jets is done by Luca et al [49]. Lumped element mathematical model of the operation of a synthetic jet actuator driven by a thin piezoelectric disk is both analytically and numerically investigated in order to obtain information about the frequency response

of the device. The model is validated through experimental tests carried out on three devices having different mechanical and geometrical characteristics. They designed primarily in order to achieve an increasing coupling strength. A computational study from Ghaffari et al [50] is carried out in 2014. A meso-scale synthetic jet actuated with a sine-wave is studied computationally with a commercially available CFD software package. Momentum, temperature fields, surface and near- wall profiles are computed. By looking at the numerical results, the following deductions can be inferred for the study. Non-monotonic behavior of turbulence kinetic energy and pressure along with strong pressure gradients leads to non-monotonic profiles for the skin friction and surface heat transfer coefficient. However, the time averaged profiles show almost a monotonic behavior independent of the jet frequency. Another study form Ghaffari etal showed the tempeature and momentum field for little surface to jet space for the synthetic jet [51]. Ikhlaq et al [52] studied effect of actuator deflection on heat transfer for low and high frequency synthetic jets. Two different low frequency synthetic jets manufactured in our laboratory and a commercially available high frequency jet are included in that study. Heat transfer performance is given as an enhancement over natural convection heat transfer. The heat transfer enhancement factor of each of these jets with respect to natural convection is measured over a 25.4x25.4 (mm) vertical heater.

1.4. Objectives:

The literature survey presented above has permitted the identification of key technical issues that remain to be resolved in order to fully implement synthetic jets into realistic applications. In order to understand the effect of distance between the orifice and heated surface, different size of synthetic jets and effect of different operating frequency with respect to the deflection of the diaphragm is not discuss and analyzed before. No

correlation is available to predict the heat transfer characteristics of low and high frequency central orifice jet. For above mentioned properties are measured experimentally and detail of experiment will be discussed in detail in later chapters.

Different mode shapes of the piezoelectric diaphragm actuators are no being analyzed before. Effect of the vortex ring over a target plate for the semi-confined jet space is being analyzed. Vortex interaction is closely analyzed with the target surface. For this computational tools Comsol and Ansys is used detail boundary conditions will be discussed in later chapters.

CHAPTER II

2. SYNTHETIC JET MODELING

The electrostictive induced diaphragm motion is the forcing mechanism in piezoelectric actuators. Extensive work has been done on modeling of circular plates of piezoelectric and almost every work is on bimorph actuators that contain layers that are symmetrical about the mid plane and thus have no bending-extension coupling. Suryanarayana et al [53] have used plate theory is used to derive circular laminated piezo plates composed with one or more transversely isotropic piezoelectric layers via lumped-element modeling. The model for a piezoelectric unimorph actuator developed it provided a close agreement for the first resonance frequency.

2.1. Piezoelectric Material

Relationship between and the electricity and pressure is known as piezoelectricity and found in many materials in nature. Piezoelectric actuators are being widely used in aerospace industry. Piezoelectric materials can be used in two different ways one is by giving excitation voltage deformation can get and this behavior can be used in the deletion of the vibration and secondly while inducing the deformation into material and DC output voltage can get and can be used as sensor. Because these types of materials are able to respond and sense the changes in their environment that is why they named as "intelligent" and "smart" materials. Piezoelectric material can be used in two different manners are following;

- Direct piezoelectric effect (Deformation of the piezoelectric material causes an electrical charge on certain opposite faces of the piezoelectric material).

- Converse piezoelectric effect (Application of an electric field across certain opposite faces of the piezoelectric material causes the material to be deformed).

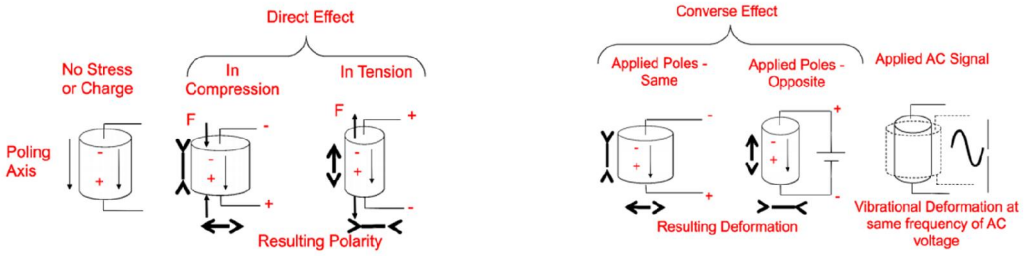

(a) (b)

Figure 2: (a) Direct piezoelectric effect (b) Converse piezoelectric effect [54]

In a piezoelectric disk an excitation voltage causes to arrange the poles which are persuading stresses in the material equivalent to –eF so called inverse piezoelectric effect. The coupled equation that model the inverse piezoelectric effect on the disk are [31]. S is strain, s is compliance and T is stress in equation (1) and (2). These may be combined into so-called coupled equations, of which the strain-charge form is:

$$\{S\} = [s^M]\{\sigma\} + [G^K]\{M\} \quad (1)$$

$$\{C\} = [G]\{\sigma\} + [\epsilon^\sigma]\{M\} \quad (2)$$

For the direct piezoelectric effect is shown as *[G]* matrix, converse piezoelectric effect is shown as $[G^K]$. *M* and *B* means constant and can be zero electric field and stress field respectively. Superscript K indicates as transpose.

$$\begin{bmatrix} s_1 \\ s_2 \\ s_3 \\ s_4 \\ s_5 \\ s_6 \end{bmatrix} = \begin{bmatrix} S_{11}^E & S_{12}^E & S_{13}^E & 0 & 0 & 0 \\ S_{21}^E & S_{22}^E & S_{23}^E & 0 & 0 & 0 \\ S_{31}^E & S_{32}^E & S_{33}^E & 0 & 0 & 0 \\ 0 & 0 & 0 & S_{44}^E & 0 & 0 \\ 0 & 0 & 0 & 0 & S_{55}^E & 0 \\ 0 & 0 & 0 & 0 & 0 & S_{66}^E = 2(S_{11}^E - S_{12}^E) \end{bmatrix} \begin{bmatrix} \sigma_1 \\ \sigma_2 \\ \sigma_3 \\ \sigma_4 \\ \sigma_5 \\ \sigma_6 \end{bmatrix} + \begin{bmatrix} 0 & 0 & G_{31} \\ 0 & 0 & G_{32} \\ 0 & 0 & G_{33} \\ 0 & G_{24} & 0 \\ G_{15} & 0 & 0 \\ 0 & 0 & 0 \end{bmatrix} \begin{bmatrix} M_1 \\ M_2 \\ M_3 \end{bmatrix} \quad (3)$$

$$\begin{bmatrix} C_1 \\ C_2 \\ C_3 \end{bmatrix} = \begin{bmatrix} 0 & 0 & 0 & 0 & G_{15} & 0 \\ 0 & 0 & 0 & G_{24} & 0 & 0 \\ G_{31} & G_{32} & G_{33} & 0 & 0 & 0 \end{bmatrix} \begin{bmatrix} \sigma_1 \\ \sigma_2 \\ \sigma_3 \\ \sigma_4 \\ \sigma_5 \\ \sigma_6 \end{bmatrix} + \begin{bmatrix} \epsilon_{11} & 0 & 0 \\ 0 & \epsilon_{22} & 0 \\ 0 & 0 & \epsilon_{33} \end{bmatrix} \begin{bmatrix} M_1 \\ M_2 \\ M_3 \end{bmatrix} \quad (4)$$

2.2. Diaphragm

In synthetic jets vibrating plate is considered as a diaphragm clamped from its periphery. According to the Kirchhoff-law governing linear differential equation of plates is

$$\nabla^4 \delta = \frac{F}{d} \quad (5)$$

Where N is the flexure rigidity of the plate, defined as,

$$N = \frac{El^3}{12(1-\nu^2)} \quad (6)$$

The flexural rigidity is a constant that is a result of the derivation of plate equilibrium. E and ν are material properties of plate. In synthetic jets diaphragms has distributed load especially in the case of piezoelectric actuators. Usually piezoelectric material is attached over a metallic diaphragm and when voltage is applied, distributed load over diaphragm is created. Typically piezoelectric driven Synthetic jets loading don't create any twisting effect in the plate and load is considered to be asymmetrical, all of the angular terms are equal to zero. Thus equation (5) can be written as,

$$\frac{1}{r} * \frac{d}{dr}\left(r * \frac{d}{dr}\left(\frac{1}{r} * \frac{d}{dr}\left(r * \frac{d\delta}{dr} \right) \right) \right) = \frac{F}{N} \quad (7)$$

This is a separable equation and can be solved for δ(r), since diaphragm is clamped from the periphery δ(0) is finite, two of constant coefficient is equal to zero because zero deflection at the end. Other two boundary conditions are needed to find other two

constants. From the plate theory and we considered as no twisting and coefficient can be found by putting boundary condition in equation of moment [55]. Final form of equation is shown in equation (8),

$$\delta(r) = \frac{Fr^4}{64N}\left(\frac{r^4}{a^4} - 2 * \frac{3+\nu}{1+\nu} * \frac{r^2}{a^2} + \frac{5+\nu}{1+\nu}\right) \quad (8)$$

Another important parameter having huge effect on synthetic jet performance is resonance frequency of the actuator. Structural resonance frequency depends on the geometric parameter (diameter, thickness) and material properties (young's modulus, Poisson ratio). In order to calculate first hand on structural resonance frequency for an isotropic material using basic material properties mention by [56].

$$\mathrm{f_d} = 0.4705 * \frac{l}{\mathrm{r}^2}\sqrt{\frac{\mathrm{E}}{\rho(1-\nu^2)}} \quad (9)$$

Where E is modulus of elasticity, ρ is density; υ is Poisson ratio of material and r is the radius of diaphragm. Equation (9) is for a single clamped diaphragm and it is short in capturing the effect of piezoelectric layer on the top metallic plate. In order to calculate other resonance frequency except the principle mode advance mathematical model is needed or commercially available software can be used for modal analysis.

2.3. Cavity

Another important frequency can have effect on the performance of Synthetic jets named and cavity resonance or Helmholtz resonance. Pressure of the cavity can be increased by pushing air in. When inside pressure of the cavity is increased and then releases it. After that air is oscillating in and out, because of this phenomenon at which that air oscillates is known as Helmholtz resonance. The following expression is for the Helmholtz resonance frequency of a typical cavity given in [56].

$$f_h = \frac{c}{2\pi}\sqrt{\frac{A}{(H+0.85d)V_c}} \tag{10}$$

Where c speed of sound, H is cavity height, d is orifice diameter and V cavity volume, A is area of orifice, Helmholtz resonance frequency is playing an important role if the driving and Helmholtz frequencies are near to each other [32].

2.4. Definition of Reynolds Number Synthetic Jet

The mass ejected from the nozzle of a synthetic jet in a single period is written as follows:

$$\int_{m1}^{m2} dm = \int_{0}^{\zeta/2} \rho A u(t)\, dt \tag{11}$$

The mass ejected from the nozzle of a synthetic jet in a single period is written as follows:

$$m = 2\pi\rho d_j L^2 \tag{12}$$

Where dj is deflection of diaphragm and L is radius of cavity. From Equation (13), the average velocity exiting the nozzle during the ejection phase is determined as:

$$\bar{u}_j = 16\frac{d_j}{\zeta}\left(\frac{L}{d}\right)^2 \tag{13}$$

A is the nozzle area. If the synthetic jet operates on a sine wave, and the velocity is assumed to be spatially invariant at the nozzle-exit. Therefore, Re for a synthetic jet can be written as:

$$Re_{D_j} = \rho\frac{16L^2\frac{d_j}{d}}{\zeta\mu} \tag{14}$$

$$Re = \frac{\rho V d}{\mu} \tag{15}$$

$$Re = \frac{\rho V d}{\pi \mu} \tag{16}$$

Equation (14), (15) and (16) show the different definitions for the Reynolds number. Equation (14) shows the Reynolds number can be calculated using deflection of the diaphragm that can be measure using Laser vibrometer. The diaphragm profile can be assumed mentioned in either equation (20) and (21). Equation (15) shows the Reynolds number calculation from the maximum velocity measured from the hotwire anemometer mentioned [42]. Equation (16) shows the Reynolds number calculation by averaging over a cycle. In this study definition of Reynolds number is used that is mention in equation (14) and (16). Equation (14) is used for computational study while equation (16) is used to calculate Reynolds number for proposed correlations of heat transfer will be discussed further in the chapter of results and discussion.

2.5. Dimensionless parameters for synthetic jets:

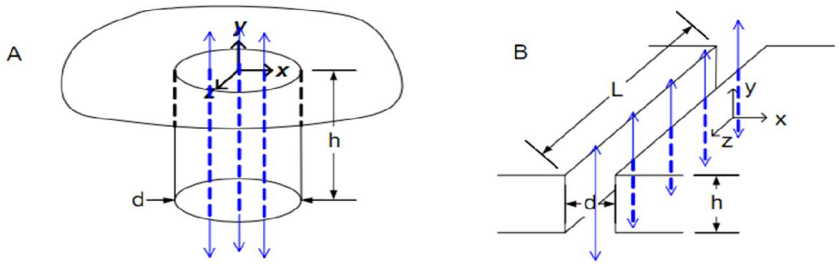

Figure 3: Orifice detail with coordinate system [57]

The jet orifice velocity scale of interest is the time-averaged exit velocity $\bar{u}_j$ that is given by

$$\overline{u_j} = \frac{2}{t}\,\frac{1}{A}\int_A \int_0^{t/2} u(\zeta, x)\,dt\,dA \tag{17}$$

Figure 3 explains geometric parameters definitions and fluid properties. A set of dimensional variables upon which the jet velocity profile is dependent is listed below:

$$\overline{u_j} = fn(\omega, \mathbb{v}, d, h, L, \omega d, \Delta\mathbb{v}, \rho, \mu, c) \tag{18}$$

The Buckingham-Pi theorem [58] is then used to construct the Π-groups in terms of the independent dimensional units M, L and T, respectively for Mass, Length and Time. Table D-2 lists the dimensions of all variables. The number of parameters is 11, n =11 and the rank of the matrix is 3. Thus 11-3=8 Π-groups are expected. The 3 primary variables chosen are the length scale d, the time scale ω, and the density ρ (for mass scale) [57].

The most important dimensionless parameters in synthetic jet technology are given as follows.

$$\text{Strouhal Number}=St=\frac{fd}{\overline{u_j}}$$

$$\text{Ratio of the driving frequency to the Helmholtz frequency} =\frac{f}{f_H}$$

$$\text{Ratio of the operating frequency of the Driver}=\frac{f}{f_d}$$

$$\textit{Stokes No}=Stk=\sqrt{\frac{fd^2}{\upsilon}}$$

The formation of synthetic jet is manipulated and governed by many parameters including the non-dimensional number. The most important parameters are Reynolds number (Re), Strouhal number (Sr) and Stokes number (St). Criteria of jet formation are also depending on these dimensionless numbers. In literature there are two different criteria is given one for two dimensional jets and one for axisymmetric jet. $1/Stk=Re/St^2>1$ for 2D jet and $1/Stk=Re/St^2>0.16$ for axisymmetric jet.

CHAPTER III

3. NUMERICAL MODELING

Three different computational studies are completed in the current synthetic jet study. Two of them related to structural part of piezoelectric actuators while one on the fluidic (CFD) side of synthetic jet. Following computational studies have been performed,

- Diaphragm modeling
    - Modal analysis using COMSOL 4.0
    - Transient deflection using piezoelectric module of COMSOL 4.0
- CFD modeling of synthetic jet

Four indigenously designed and manufactured synthetic jets were analyzed and one commercially available high frequency synthetic jet was examined. High frequency synthetic jet was disassembled and dimensions were measured using a Vernier Caliper. Two different types of synthetic jets were analyzed regarding to its orifice shape,

- Slotted orifice jet
- Central orifice jet

Table 1 gives material and geometric properties of central orifice jet, while Table 2 shows material and geometric properties for the slot orifice jets. ART4000 is corresponds 40 mm synthetic jet, ART2000 corresponds to 20 mm synthetic jet and similarly for ART4500 and ART3500.

Table 1: Central orifice synthetic jet geometric parameters

	Properties	ART4000	ART2000	Commercial jet
Geometry	Shim diameter (mm)	40	20	13
	Shim thickness (mm)	0.1	0.2	0.08
	Piezoelectric diameter (mm)	25	15	10
	Piezoelectric Thickness (mm)	0.1	0.1	0.1
	Cavity diameter (mm)	38	18	12
	Cavity height (mm)	1.2	1	0.1
	Orifice diameter (mm)	2	1	1
Shim	Young's modulus (Pa)	2.00E+11	1.10e11	2.00e11
	Poisson's ratio	0.3	0.34	0.3
	Density (kg/m^3)	7750	8490	7750

Table 2: Slotted orifice synthetic jet geometric parameters

		ART 4500	ART 3500
Geometry	Shim diameter (mm)	45	35
	Shim thickness (mm)	0.1	0.24
	Piezoelectric diameter (mm)	25	25
	Piezoelectric thickness (mm)	0.1	0.24
	Cavity diameter (mm)	43	33
	Cavity height (mm)	2.1	1.1
	Orifice hydraulic diameter (mm)	3	2
	Orifice length (mm)		
Shim	Young's modulus (Pa)	9.7e10	9.7e10
	Poisson's ratio	0.36	0.36
	Density (kg/m^3)	8490	8490

3.1. Diaphragm Modeling

Presently computational tools are getting significance in all engineering field. COMSOL 4.0 is used for diaphragm modeling. Both modal and transient analyses have

been done for the diaphragm. Detailed boundary conditions and will be discussed in upcoming sections.

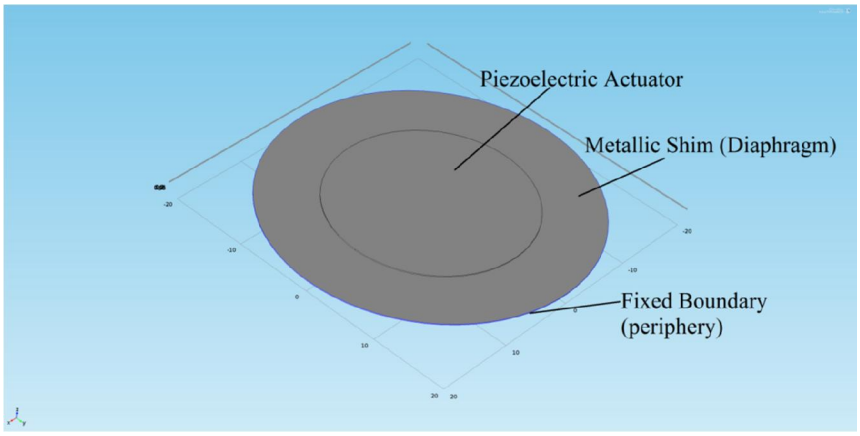

Figure 4: Piezoelectric actuator with diaphragm for computational modeling of diaphragm

A diaphragm with a piezoelectric actuator is modeled. Simplified geometry for the diaphragm modeling is shown in the Figure 4. The bigger disk is the metallic shim and it acts like a diaphragm, while the small disk on the top of the bigger one is piezoelectric actuator. For the current study, four different sizes of actuators were analyzed in which material of metallic diaphragm was either brass or steel, while material for piezoelectric actuator was fixed as PZT-5A. It is also assumed that interface between diaphragm and actuator is perfectly matched and no relative motion was assumed during all simulations.

In numerical study, mesh size plays an important role. Mesh sensitivity analysis was done before getting any results from the computational study. Different mesh sizes were used to solve problem, any variable's value can be check for all configurations of meshes and mesh iteration should be continued until nearly same value will come out for the two different mesh sizes.

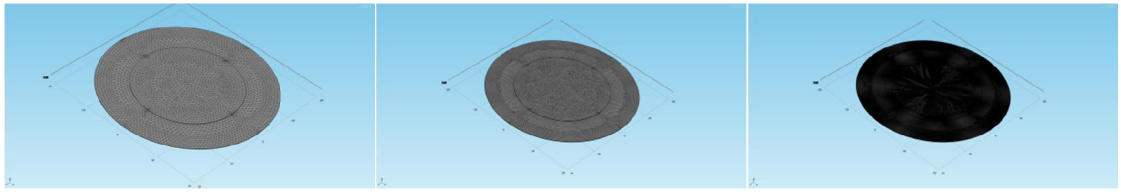

(a) (b) (c)

Figure 5: Different number of elements (a) Coarse mesh (b) Fine mesh (c) Finer mesh

Figure 5 shows three different sizes of elements. It is shown that these three different meshes have different number of element. For ART4500 and ART3500 deflections were measured for these two actuators. Figure 6 shows deflection for different number of elements. It is clear from the values that for the last two mesh sizes for both actuators show almost the same value of deflection. Less number of elements gives unreliable results, while dense of mesh structure can be expensive computationally. In current study, very fine mesh is used for other actuators except ART4500 and ART3500, because of availability of high computing power. It is recommended that when results become grid independent, the least number of elements should use if the computational power is limited.

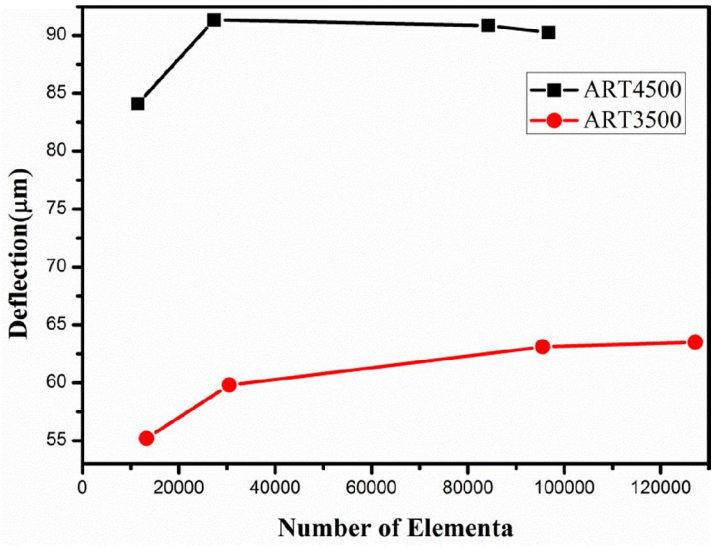

Figure 6: Mesh sensitivity analysis

3.2. Modal Analysis of an Actuator

Modal analysis is a special type of study that measures the response or dynamic response of the system when it is exposed to an excitation, since except first mode shape an appropriate value of excitation is required that can bring the system to response at high mode shapes. In an experimental study, sometimes high excitation power is required and very expensive experimental facility including a scanning laser vibrometer to capture higher mode shapes may be necessary. In order to calculate the first resonance frequency while for approximating the resonance frequency analytically roots of first kind Bessel function is required.

Calculating resonance frequency for different mode shape using commercially available software such as Comsol can be very practical. In order to calculate the frequency response of the piezoelectric diaphragm following are the boundary conditions and assumptions are being made.

- Geometric properties mentioned in Table 1 and Table 2.
- Material properties mention in Table 1 and Table 2.
- Outer periphery of metallic diaphragm is fixed.
- Piezoelectric disk is perfectly fixed over a metallic diaphragm; relative motion between them is zero.
- Air damping is neglected and operated actuator in vacuum.

In Figure 4, blue line over the periphery shows the fixed boundary for the actuator. By mentioning the number of mode shape required computational software is capable of solving for those mode shapes.

3.3. Transient Deflection Modeling of a Diaphragm

Piezoelectric diaphragm behavior is transient in nature. A steady state assumption cannot be used for these actuators. While simulating piezoelectric actuators one thing should be kept in consideration that it is a multiphysics problem and two different physics should be coupled to simulate the complete problem. Electrical and structural modules in Comsol are coupled to simulate the piezoelectric actuators. Following assumptions are used for the transient deflection modeling of the diaphragm.

- Piezoelectric disk is perfectly fixed over a metallic diaphragm; relative motion between them is zero.
- Air damping is neglected and operated actuator in vacuum.

Figure 7 illustrates the basic boundary conditions for the transient analysis of the piezoelectric diaphragm. In Figure 7, the bigger rectangle is representing the metallic circular diaphragm while small rectangle is representing the piezoelectric actuators. The periphery of the metallic diaphragm is fixed. Electrical boundary condition for the piezoelectric actuator should be applied. Upper face of the piezo actuator is assigned as ground boundary condition and other face of piezo diaphragm is assigned as electrical potential boundary condition.

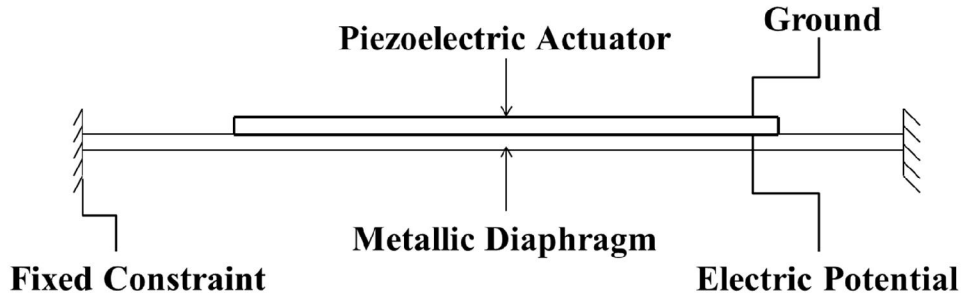

Figure 7: Boundary conditions for transient deflection measurement for piezoelectric actuators

Equation (19) shows details about applied voltage to the piezoelectric actuator in COMSOL [59]. It is shown in equation (19) that there are two more parameters that are important in transient simulation of diaphragm (i.e. frequency and time step). Results of deflection are highly depending on these two factors. Frequency is the driving resonance frequency of the diaphragm found from the modal analysis of the diaphragm.

$$V = V_o Sin(2 * \pi * f * t) = V_o Sin\left(2 * \pi * \frac{t}{\zeta}\right) \tag{19}$$

Time step is playing an important role in the reliability of the computational results. Enough number of points should be needed to resolve one cycle to get as similar as possible for the real system. ζ is the corresponding time period to frequency. For the current study three hundred and sixty points were considered in one cycle. In equation (19), t is calculated by dividing the ζ with 360.

3.4. CFD modeling of synthetic jet

Comsol multiphysics is based on the finite element formulation which is considered to be reliable solver for the solid and electrical module, but when it comes to the fluid solver finite volume is consider to be most reliable than finite element. Moving mesh technique is used for CDF and ANSYS CFX has vast history as compared to Comsol,. Therefore Ansys CFX is utilized for the computationally flow visualization of synthetic jet.

A 3-D computational fluid dynamics model was constructed to determine the flow and temperature fields of a meso-scale synthetic jet at a nozzle-to-target surface spacing of Y/D = 2 and Re_{Dj}= 1400 for the round orifice synthetic jet. Figure 8 shows the computational domain for CFX model. The whole computational domain is made up of

many cylinders. Geometry is divided into many small-scale cylinders to have the mesh customized for current simulation.

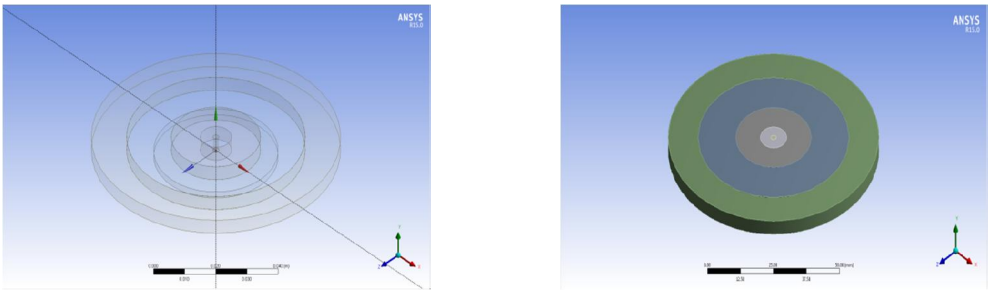

(a) (b)

Figure 8: 3D geometry for the computational domain

Figure 9 shows the mesh used for the current CFD study. It is seen that at center mesh is very fine as compared to the outer domain, a very fine mesh is used near to the orifice, and a coarse mesh in other regions relatively. Majority of elements are brick in the current study.

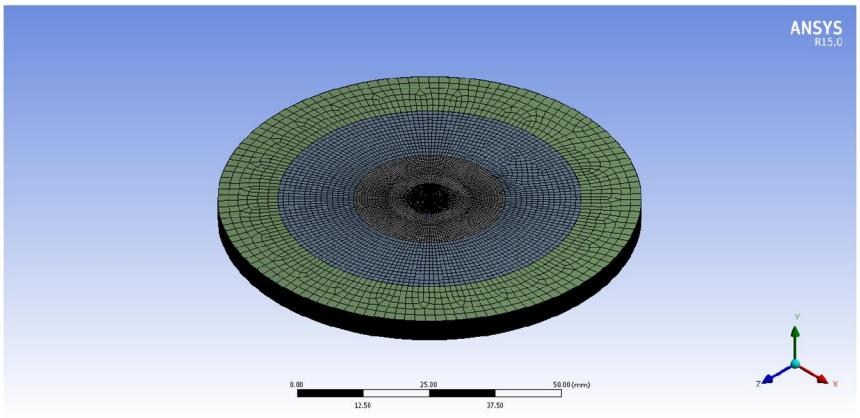

Figure 9: Mesh structure

Unlike the majority of similar computational studies, rather than specifying the velocity boundary conditions at the nozzle, the flow inside the synthetic jet device was solved by specifying the time dependent boundary conditions on the vibrating diaphragm

and utilizing the moving mesh technique. Local surface pressure and heat transfer coefficient distributions were determined and discussed. It was found that the pulsating flow at the nozzle exit for a round jet generates vortex rings and these rings seem to have some considerable effects on the target surface profiles.

$$\frac{d}{d_j} = 1 - \frac{r^2}{R^2} \tag{20}$$

$$\frac{d}{d_j} = 1 - \frac{r^2}{R^2} + 2.\frac{r^2}{R^2}\ln\left(\frac{r}{R}\right) \tag{21}$$

As it is mentioned, moving mesh techniques is used to get air velocity from the orifice of synthetic jet. In transient analysis of a piezoelectric actuator, the outer periphery if actuator was fixed, maximum deflection was observed at the center of the orifice. In order to mimic the diaphragm deflection two different types of profiles are being used in the literature [33].

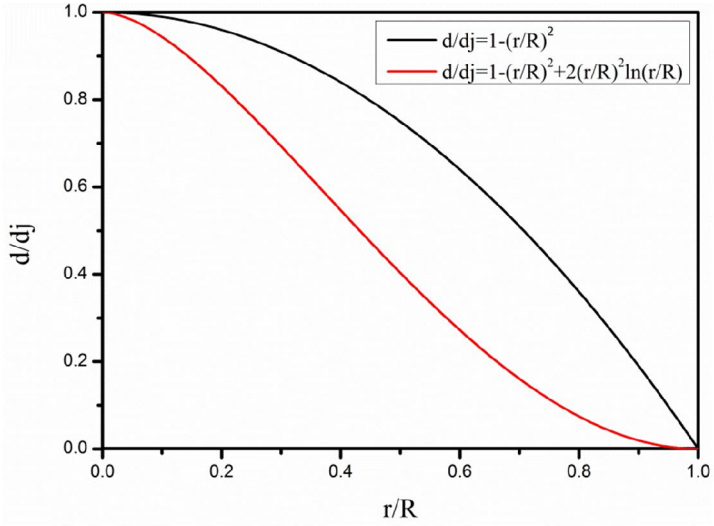

Figure 10: Profile for the deflection of diaphragm

Figure 10 illustrates the difference between these two profiles. It is observed the profile given in equation (21) is closer to the real diaphragm deflection as compare to the profile mention in equation (20). It is possible to insert boundary condition in the form of the profile given above. A comparatively easy way is by integrating the equation (21) for the variable r from 0 to R, following result is found.

$$D = 0.25 * D_j \tag{22}$$

The result of integration of equation (21) gives us the result mentioned in equation (22). The result tells us that displaced volume by using profile mentioned in equation (21) will be equal to the volume displaced when the whole diaphragm will move (supposing the periphery is not fixed) with the one fourth of the maximum deflection.

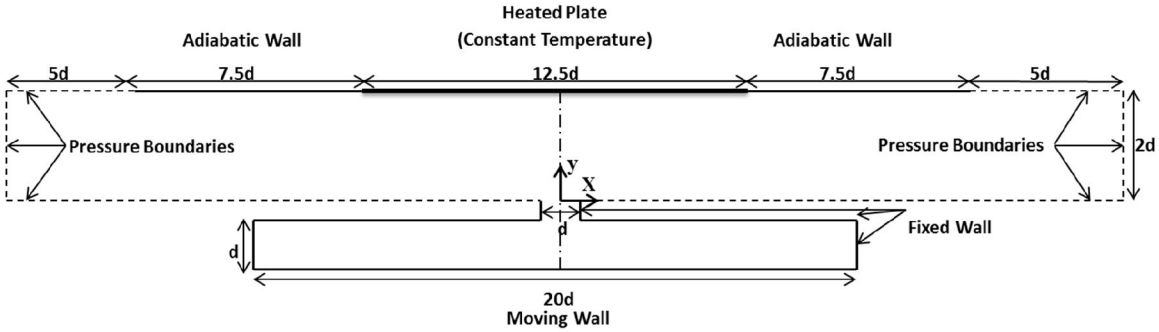

(a)

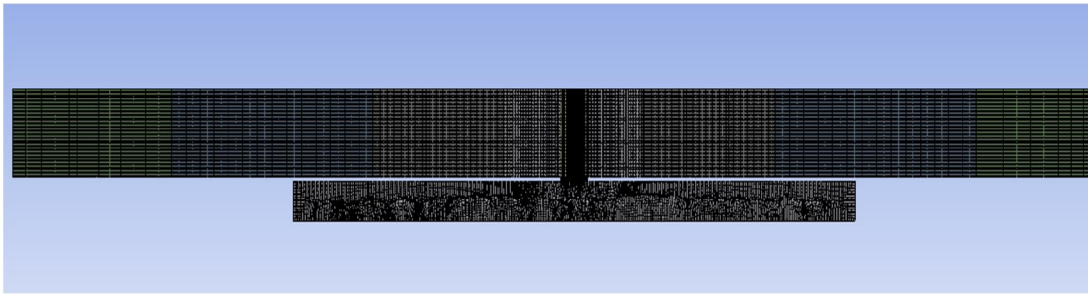

(b)

Figure 11: Computational (a) domain and boundary conditions, (b) grid structure

For the current CFD study, the basic boundary condition given to system was deflection of the diaphragm. The one fourth of the maximum deflection was applied that was measured from experiments on the piezoelectric actuator. Deflection boundary condition is mentioned in the equation (23).

In this study, the flow and temperature fields created by a synthetic jet emanated from a circular nozzle are numerically investigated. Computational domain, boundary conditions and grid are depicted in Figure 11. The computational domain consists of two circular rings connected via a circular nozzle. The size of the computational domain is 18.75 nozzle diameters ($0 \leq r/d \leq 18.75$) in the radial direction, and 4 nozzle diameters (maximum, $-2.0 \leq y/d \leq 2.0$) in the wall-normal direction with $y = 0$ corresponding to the nozzle exit. The target plate is placed at two nozzle diameters away from the nozzle exit with:

Wall: Target plate – Heated section: $0 \leq r/d \leq 6.25$

Wall: Target plate – Unheated section: $6.25 \leq r/d \leq 13.75$

The computational domain is further extended with five nozzle diameters in the radial direction with zero-pressure boundary conditions at $13.75 \leq r/d \leq 18.75$. The size of the computational domain in the radial direction is chosen such that there is no circulation at the vertical boundaries on each side to establish them as zero-pressure boundaries. The synthetic jet is a semi-confined jet with a confinement wall extending up to$0.5 \leq r/d \leq L/d = 10$ at $y = 0$.

The diaphragm is taken as a rigid circular disk (with a diameter of 2L) moving wall boundary, which reciprocates around y/d = -2.0 as follows:

$$D(t)=D.\ cos(2.\pi.f.t) =0.25.D_j\ cos\left(2.\pi.\frac{t}{\zeta}\right) \tag{23}$$

Where dj shows the maximum deflection of the diaphragm. Transport fields only at the first fundamental frequency of the synthetic jet of 500 Hz are considered in this study. Therefore, at this frequency, the corresponding period is ζ = 2 ms, and the time stepping is chosen at a fixed interval of 5.55 μs in order to have 360 time steps per cycle. Initial conditions of the computational domain are as follows:

$$u\ (r, y,\ t = 0) = 0$$

$$T\ (r, y,\ t = 0) = T_{amb}$$

$$\text{Wall: } T\ (0 \leq r/d \leq 12.5, y = 2d, t = 0) - T_{amb} = 35\ ^{\circ}\text{C}$$

Only conduction and convection heat transfer components are taken into consideration and radiation heat transfer between the heated wall and its surroundings is neglected in the computations. All the computations are performed with a commercially available general purpose CFD package [60].

CHAPTER IV

4. EXPERIMENTAL STUDY

4.1. Experimental Setup

Various properties of synthetic jets were calculated and mentioned by different researchers from heat transfer measurements to power consumption measurements. A number of techniques have been applied by researchers to measure heat transfer distribution on synthetic jet impingement surfaces. There are two most commonly used techniques for heat transfer using constant heat flux surface and constant temperature surface. A uniform heat-generating surface can be achieved through the use of a highly conductive plate. This plate can be soldered to copper bars using the tin and lead based solder and a hot plate. As the stainless steel copper interface removes from both ends of the sheet, a surface area will be left exposed to air on both sides. The copper bars will serve as voltage terminals and due to uniform heating within the stainless steel sheet; a constant heat flux can be generated. Uniform heat flux techniques is used by many researcher to measure local heat transfer for synthetic impinging jet [38], [46]. Measurements on constant heat flux (iso-flux) surfaces can be measured, if the applied heat flux on the surface is known, local heat transfer coefficient can be predicted by measuring the surface temperature for the location of interest. Heat transfer surface distribution of iso-flux surfaces can be obtained using IR thermography as mentioned by Kimber et al [46].

Constant temperature can be achieved using a kapton heater available in market for small surfaces, for bigger surface number of independent heaters on the surface; the power applied on individual heaters can be adjusted so that a constant temperature surface is obtained. Then, heat transfer coefficient can be determined by using measured heat flux

values and surface temperatures. The main goal is to obtain local heat transfer coefficients, however, with this technique, only average heat transfer coefficients can be predicted for those individually heated areas.

Four different type of experiment carried out on the synthetic jets in the present study. Following are four different types of measurements made on Synthetic jets synthetic jets.

- Deflection measurements
- Velocity measurements
- Power consumption measurements
- Heat transfer measurements

List of equipment's used for the above mentioned measurements are as follows,

- Single point laser vibrometer
- Hotwire anemometer
- 3D robot
- Agilent function generator
- Agilent data acquisition
- Trek amplifier
- Agilent DC power supply
- Agilent oscilloscope
- Indigenously made calibrated heater.
- T-type thermocouples (5-thermocouples)
- LabView2013

Experimental setup for each type of measurement will be discussed in following sections.

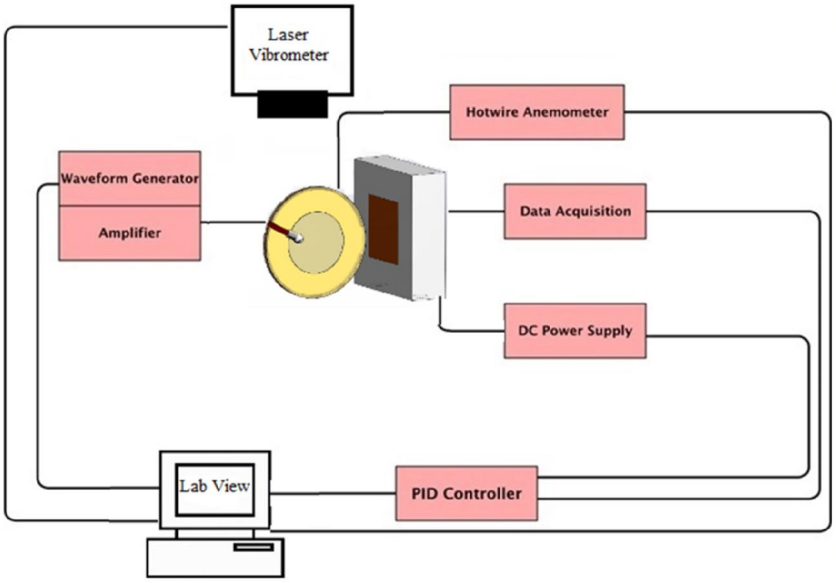

Figure 12: Schematic diagram of experimental setup

Figure 12 displays the schematic diagram for the experimental setup for the synthetic jets except the power measurement equipment. It is shown that using a computer is controlling all of the equipment.

4.2. Deflection measurements

Different measurements can be made on the vibrating diaphragm. One of the basic measurements is deflection measurements. Different techniques had been used by researchers depending on the required sensitivity. Laser technique is the most accurate and precise to measure deflection. Mode shape of vibrating diaphragm can also be measured using a scanning laser vibrometer [61]. Single-point laser vibrometer is being used to measure maximum deflection of piezoelectric actuators at the central position. A Polytec OFV-505 sensor head is being used with an OFV-5000 Vibrometer controller. OFV-505 is quite sensitive equipment and can measure nanometers deflection precisely. For this purpose, we should isolate our system from structural vibrations. One of the best

ways is to use an optical table with an active vibration controlling system (isolate the system using compressor from bed of table to legs).

Since the structural vibrations are very low frequency of vibration and operation conditions of synthetic jets are far away from the frequencies compare to the structural frequencies. Details about how to select the low and high pass filter is mentioned in vibsoft user manual [62].

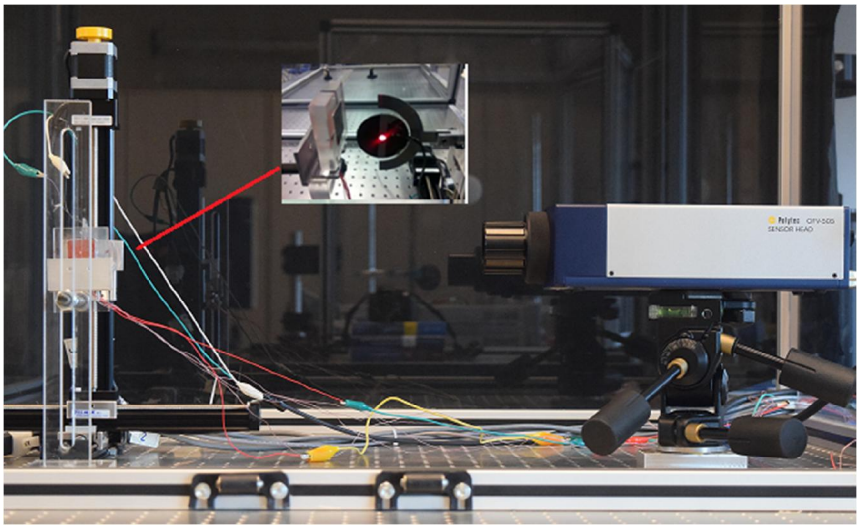

Figure 13: Experimental setup for vibration measurement.

Figure 13 displays the laser sensor head and 3D robot. Robot is holding the synthetic jet while laser pointer is focused central point on the piezoelectric actuator. A small picture of jet with laser point gives a closer look for deflection measurements. As mentioned above, the mode shape can be measured using the scanning laser [61]. Another way to estimate the mode shape is to measure deflection at five different locations in the radial direction. An Agilent function generator is used to operate at desire operating frequency and voltage. An amplifier is being used to amplify the signals from the function generator in order to reach to desire level of power given to system. For five different

piezoelectric diaphragms, deflections are measured and results will be discussed in detail for each in result and discussion section.

4.3. Velocity measurements

A TSI hotwire anemometer was used to measure the velocity coming from the synthetic jet. A Velocity measurement experimental system was developed (see Figure 14(a)). Jet exit velocity measurements were taken using a TSI IFA300 constant-temperature hot-wires anemometer system with a TSI 1210A single-axis hot wire probe (Figure 14 (b)). The sensing element length was 1.27 mm with a diameter of 3.8 µm. The sensor was parallel to the long axis of the nozzle exit and to the nozzle surface. The hot wire was calibrated prior to each test day using a TSI 1128 velocity calibrator. A compressor is used to calibrate the system feed the flow the calibrator.

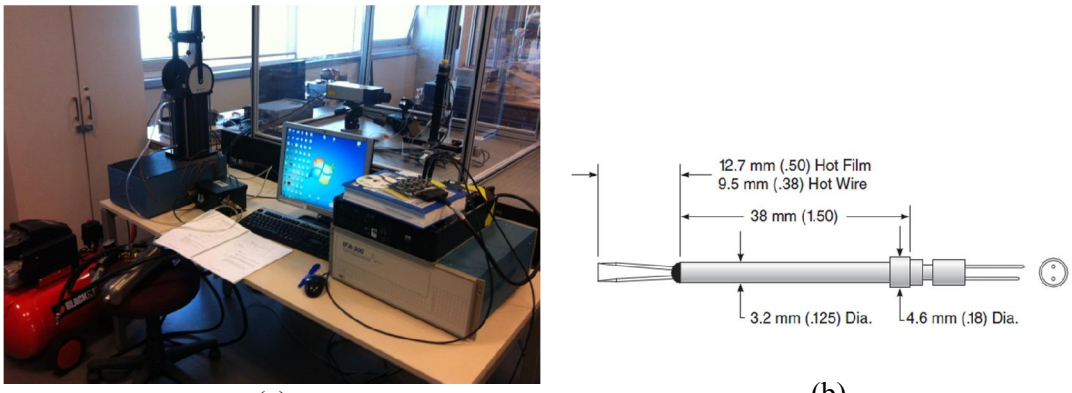

(a) (b)

Figure 14: (a) IFA300 hotwire anemometer setup (b) Single wire hot wire probe

A hotwire anemometer operates on constant temperature anemometry principle usually use to measure fine structures in turbulent gas and liquid flows. Simple convective heat transfer relations are being used for the calculation over a cylinder (wire act like a thin cylinder). When the probe faces the flow, wire cools down and the Wheatstone bridge at the back balance the bridge and provide the flow velocities.

Similarly an Agilent waveform generator and a trek amplifier are used to operate the synthetic jet on the desired operating conditions. Slot and central orifice synthetic jets are analyzed for different sizes. Detailed results will be discussed in the following sections.

4.4. Power consumption measurements

One of the advantages of synthetic jets over conventional fans is their low power consumption rate. With the same amount of flow rate a synthetic jets consume less power compared to muffin fans. Power consumption was measured for the synthetic jets at different frequencies. An oscilloscope is used with current and voltage probe to measure the power consumption of synthetic jets.

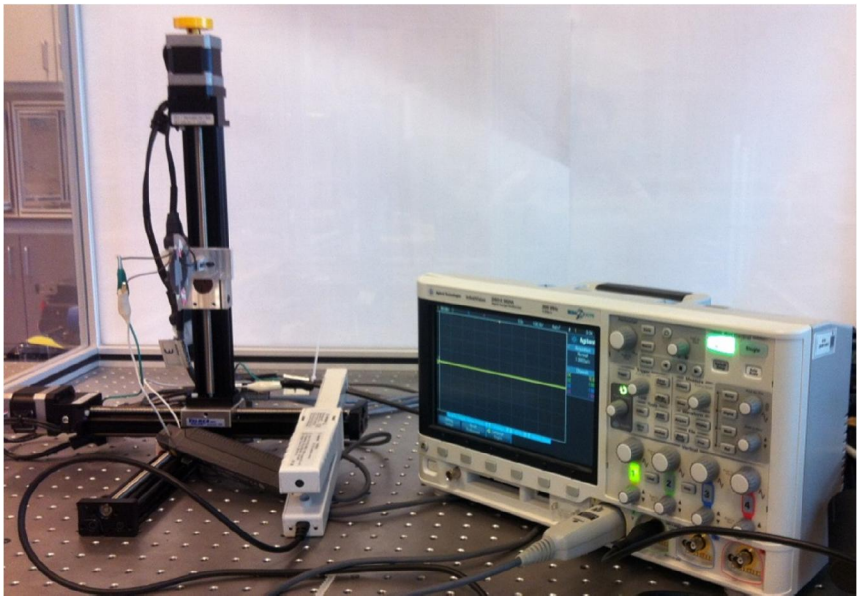

Figure 15: Power consumption measurement setup.

Figure 15 shows the experimental setup for power measurements of synthetic jets. A built-in power analyzer module is used in the Agilent oscilloscope. Another method to measure the power consumption for devices operated on AC power supply is to calculate

RMS values from the peak to peak values to get equivalent power as DC voltage and current. Conversion from peak to peak to RMS is mentioned [63] as,

$$V_{rms} = \frac{1}{2\sqrt{2}} V_{pp} \tag{24}$$

4.5. Heat Transfer Measurements

A calibrated heater is used in the thermal experiments. A heater is designed and built. A standard Kapton heater is used for the test surface. The heater is placed in between two highly conductive metal plates in order to keep the heat transfer uniform on the front surface. Four T-type thermocouples are used over a copper plate. During the experiments, less than a 0.5 ^{0}C difference was observed over the copper plate and an average of all four thermocouples are assumed to be the surface temperature of the heater. Fifth thermocouple is used to measure the ambient temperature.

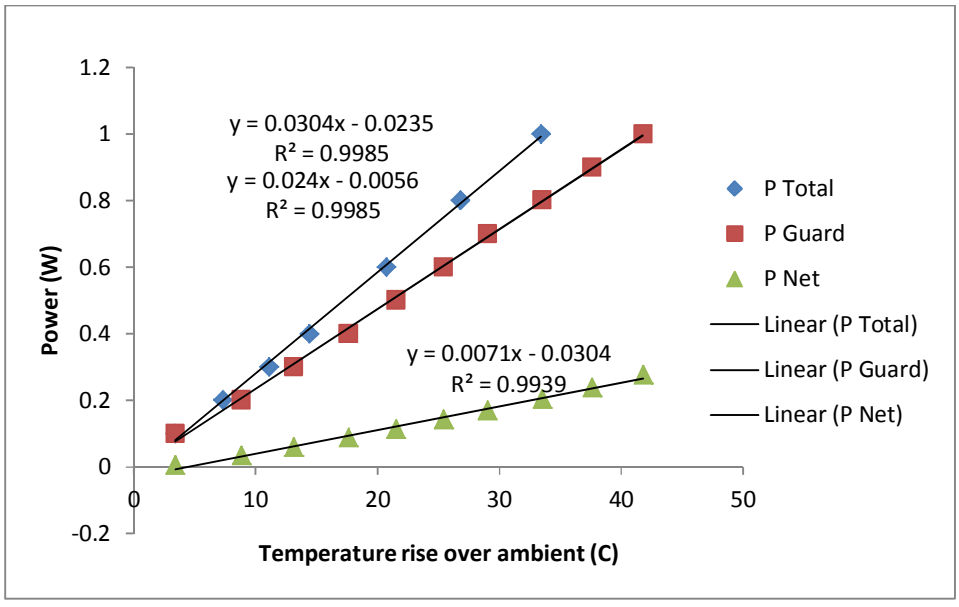

Figure 16: Heater performance test results

$$Q_s = Q_{total} - Q_{loss} \tag{25}$$

Finally, knowing the effective heater power and surface and ambient temperatures, the convection coefficient h, can be determined by the equation (26) and Nu number can be calculated using Equation (27);

$$h = \frac{Q_s}{A_s(T_s - T_{amb})} \tag{26}$$

$$Nu = \frac{Q_s D}{A_s(T_s - T_{amb})k} \tag{27}$$

Where, A_s is the surface area of the heater. Heat transfer data was collected to examine the effect of three operating parameters i.e. voltage, frequency and distance.

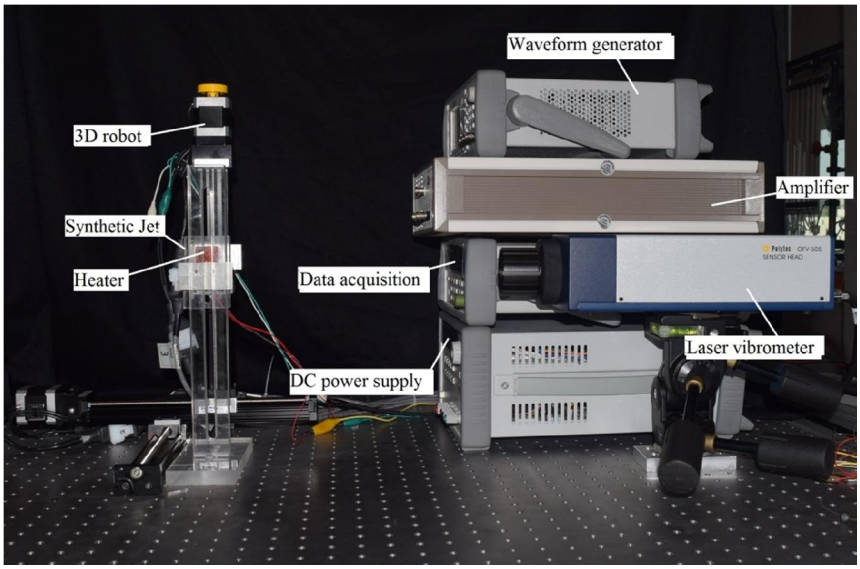

Figure 17: Heat transfer measurement setup

An agilent E3834A DC power supply is used to power up the heater. Since a small 1 inch kapton heater is used, heater surface can be considered as an isothermal surface. Agilent data acquisition and waveform generator are connected using USB port with the computer, DC power supply is connected serially with computer with a 9 pin RS-232 cable. A Velmex robot has two controllers that are needed to connect with computer

simultaneously. One USB and one RS-232 connection is created to control the robot using computer.

An indigenously made LabView [64] PID controller is used to control the surface temperature of heater to a desired value (40 ^{o}C, 60 ^{o}C and 80 ^{o}C). Values from four thermocouples were used as input for DC power supply. System was comparing average of 4-heater thermocouple readings with the set value and was giving the command accordingly. After reaching the steady state condition, temperature and power values were recorded.

Currently system is capable of conducting fully automated experiments. A notepad file is needed for the all operating conditioned in it with different values of voltage, frequency and distance of the jet from heater. System is waiting to maintain the desire temperature over heater surface and saving reading and moving to next reading and at the end of experiment stopping all the equipment.

4.6. Experimental uncertainty and repeatability

Reliability of an experimental study relies on the repeatability and low uncertainty. Therefore, over the last three decades researchers have given an increasing amount of attention so more reliable data has been generated. In 1988, Moffat [65] mentioned that experimental data will not be accepted without mentioning the uncertainty involves in the experiments. Uncertainty analysis is not only essential in writing experimental data but also more useful to point out the possible cradles of residual error at the first stage of an experiment build-up. A number of sample analyses was collected and described different parameters. Equation (28) and (29) presents the same equation mentioned by the Moffat for Nu and Re numbers.

$$\delta Nu = \left[(a_1\delta Q_s)^2 + (a_2\delta D)^2 + (a_3\delta A_s)^2 + \left(a_4\delta(T_s - T_{amb})\right)^2 + (a_5\delta k)\right]^{\frac{1}{2}} \quad (28)$$

$$\delta Re = [(b_1\delta\rho)^2 + (b_2\delta U)^2 + (b_3\delta D)^2 + (b_4\delta\mu)^2]^{\frac{1}{2}} \quad (29)$$

Where a_i(i=1…5) and b_j(j=1…4) are the sensitivity coefficients as shown in equation (28) and (29). δ shows the uncertainty in front of corresponding variable in equation (28) and (29). Major sources of uncertainty for the experiments were identified as the heat losses through the heater holder, temperature measurements and heater power measurements. A set of separate heat loss experiments was performed for the heater to quantify the heat losses through the substrate using guard heater. Table 3 is enlisted with the calculated sensitivity coefficient for the equation (28) and (29). In the current study, RMS (root mean square) method is used to analyze the uncertainty in the experiments.

Table 3: The sensitivity coefficient given in equation (28) and (29)

Sensitive coefficient	Value	Sensitive coefficient	Value
a_1	$\frac{d}{A_s(T_s - T_{amb})k}$	b_1	$\frac{Vd}{\mu}$
a_2	$Nu = \frac{Q_s}{A_s(T_s - T_{amb})k}$	b_2	$\frac{\rho d}{\mu}$
a_3	$-\frac{Q_s d}{A_s{}^2(T_s - T_{amb})k}$	b_3	$\frac{\rho U}{\mu}$
a_4	$-\frac{Q_s d}{A_s(T_s - T_{amb})^2 k}$	b_4	$-\frac{\rho V d}{\mu^2}$
a_5	$-\frac{Q_s d}{A_s(T_s - T_{amb})^2 k^2}$		

The final calculated quantities are Nu and Re numbers for the current heat transfer study. In Nu number two different types of uncertainties are possible;

- Uncertainty propagated from the measured primary variables.
- Uncertainty including the effect of all variable mentioned by Moffat [65].

Propagation of uncertainty is measured using the RMS method using the uncertainty in the primary measured variables listed in Table 4. The values of uncertainty are taken from the least value that can be measured from the equipment. For current study, it is assumed that values of air properties like density, conductivity and viscosity are fixed.

Table 4: The uncertainty and the range of the primary variables measured

Primary variables	Absolute uncertainty	Relative uncertainty
$T_{Thermocouple}$ (K)	±0.1	-
Current(A)	±0.001	-
Voltage(V)	±0.01	-
Density(kg/m^3)	Fixed value (1.225)	-
Air conductivity (W/m-K)	Fixed value (0.0257)	-
Air viscosity(Pa.s)	Fixed value	-
Velocity(m/s)	-	2%
Length, Width, Diameter(mm)	±0.01	

Second type of uncertainty is measured by repeating the experiment several times for different operating conditions. Table 5 shows some of the experimental sampling that had been made in order to calculate the standard deviation and error (%) in Nu number.

Table 5: Experimental results and (%) error in measured Nu numbers

Hz,mm,Volts	Test 1	Test 2	Test 3	Test 4	Standard Deviation	%Error
0,10,20	11.22	10.90	12.27	11.36	0.58	5.15
100,10,20	17.41	14.21	15.37	18.90	0.99	5.62
200,10,20	26.57	26.44	25.69	28.31	1.10	4.14
300,10,20	51.79	54.34	56.93	54.85	2.11	3.87
400,10,20	85.05	84.86	87.24	84.31	1.28	1.50
500,10,20	80.77	80.14	80.68	81.75	0.67	0.83
600,10,20	46.47	44.62	50.06	46.62	2.27	4.83
700,10,20	31.15	33.42	33.22	30.33	1.53	4.78
800,10,20	20.22	22.02	19.83	21.72	1.08	5.18

The maximum error found related using standard deviation method is 5.2%, while error from uncertainty propagation is 4.6%. Error calculated from sampling is greater than uncertainty propagation which is why uncertainty in heat transfer using standard deviation is greater that is why 5.2% experimental uncertainty is taken as our uncertainty.

Propagation of uncertainty is also included in the uncertainty calculated by the sampling. Similarly in Re number the measured variables are diameter of the orifice and velocity. It is mentioned by the manufacturer that there is 2% uncertainty in velocity measurements and maximum uncertainty found in Re number is around 2.9%. Detailed analysis of uncertainty propagation is shown in Appendix A.

CHAPTER V

5. RESULTS AND DISCUSSIONS

5.1. Mode Shapes and Deflection Measurements

Every dynamic system has some mode shapes that they follow whenever they are excited using some kind of force. Different geometric formations are followed by the system for different magnitude of the exposed forces. Figure 18 show different mode shapes for the circular vibrating membrane fixed from its periphery. It is seen that the number of peaks increases as the mode shapes increases. Deflection at the center is needed to actuate the synthetic jets. Mode shapes given in the first row have deflection at the central points.

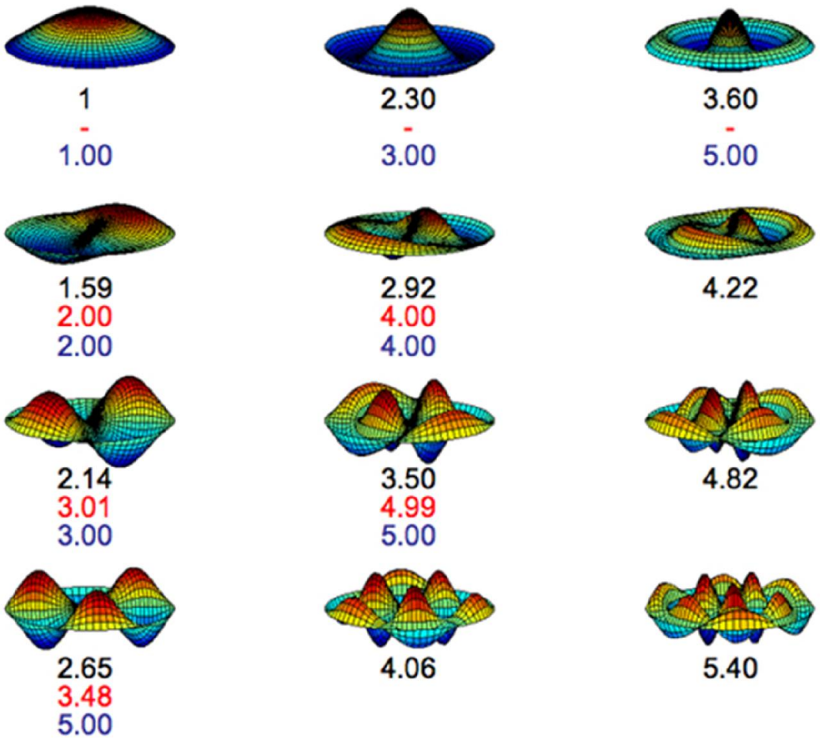

Figure 18: A set of mode shapes for the diaphragm [66]

Modal analysis has been done to analyze the fundamental frequencies for the circular diaphragm fixed from the periphery. In order to determine the basic mode shapes and their resonance frequency response, a modal analysis of the diaphragm is conducted using Comsol 4.0. Number of parameters affects the fundamental resonance frequencies of diaphragm fixed from the periphery. Basic parameters are material property of the diaphragm and geometric property of the diaphragm (diameter and thickness). Figure 19 shows four fundamental mode shapes for the circular diaphragm. Figure 19 (a) shows the first mode shapes for the circular diaphragm fixed from the periphery, maximum deflection is observed at the center of the diaphragm. This mode shape is required to operate synthetic jet at low frequencies, since first mode shape of every device is the lowest resonance that structure can operate. It is also observed that the shape of vibration is like a half standing wave. Figure 19 (b) shows the second mode shape. If the excitation force is increased, system will oscillate at it the second mode as shown in Figure 19 (b). It is observed that maximum deflection for the second mode occurred at two different positions, one in the positive direction and second in negative direction. In the third mode shape as shown in Figure 19 (c), it is shown that diaphragm is divided into four different parts, two of them move in positive direction while two of them move in negative direction.

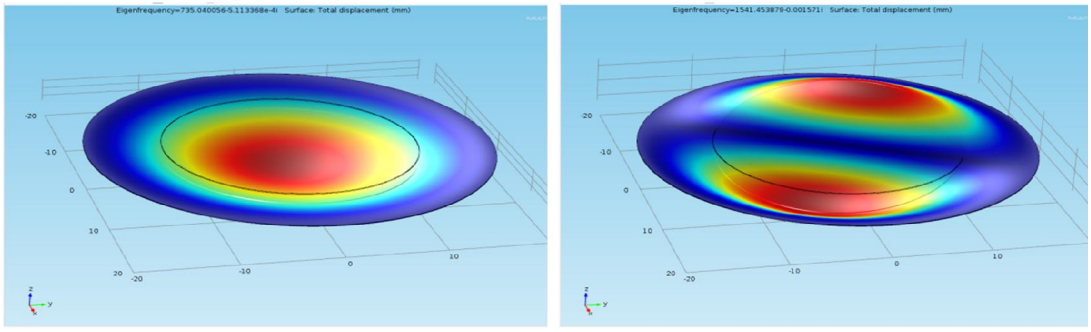

(a) (b)

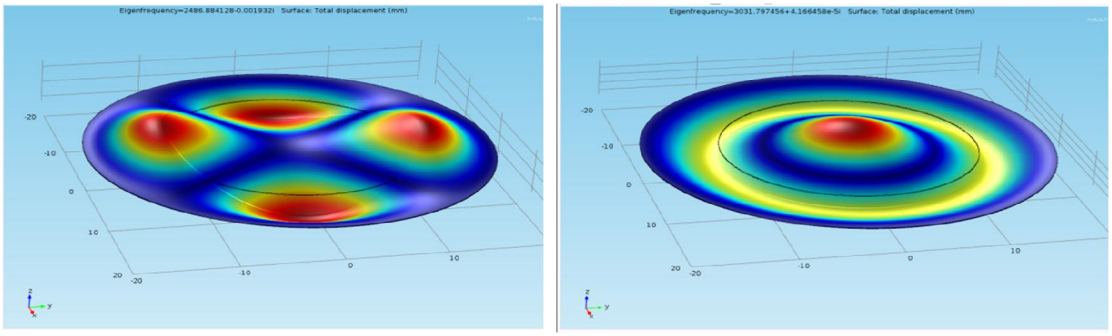

(c) (d)

Figure 19: Mode shapes for circular diaphragm measured using Comsol

Figure 19 (d) shows the fourth mode shape calculated using Comsol and third mode shape according to the mode shape mention in Figure 18. One common thing has been observed between the first and the last mode shape shown in Figure 19 is the maximum deflection occurs at the central point while in the other two mode shapes shown in Figure 19 have maximum deflection not at the center. In order to build a high frequency synthetic jet, 3rd mode shape is very critical.

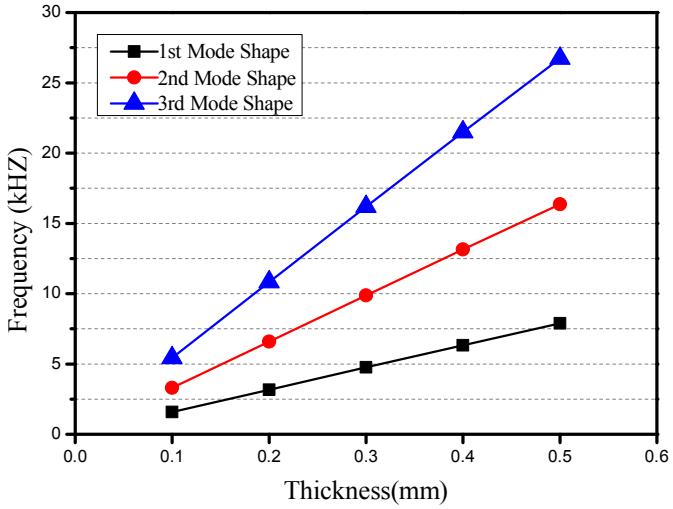

Figure 20: Structural resonance frequencies for different mode shapes

A set of modal analysis has been done in order to understand the effects of diameter and thickness over the resonance frequency of a synthetic jet. In the first figure, the diameter of the diaphragm diameter is kept constant (25 mm) while in Figure 21 thickness was kept constant (0.1mm). Material of the diaphragm was assumed to be constant in both cases as structural steel and piezoelectric material (PZT-5A). Figure 20 shows the change in the structural resonance with respect to the change in the thickness of the diaphragm. It is clear from the figure that as the thickness of the diaphragm increases the resonance frequency increases. It is shown in equation (9) when the thickness increases the stiffness of the diaphragm increase that causes the increase in structural resonance. Synthetic jets need thin diaphragms, since increase in stiffness can decrease in the deflection of the diaphragm for the given amount of force. Figure 20 and Figure 21 both show first three structural resonances for the diaphragm.

Figure 21 illustrates the change in structural resonance frequency of the diaphragm fixed from its periphery with respect to its diameter. It is observed that as the diameter increases the structural resonance decreases. An exponential decay is observed. For these set of modal analysis, the thickness was fixed to 0.1 mm and the material is the same as structural steel and PZT-5A. In Figure 21 when diameter is 25 mm the structural resonance for 1^{st}, 2^{nd} and 3^{rd} mode shapes are near to each with the range of few kHz, on the contrary when the diameter reaches to 5 mm this difference become significant and large gap between the structural resonance can be seen. This point is the starting point for the building of a high frequency synthetic jet. Smaller diameter has an advantage that the difference between 1^{st} to 2^{nd} modes shapes is separated with a significant difference of resonance frequencies.

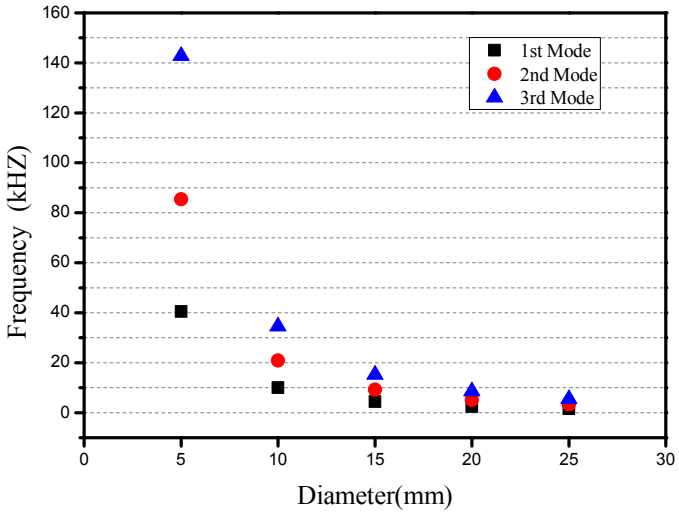

Figure 21: Structural resonance frequencies for different mode shapes of various diaphragm diameters

Table 6 illustrates the calculated driving and Helmholtz resonance using equation (9) and equation (10) respectively. Calculated frequencies are shown in descending order of the size of synthetic jets, one thing can also confirm from that results of the modal analysis and analytical calculation that structural resonance increased as the diaphragm decreases. Equation (9) is only able to capture first resonance frequency for other mode shapes advance correlations are needed (root of Bessel function etc.).

Table 6: Structure and Helmholtz resonance for analyzed jets

Jet type	Driving frequency	Helmholtz resonance
ART4500	358.36	1243.66
ART 4000	689.02	1625.62
ART3500	1184.78	1923.66
ART 2000	3961.87	2275.25
High frequency jet	4744.236734	15060.69894

In Table 6, Helmholtz cavity resonance is also calculated using equation (10) by using the geometric parameters given in Table 1 and Table 2. It is also observed that as the cavity size reduces cavity Helmholtz resonance increases. Helmholtz resonance is an

acoustic property of the system can be altered using different parameters like height of the cavity, orifice size and cavity size etc. Cavity Helmholtz plays an important role in order to determine the flow regime in the synthetic jets. If operating frequency match with the cavity Helmholtz, flow can be considered as compressible otherwise it will be considered as incompressible [33].

Driving resonances calculated mentioned in Table 6 using equation (9) are deviating from the resonance calculated by experiments and computational as shown in the Figure 22 to Figure 26. After analyzing the equation (9) it can be inferred that following formula cannot be used to capture the effect of the piezoelectric actuator on top for the diaphragm. Any increase in the stiffness of the diaphragm can cause increase in the structural resonance, which is observed from deflection measurement results.

Two different voltages have been applied for slot orifice jet and circular orifice jet. For slotted orifice jet 35 Vpp was applied while for the circular jet was excited using 20 Vpp. A modal analysis of each individual diaphragm was also completed in order to determine the operating range for the first mode. Figure 22 shows the measured deflection of ART4500 jet experimentally and computationally. Experimental and computational values are in a good agreement with each other except for a couple points although air damping was neglected. We believe that it still has some effect on the performance. Resonance frequency of this jet found to be about 480 Hz providing a peak deflection of 105 μm experimentally. As it is mentioned in Table 1 and Table 2 that ART4500 and ART3500 are slotted orifice jets while ART4000, ART2000 and high frequency jet are central circular orifice jet. The same boundary and operating conditions applied to ART3500 jet. This jet is slightly smaller than ART4500 jet with an outer diameter of 35

mm. Disk deflection has been measured and it is found that experimental and computational results showed a similar trend.

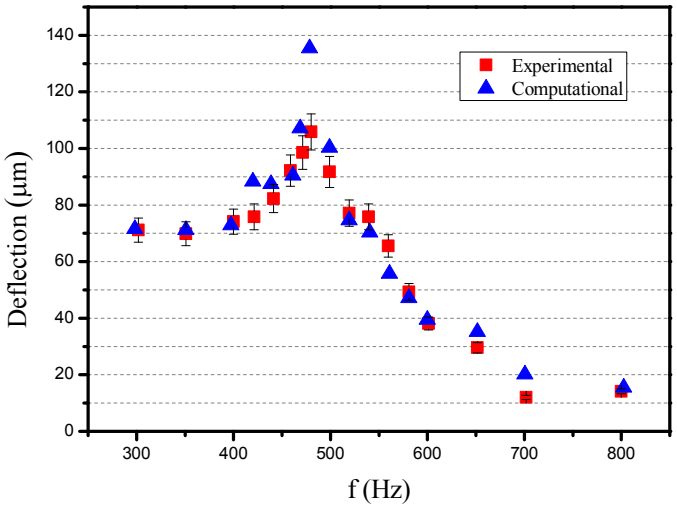

Figure 22: Effect of frequency on ART4500 diaphragm deflection

By comparing Figure 22 and Figure 23, one can see that peak deflection is shifted from 480 Hz to 1200 Hz. This is due to the fact that the resonance frequency is highly sensitive to the disk geometry as mentioned above. Piezoelectric actuators usually operate near or at the resonance points in order to get maximum air out from the orifice. ART3500 jet experienced a peak deflection of about 62 μm at 1200 Hz. This is found to be interesting while resonance increase about 2.4 times, and deflection dropped about 45% compared to a larger synthetic jet.

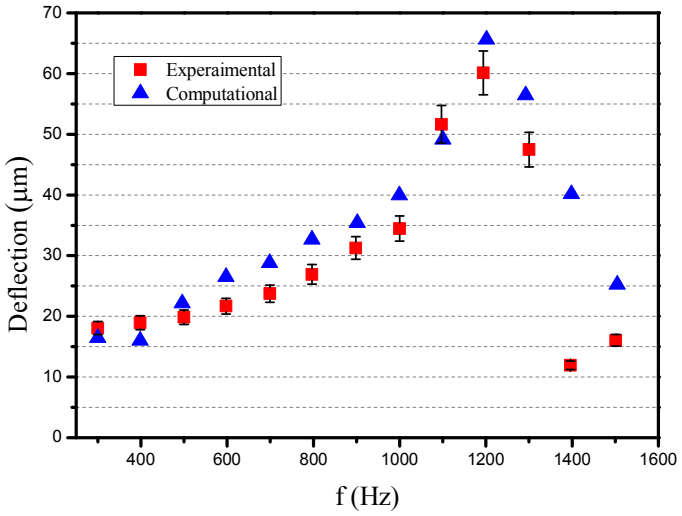

Figure 23: Effect of frequency on ART3500 diaphragm deflection

ART4000 jet deflection was measured for a range of 100 Hz to 1000 Hz, with an interval of 50 Hz in order to capture the deflection for the first mode. Figure 24 shows the measured diaphragm deflection for ART4000 at the resonance frequency (700 Hz). The maximum experimental deflection result was observed around 46 μm while the maximum computational result was around 60 μm. Although during the time dependent study of a synthetic jet, air damping was neglected, computational methods are still valuable to predict behaviors of an actuator. Operating synthetic jets at point close to the structural resonance frequency is preferred, because operating away from the resonance deflection degrades. Figure 25 shows the variation of frequency with deflection for the small synthetic jet (ART2000). The same behavior was observed for other jets except for the values of deflection and resonance frequency. As it is discussed earlier, while the size decreases, resonance frequency increases. ART2000 synthetic jet actuator was smaller than ART2000, ART4000 and ART3500 that is why the resonance frequency shifted from 700 Hz to over 4000 Hz, as shown in Figure 25.

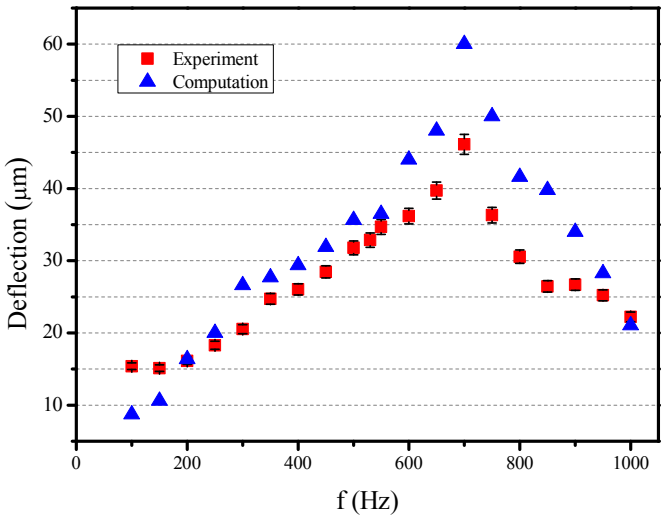

Figure 24: Effect of frequency on ART4000 diaphragm deflection

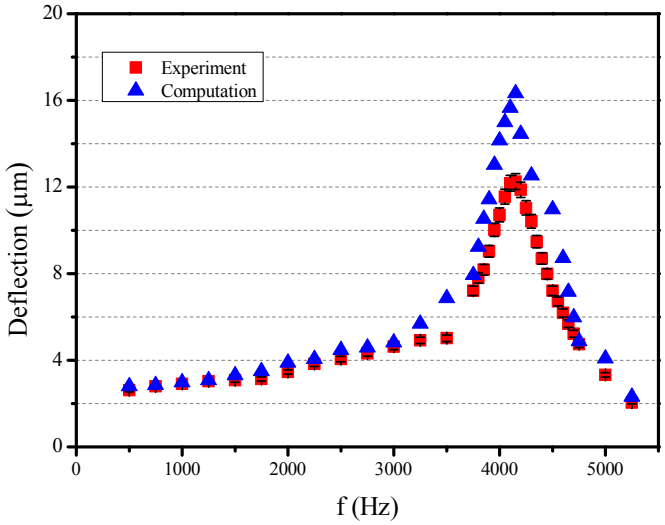

Figure 25: Effect of frequency on ART2000 diaphragm deflection

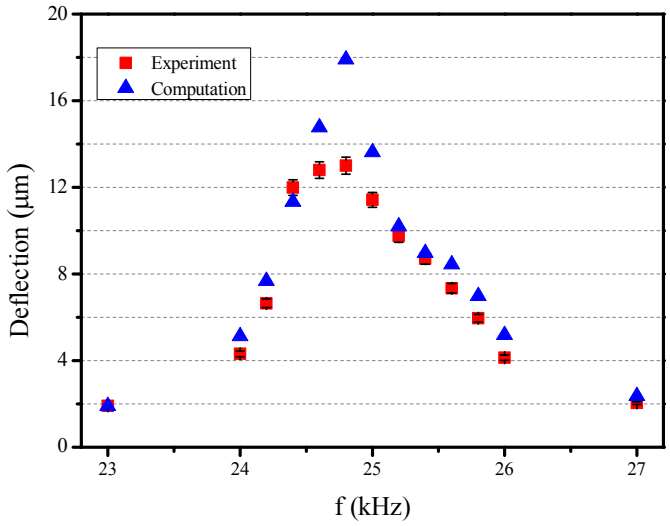

Figure 26: Effect of frequency on high frequency jet diaphragm deflection

In order to perform a fair comparison, a 20 Vpp driving voltage was applied to all three synthetic jets. It was found that as the operating voltage increases, the amount of deflection increases linearly [32]. Deflection measurements for the high frequency jet are shown in Figure 26. The maximum measured deflection at the resonance was around 13 μm, while computational models predicted 17 μm. The differences are due to the air damping neglected in the models. For a high frequency synthetic jet, 20 Vpp is a harsh operating condition which is why the deflection shown in Figure 26 is more than the one stated by the manufacturer [67]. Manufacturing and packaging plays an important role in resonance frequency, it is possible that initial structural resonance can be differ from the operating frequency with final product.

5.2. Velocity measurements

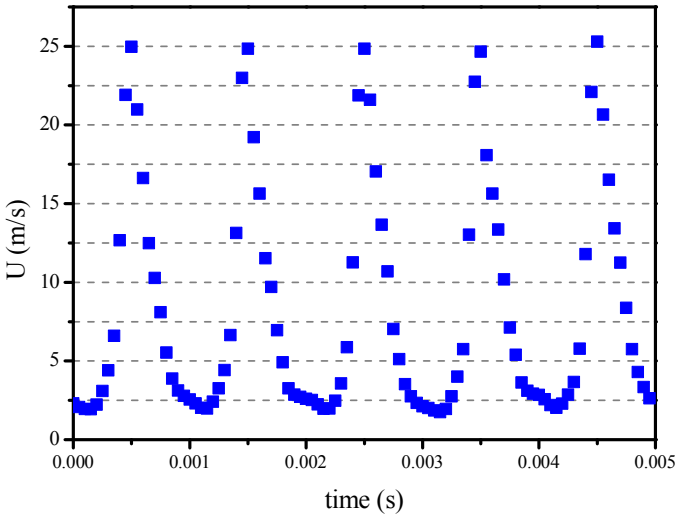

Figure 27: Variation of jet exit velocity with time for ART4000 at 700 Hz

Jet exit velocity measurements were performed by using a TSI IFA300 constant temperature hot wire anemometer system, with a single axis hot wire probe. The hotwire was calibrated prior to each test using an automatic calibrator (TSI-1129). The measurements were taken for three different synthetic jets located 1 mm away from the orifice. Figure 27 displays instantaneous absolute exit velocity with respect to time for the ART4000 jet at the resonance frequency of 700 Hz using single axis probe at 20 Vpp. Single axis probe is able to measure only the absolute component of the velocity. The periodic nature of the air stream was quite clear where the peak velocity was observed during the ejection phase and dropped afterwards. This is a typical and expected profile for synthetic jet devices. For heat transfer, peak exit velocity plays an important role and demands more attention.

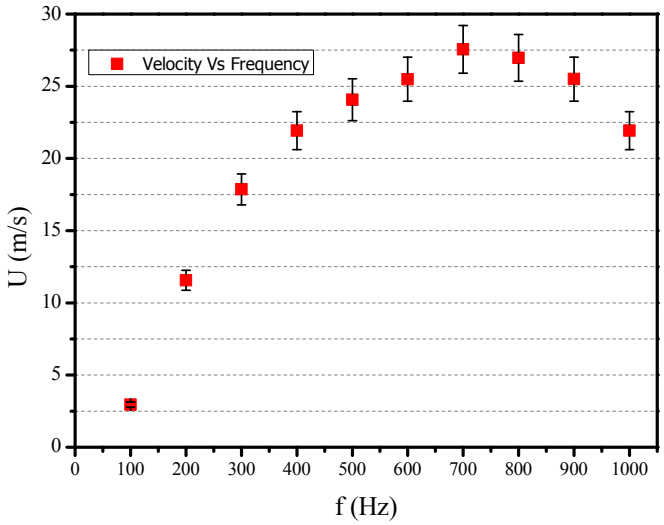

Figure 28: Effect of driving frequency for ART4000 jet exit velocity

The peak velocity results are summarized in Figure 28, Figure 30 and Figure 31.The peak jet velocity for ART4000 was scanned between 100 and 1000 Hz. The peak jet velocity for ART2000 was scanned between 1000 to 5500 Hz. The peak jet velocity for high frequency jet was scanned between 23 to 27 kHz. Figure 28 shows the peak exit jet velocity for ART4000, a similar trend was observed in the deflection measurements.

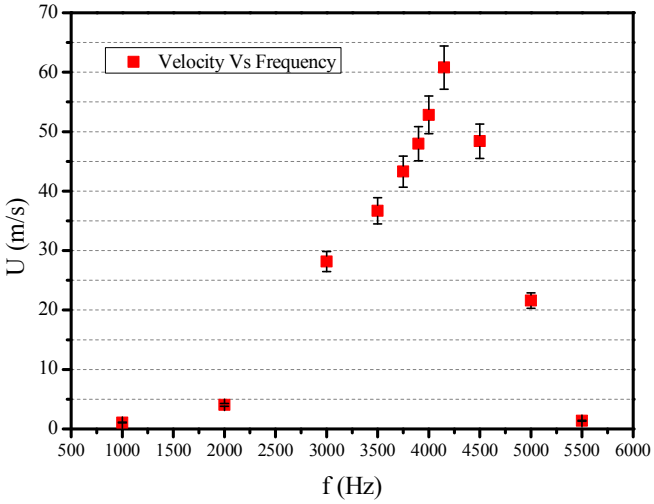

Figure 29: Variation of velocity with driving frequency for ART2000 jet

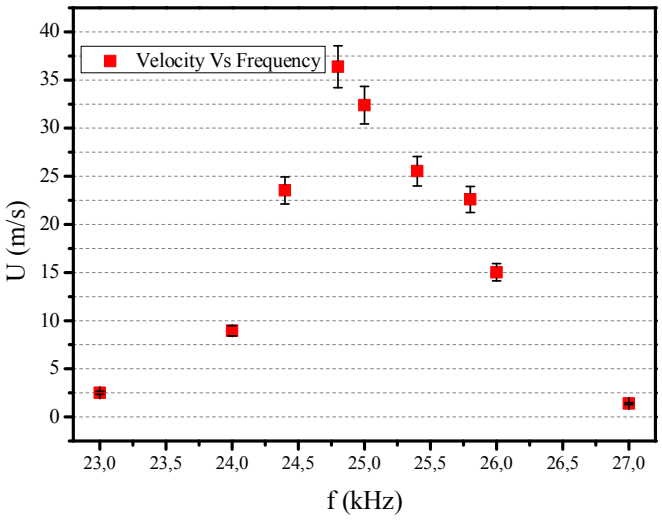

Figure 30: Variation of high frequency synthetic jet exit velocity with driving frequency

As it was mentioned before, operating piezoelectric actuators away from the resonance frequency does not give enough deflection to expel a strong stream of air from the cavity. Table 6 shows that Helmholtz cavity frequency for ART4000 is over 1600 Hz, so air is incompressible and has no effect on the air coming out of the jet orifice [32]. For ART4000 maximum velocity was measured as 26 m/s at 700 Hz, for ART2000 was almost 60 m/s and for high frequency synthetic jet was found around 36 m/s as shown in Figure 28, Figure 30, Figure 31.

5.3. Heat transfer measurements

Four T-type thermocouples were placed under the heated surface. The average heater surface temperature was determined based on four distinct point measurements from a copper surface. Total heat transfer from the vertical heater was calculated using equation (30),

$$Q_{total} = Q_{heater} + Q_{loss} \quad (30)$$

The average Nu number over a 1 inch vertical heater surface was determined. Since the copper has a high thermal conductivity, the temperature gradient of the surface was less than 0.1 ^{o}C. Therefore, this heater, assumed to be isothermal and it met the need of the present study. Figure 31 and Figure 32 show average Nu number for the slot jets (ART4500 and ART3500). It is mentioned prior that applied voltage for the slot jets is 35 Vpp. The surface temperature was fixed for all heat transfer experiments as 60 ^{0}C. At early stage the surface temperature of the heater was maintained manually by playing with DC power supply with hand that is why for slot jet only Nu number was calculated over a range of frequency. Later, a PID controller was used to maintain the surface temperature over heater which had reduced the time required to get data for single data point, which enable us to sweep the distance along with the frequency sweep.

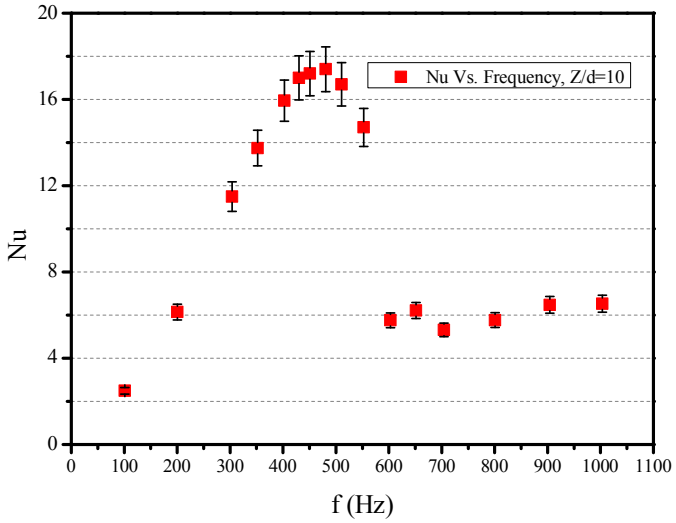

Figure 31: Average Nu number for various frequencies at 35 Vpp for ART4500

Figure 31 shows the average Nu number distribution over a frequency range of first mode shape for ART4500 at the dimensionless distance (Z/d) of 10. Error bars are shown with each point is showing uncertainty in the experimental data that was mention in section experimental uncertainty. Increasing and decreasing behavior like deflection is observed initially increases with increase in frequency and after crossing the resonance of the particular jet decreases. ART4500 showed maximum heat transfer rate at 480 Hz which considered being resonance when deflection was measured.

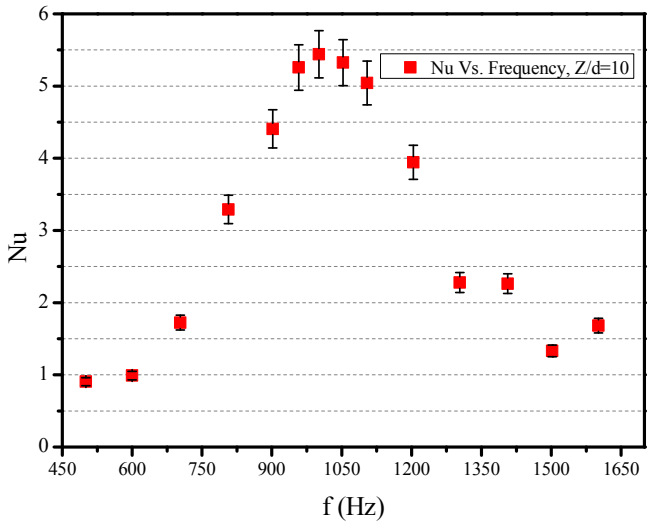

Figure 32: Average Nu number for various frequencies at 35 Vpp for ART3500

Figure 32 illustrates the change of behavior of average Nu number with respect to the frequency changing from 500 Hz to 1600 Hz at the dimensionless distance (Z/d) of 10. Peak Nu number for ART3500 found to be around 1000 Hz which is deviating from the resonance found using laser vibrometer. It can be inferred that perhaps a coherent votrical structure did not have enough time to develop at high frequency of 1200 Hz and flow similar to continuous stream jet is produced and boundary layer can be develop that can

reduce the heat transfer compare to low frequency at 1000 Hz. First point which is shown in Figure 32 has a Nu number of less than one, which means that flow produced by synthetic jet reduced the heat transfer as compared to natural convection. Sometimes at really small flows, pressure forces and buoyant forces magnitudes are comparable to each other. As one know that natural convection boundary layer started from the bottom of the plate and continues to the end of the plate and fluid become hot after getting heat from the hot surface and leads to lower in density and move in upward direction. When small flow disturbs the flow which leads to results either increase in heat transfer or decrease in heat transfer. If the flow created by natural convection is assisted by the forced convection flow, heat transfer will increase, in other case it will decrease. In the current case, with the first data point the same thing happened which reduces the Nu number less than one. Since most of the synthetic jet operates near to resonance frequency the mixed convection criteria does not apply on it.

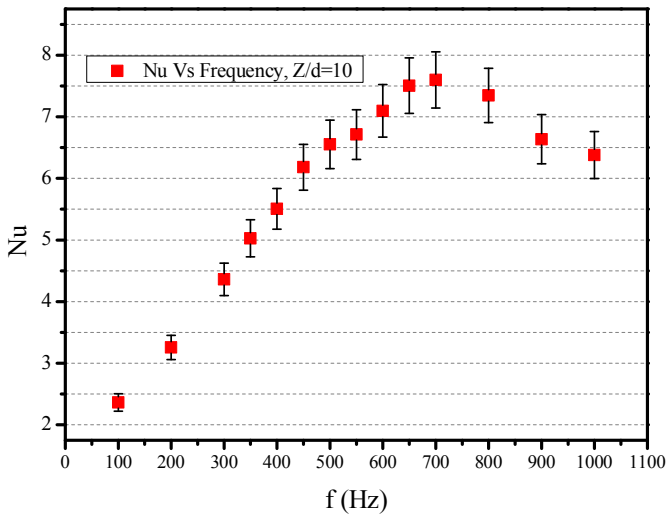

(a)

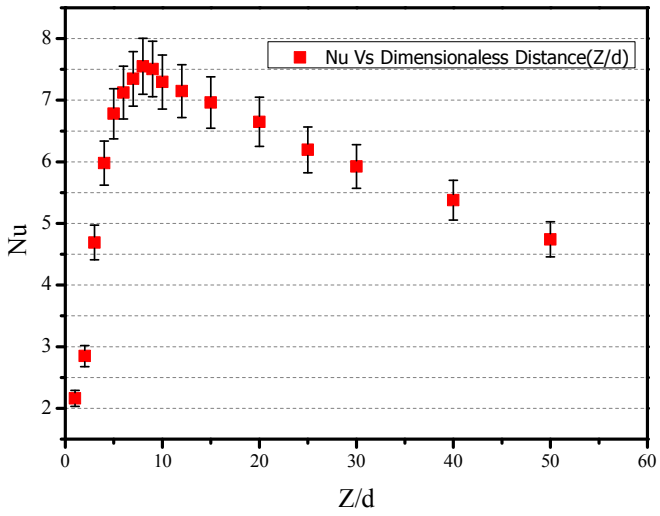

(b)

Figure 33: (a) Average Nu number for various frequencies at 20 Vpp for ART4000 (b) Nu number over dimensionless distance for ART4000 at resonance frequency

Figure 33 shows the average Nu number for ART4000. Figure 33(a) shows the average Nu number for ART4000 with respect to frequency sweep at the dimensionless distance (Z/d) of 10 with an applied voltage of 20 Vpp. It is shown that as the frequency increased towards the resonance Nu number also increases. It can be inferred that strong vortex rings were generated and caused a large amount of heat transfer. It is observed that piezoelectric actuators have less deflection before and after the resonance frequency. Deflection plays an important role in heat transfer which shown in the Figure 31, Figure 32 and Figure 33(a). Voltage is another parameter that affects heat transfer. The higher voltage applied to the jet, the higher amount of heat removed from the heater surface [68]. Figure 33(b) presents the effect of dimensionless distance between the orifice and heater surface on Nu number at the resonance frequency of the ART4000 synthetic jet. Initially average Nu number increases as the distance increases. After it reaches the maximum, it

gradually decreases. In the vicinity of the heater, vortex rings may not have enough space to develop, which results in less heat transfer. Secondly, it reaches a place where the maximum heat transfer is observed, so, vortex rings may have formed completely and reached the heater. Later, a gradual decay was observed which may be related to the transition from the regime dominated by strong vortical structures to the flow dominated by stochastic turbulence [43]. A similar behavior was reported for a magnetic actuator [34]. Heat transfer can be increased while operating the jet at the cavity resonance frequency [35]. In the case of ART4000, driving frequency and cavity resonance are not close to each other as shown in Table 6. Hence, cavity resonance has no effect on the performance of the 40 mm jet. The ratio of the heater area to the orifice area also plays an important role in heat transfer. If the size of the orifice is small, a peak will occur at a high Z/d ratio compared to bigger orifice or if the heater size is larger.

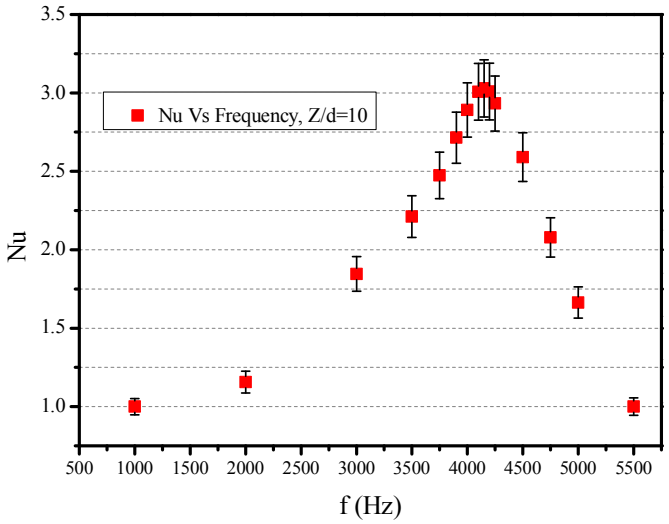

(a)

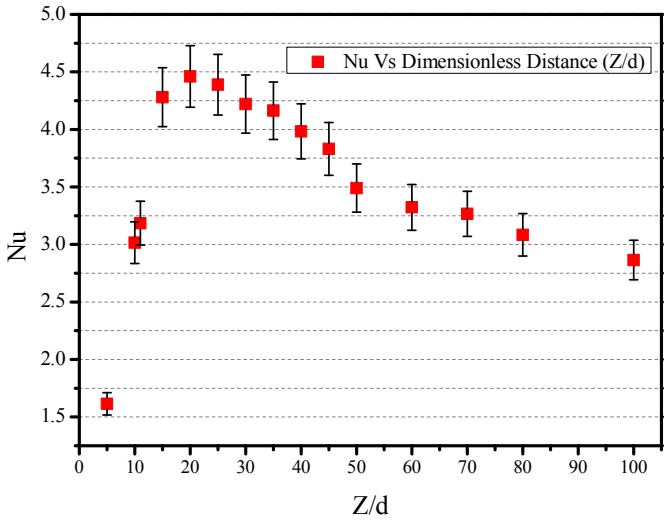

(b)

Figure 34: (a) Average Nu number for various frequencies at 20 Vpp for ART2000 (b) Nu number over dimensionless distance for ART2000 at resonance frequency

Figure 34 (a) shows average Nu number for the ART2000 for a range of frequencies from 1000 to 5500 Hz. The same trend was observed with ART4500, ART3500 and ART4000 which initially increased in frequency and caused an increase in Nu number until it reached the resonance frequency and then decreased. This is due to the fact that the size of the orifice is smaller than ART4000 and it has a higher peak exit velocity shown in Figure 28 and Figure 29. On the other hand, Nu number of the ART4000 is more than ART2000 which may lead that volume flow rate of ART4000 is greater than ART2000, as shown in Figure 28 (a) and (b). Maximum Nu number for ART2000 is around 3 which is equal to half of Nu observed for ART4000 at the resonance frequencies. Figure 34 (b) shows Nu number with respect to dimensionless distance. It was observed that peak heat transfer at dimensionless distance of 20 proves that the area of the orifice and the area of the heater play an important role. Another reason could be

the transition from the regime dominated by strong vortical structures to the flow dominated by stochastic turbulence.

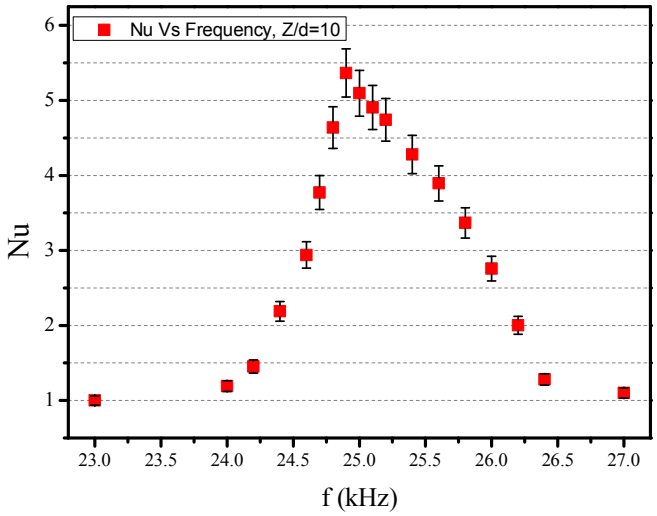

(a)

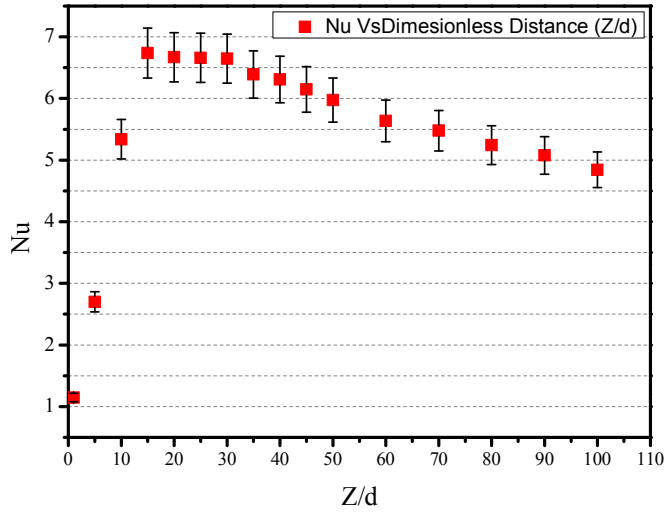

(b)

Figure 35: (a) High frequency synthetic jet average Nu numbers vs. frequency sweep various frequencies at 20 Vpp (b) Variation of high frequency jet average Nu numbers with dimensionless distance

Figure 35 (a) and (b) presents heat transfer data for the high frequency synthetic jet. Maximum heat transfer for the high frequency synthetic jet was found to be around 24.8 kHz. The maximum Nu number was about 5.5 for Z/d equal to 10. The study of heat transfer with respect to dimensionless distance for the high frequency jet also showed a trend similar to ART2000 and with a maximum of heat transfer around Z/d equal to 20. The peak jet velocity for high frequency jet was scanned between 23 to 27 kHz. Figure 30 shows the peak exit jet velocity for high frequency synthetic jet, a similar trend was observed in the deflection measurements also.

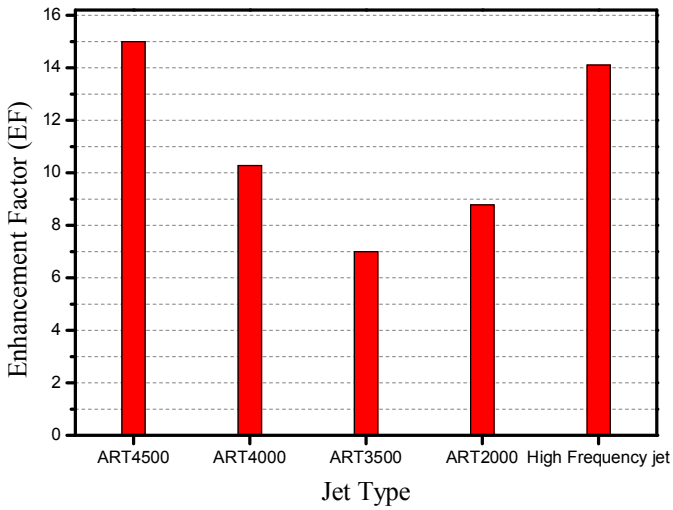

Figure 36: Enhancement factors for various synthetic jets

Figure 36 shows maximum enhancement factor that measured (EF is defined as heat transfer coefficient when jet is on over natural convection coefficient) for all five synthetic jets. It was observed that ART4500 and high frequency synthetic jet have comparable enhancement factor with each other. It is found that ART3500 has the least

EF value as compare to the all examined five jets.

5.4. Proposed heat transfer correlations

Heat transfer mechanism for steady jet and synthetic jet is different from each other. Garg et al. [69] studied synthetic jet and presented a correlation for prediction of heat transfer for a single slot impingement jet [70] with a limited data set for a 12 mm piezoelectric jet with a resonance frequency of between 3500 and 4500 Hz. Arik et al. [68] later presented another correlation for low a frequency synthetic jet ($300 < f < 800$ Hz) with an extended data set. It is observed that Nu number predicted by Arik et al. correlation offers a good agreement up to 600 Hz for slot jet. After resonance frequency jet prediction capability significantly degraded. Correlation by Arik et al. focused on slot orifice jet, which is why here it is neglected in order to create correlation for the slot orifice jet those are examined in this study.

In the present study, a broad correlation is proposed to capture the cooling effect over a heated vertical surface for annular synthetic jets. Since air is used as a working fluid for electronics cooling applications, the effect of Pr number in the correlations was not examined. A typical form for the average Nu number is given as;

$$\mathrm{Nu} = \alpha \mathrm{Re}^{\beta} \left(\frac{f}{f_n}\right)^{\gamma} \left(\frac{A_{heater}}{A_{orifice}}\right)^{\kappa} \left(\frac{Z}{d}\right)^{\nabla} \tag{31}$$

The proposed correlation from Arik et al. [68] was for a slot orifice synthetic jet. In a slotted jet, dipole vortices are generated; while, in a circular jet, vortex rings are produced. A large number of data points were used to develop two different correlations for low frequency synthetic jets (driving frequency <5 kHz) and for high frequency synthetic jets (f >20 kHz), since both have different flow physics and different behavior

of data with respect to the important non-dimensional parameter of the correlation. Re number is an important parameter for predicting the cooling of synthetic jets. For pulsating jets, two distinct definitions of Re number for the synthetic jet had been used, based on peak jet exit velocity [68] or the average velocity over a cycle. In the present study, the following definition is used for Re number,

$$\int_{m1}^{m2} dm = \int_{0}^{\zeta/2} \rho A u(t)\, dt \tag{32}$$

$$\frac{m_{syn,j}}{m_{imp,j}} = \frac{\frac{\cos(2.\pi.f.t))_{n\zeta+1/2.f}^{n\zeta}}{2.\pi.f}}{\frac{1}{f}} = \frac{1}{\pi} \tag{33}$$

Equations (32) and (33) show the mass flow rate for the synthetic jet and impinging jet. In order to have similarity between these two jets mass flow rates of both jets equated with each other. Finally we obtained a constant that is one over Pi. In order to have an average Re number one can divide it by pi which is calculated using maximum jet exit velocity of synthetic jet over a cycle. For the proposed correlation for a circular orifice synthetic jet definition of Re number in equation (16) is used.

The second term in equation (31) is the dimensionless jet driving frequency, driving frequency is non-dimensionalized using the structural resonance frequency. The next term in equation (31) is the ratio of surface area of heater to the area of jet orifice and the latter term is dimensionless horizontal distance between heater's surface and the jet. The coefficients were determined using the experimental data gathered for low and high frequency jets and the following correlations are developed;

$$Nu = 1.007 Re^{0.485} \left(\frac{f}{f_n}\right)^{-0.002} \left(\frac{A_{heater}}{A_{orifice}}\right)^{-0.214} \left(\frac{Z}{d}\right)^{-0.194} \tag{34}$$

$$Nu = 1.003Re^{0.727}\left(\frac{f}{f_n}\right)^{0}\left(\frac{A_{heater}}{A_{orifice}}\right)^{-0.381}\left(\frac{Z}{d}\right)^{0.006} \quad (35)$$

$Re < 1200$

$0.15 < f/fn < 1$

$5 < Z/d < 50$

Equations (34) and (35) show the proposed correlations for low and high frequency central orifice synthetic jets, respectively. It was observed that Nu number is affected more by Re number, the ratio of surface area of heater and area of the jet orifice compared to dimensionless distance and dimensionless frequency. It is shown that Nu number has the least dependency on non-dimensional driving frequency and non-dimensional distance. Nu number for high frequency jet shows almost negligible dependency on non-dimensional driving frequency and non-dimensional distance. Equation (34) and (35) captures both synthetic jet convection and radiation heat transfer. Radiation contribution to the overall heat transfer coefficient was roughly calculated and found to be less than 4% for best operating conditions (near to resonance frequency).

Figure 37 shows the comparison of calculated average Nu numbers and measured values from experiments for the complete data set with ± 25% boundaries. We have found that proposed correlations are able to predict synthetic jet heat transfer within given boundaries. However, it has also been observed that the proposed correlation for low frequency synthetic jet cannot predict less than 200 Hz, since at low frequency vortex generation is weak and we may have mix-convection regime. The correlation proposed for high frequency jets can neither predict Nu number less than 23 kHz operating frequency nor jet- to- heater -distance (Z/d) less than 5 with a reasonable accuracy. The deviation is found to exceed 25%. Therefore, those data points were not included in the current study. The effect of jet to heater axial distance needs further flow visualization

type techniques for better understanding fluid flow phenomena impinging on the heater.

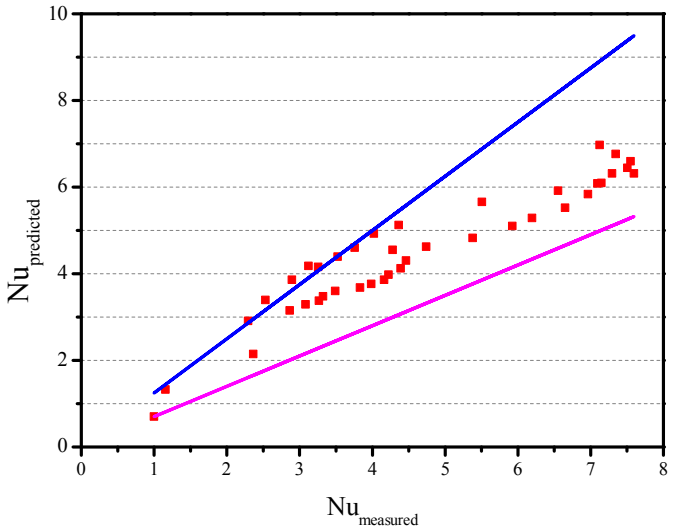

(a)

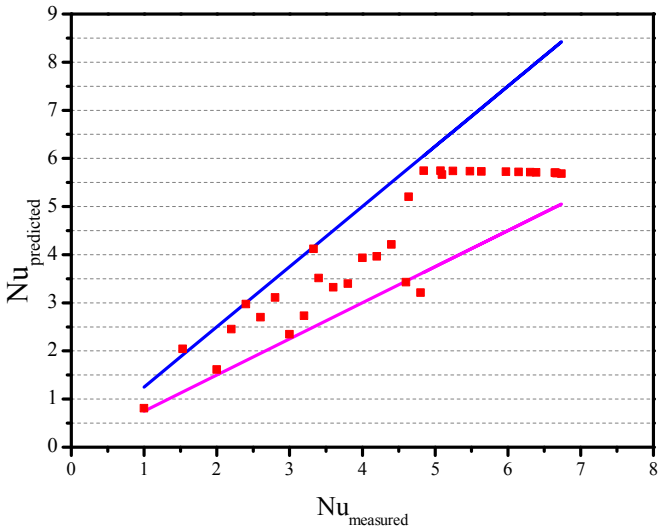

(b)

Figure 37: Variation of predicted and measured average Nu number with ± 25 % boundaries (a) Art jets (b) High frequency jet.

5.5. CFD for synthetic jets

Bulk of the computations are performed for a circular jet at $ReD_j = 1400$ and y/d = 2. Figure 38 demonstrates the instantaneous non-dimensional pressure profiles on the target plate at various times (phase angles) for f = 500 Hz. As it can be seen, the pressure coefficient at the stagnation point is positive for all the phase angles and the maximum non-dimensional pressure value (Cp = 4.9) is obtained at the second half of the exhale phase ($\varphi = 135^o$). The scaling for the pressure coefficient is based on the mean velocity at the nozzle exit, however if the maximum instantaneous velocity is taken as the reference velocity, the Cp value at the stagnation point is determined to be less than unity, i.e. Cp = 0.85, which is identical to that of an impinging jet utilizing the centerline velocity at the nozzle exit as the reference value.

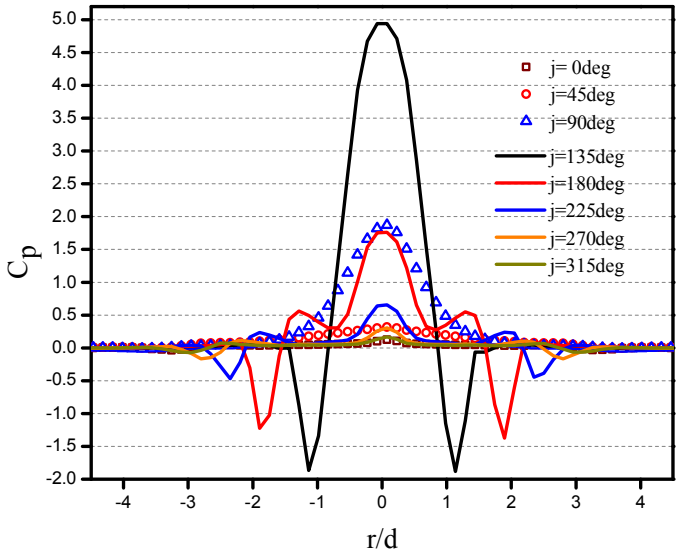

Figure 38: Pressure distributions on the target plate at various phase angles for ReD_j = 1400 and y/ d = 2.

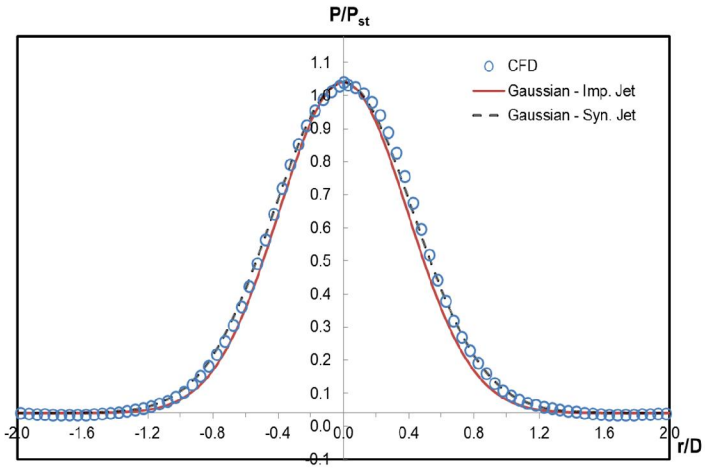

Figure 39: Time-averaged pressure distribution on the target plate.

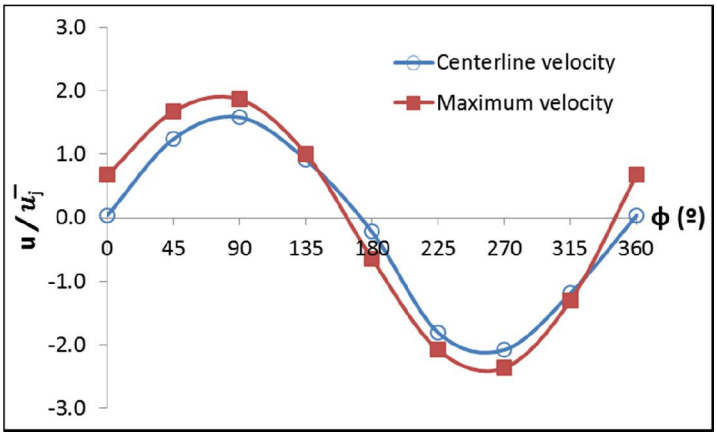

Figure 40: Non-dimensionalized centerline and maximum velocity at the nozzle exit at various φ.

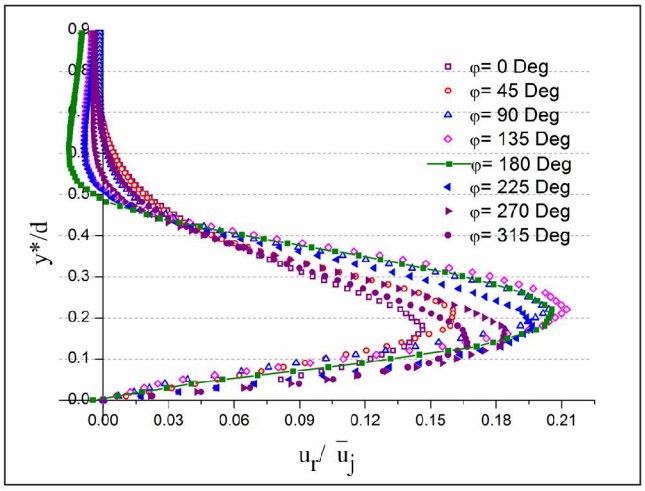

Figure 41: Non-dimensional radial velocity distributions near wall at various phase angles, r/d = 4.0, ReD_j = 1400 and y/d = 2.

Nevertheless, unlike an impinging jet, the shape of the instantaneous profiles is not Gaussian and shows negative (sub-ambient) values. At or around φ = 135°, significant (favorable) pressure gradients are seen within the close proximity of the symmetry plane/stagnation point, i.e. just within r/d ≤ 1. It is noteworthy that only the first half of the ejection phase (0° ≤ φ ≤ 90°) produces Gaussian shape pressure profiles, resembling a circular impinging jet. Figure 39 shows the time averaged pressure profile of the circular jet for ReD_j = 1400 and y/d = 2. Similar to the instantaneous profiles produced in the first half of the ejection phase (0° ≤ φ ≤ 90°), the time averaged profile is also of Gaussian. Its form is:

$$\frac{P}{P_{st}} = e^{-\beta[r/d]^2} \tag{36}$$

Where P_{st} is the stagnation pressure and β is a parameter that can be determined from curve fitting. β can also be written in exponential form as:

$$\beta = \exp(\alpha) \tag{37}$$

Where α is a constant and a function of the nozzle-to-height distance and type of the jet. While not shown here, a separate set of simulations were performed for an impinging jet at $ReD_j = 700$ and $y/d = 2$. Even though the instantaneous pressure profiles vary considerably between the synthetic jet and its impinging jet counterpart, the time averaged Gaussian profiles are just slightly different and almost collapsed into a single curve, i.e. α in Equation (37) is determined as 1.16 via curve fitting for the synthetic circular jet and it yields unity for the impinging circular jet.

Figure 40 shows non-dimensionalized centerline and maximum velocity curves in a complete cycle. As expected, the co-sinusoidal displacement input on the actuator leads to a sine-wave like velocity profile at the nozzle exit. While not shown, the exhale phase velocity profiles demonstrate wider jet core and more uniformity compared to those at the inhale phase. As can be seen from Figure 40, at a given time, maximum velocity does usually not occur on the centerline, and the difference between the centerline and maximum velocity becomes the highest at the beginning/end of the inhale/exhale phases and this behavior repeats itself after the initial transients cease.

From Figure 38, it bears noting that the instantaneous pressure gradients completely vanish at $r/d = 4$ for all of the phase angles. At this particular radial coordinate, Figure 6 demonstrates the streamwise velocity profiles near the target wall. The maximum value of the non-dimensional streamwise velocity is a function of the phase angle, however the variation is not large, i.e. $u_r / \bar{u}_j$ varies between 0.15 and 0.21. It is noteworthy that the highest of thesure maximum values ($u_r / \bar{u}_j = 0.21$) is obtained at the second half of the ejection phase, i.e. at $\varphi = 135°$, which corresponds to the angle where highest pressure gradients are observed (see Figure 38).

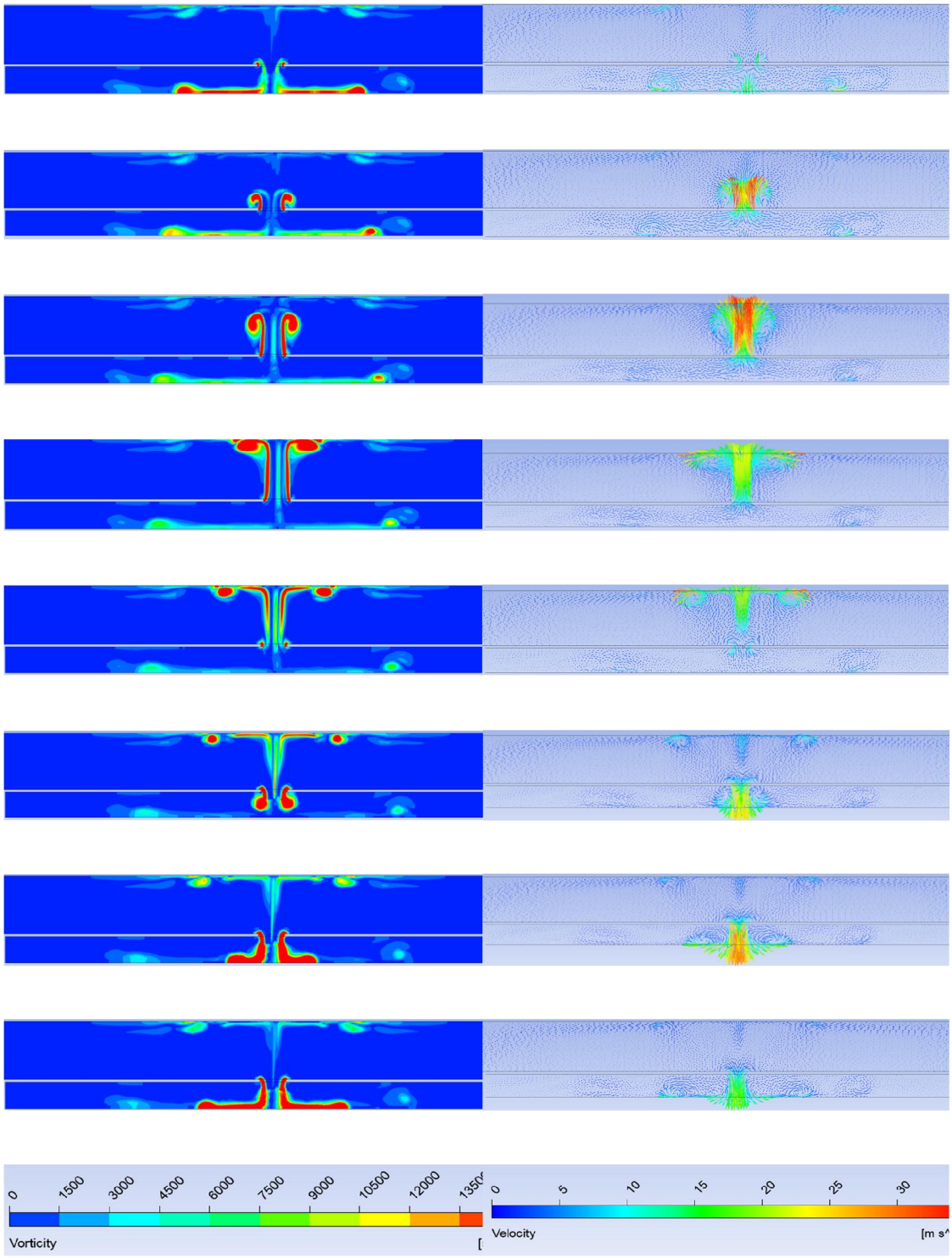

Figure 42: Vorticity contour and velocity vector plots during the ejection and suction periods for ReD_j = 1400, y/d = 2, f = 500 Hz. From top to bottom: φ =0º, 45º, 90º, 135º, 180º, 225º, 270º, 315º.

Figure 42 demonstrates the vorticity contour and velocity vector plots on a vertical plane in a full period after the initial transients die in the flow field. As can be seen, a small vortex ring is produced at the nozzle exit at the beginning of the ejection phase (φ =0º) and it is fully attached to the nozzle. While the vortex ring being attached for the entire ejection phase, the vortex ring keeps growing in size and in strength with the entrainment from the surrounding fluid. Consequently, the vortex ring reaches the target surface towards the end of the ejection phase (φ =135º) and starts spreading radially (φ =180º). At the early inhale phase (φ =225º), the vortex ring at the nozzle exit gets detached from the nozzle, so does the vortex ring in the near-wall region. No strong vortex formation is observed for the rest of the ejection phase until the small vortex ring is generated at the nozzle exit at the beginning of the exhale phase. This pattern repeats itself for the total time interval considered in this study.

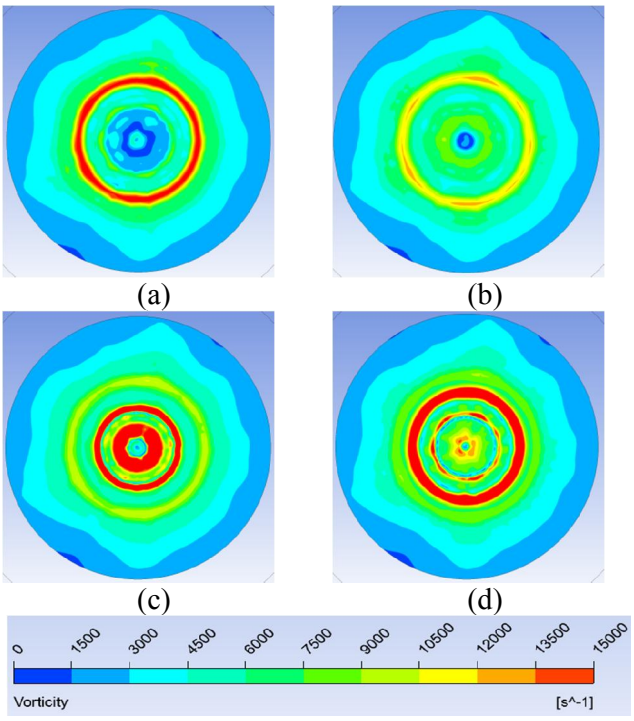

Figure 43: Instantaneous vorticity distributions over the target plate at (a) φ =0º, (b) φ =90º, (c) φ =180º, (d) φ =270º.

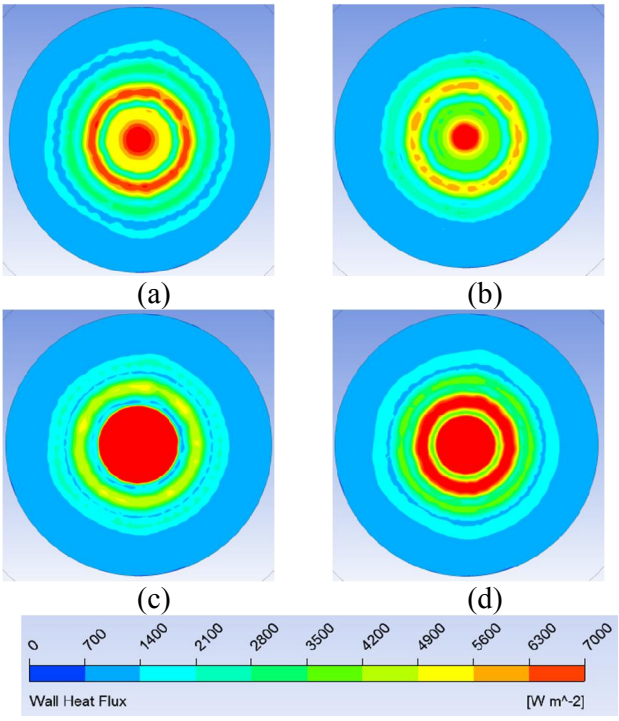

Figure 44: Instantaneous heat flux distributions on the target plate at (a) φ =0º, (b) φ =90º, (c) φ =180º, (d) φ =270º.

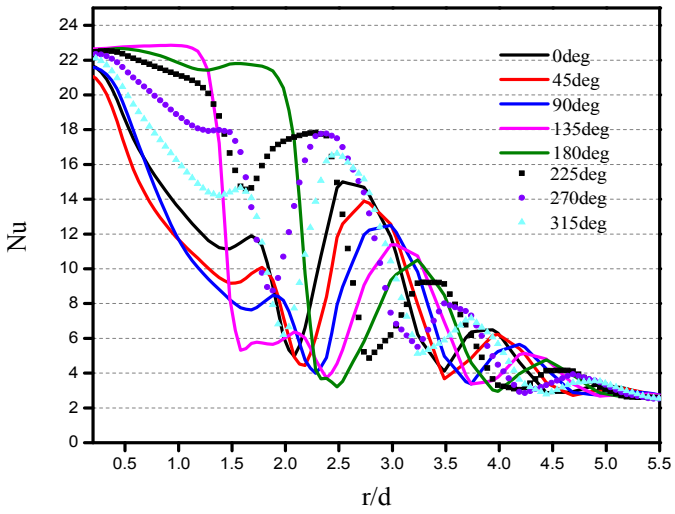

Figure 45: Nu number distribution on the target plate at various phase angles (times), ReD_j = 1400 and y/d = 2.

These near-wall vortices have considerable effects on the surface profiles. This is evident from Figure 43 and Figure 44 which show the vorticity and heat flux contours on the target surface, respectively, at various phase angles. As can be seen from Figure 43, at $\varphi = 180^{o}$, the detached vortex ring is located at nearly $r/d \approx 3$ which is almost coincident with the first off- center peak in the vorticity profile of Figure 43, and that of the heat flux distribution shown in Figure 44. There are multiple rings shown in both of these distributions, spreading in the radial direction with peaks and valleys.

Figure 45 shows Nu distributions in the radial direction at various phase angles. As can be seen, a significant increase in the heat transfer coefficient is observed in the stagnation area at $\varphi = 135^{o}$. It is worth noting that this is coincident with the time where the vortex ring produced at the nozzle exit reaches the target surface. Thereafter, while there is a slight variation in stagnation point heat transfer coefficient, heat transfer coefficient decreases with the phase angle in the vicinity of $0.5 \leq r/d \leq 2.0$. As it is expected and consistent with the vorticity and heat flux contours shown in Figure 43 and Figure 44, the distributions of heat transfer coefficient at different phase angles demonstrate multiple off-center peaks as well (see Figure 45).

Figures 40, 41, 46 and 47 show that the pressure and heat transfer distributions at the target wall are highly non-monotonic and demonstrate multiple off-center peaks at $y/d = 2$. For the same frequency and the jet velocity, if the nozzle-to-plate distance is increased to $Y/D = 5$, these fluctuations are not completely vanished but attenuated significantly. Further increases in nozzle-to-plate distance lead to monotonic profiles, i.e. the off-center peaks completely vanish. Based on the following definition of Strouhal number with height adjustment:

$$St=\frac{fD}{\bar{u}_j}\left[\frac{y}{d}\right]^{-1} \quad (38)$$

It is clear from the equation (38) that when H will increase to very large number St Number will reduces to very small, and when St > 0.02, non-monotonic wall profiles may be expected from a circular synthetic jet.

5.6. Power consumption

Any new proposed cooling technology should consume minimum amount of energy with high cooling performance leading to a high coefficient of performance (COP). The definition of COP for current study is used as heat removal from heater front surface over power supplied to the actuator [71]. Power consumption for circular orifice jets are measured and showed in Figure 46. Power consumption is not mentioned here, since ART4500 and ART3500 was analyzed at very early stage and their piezoelectric element flake out from the diaphragm and later is not able to measure its power at 20 Vpp in order to make comparison with annular orifice jets.

Figure 46 shows the power consumption for ART4000, ART2000, and the high frequency synthetic jet. Power consumption for all three jets for three different voltages is presented. For low frequency jets, peak to peak voltages were 15, 20 and 25 volts, but for the high frequency jet 25 Vpp operating condition would be harsh which was why the high frequency jet was operated at 10, 15 and 20 Vpp for its power consumption.

It is seen that comparison between three is only made at 15 and 20 Vpp. It is observed that ART4000 consumed 0.08 watt at 15 Vpp and 0.13 watt at 20 Vpp. For ART2000 these values are 0.06 and 0.1 for 15 watt and 20 Vpp, respectively and high frequency jet showed values around 0.27 and 0.33 watt for 15 and 20 Vpp. COP for ART4000 and

ART2000 showed slightly different while in power ART2000 consumed the least amount of power. High frequency jet drew the amount of maximum power and also has shown the maximum coefficient of performance.

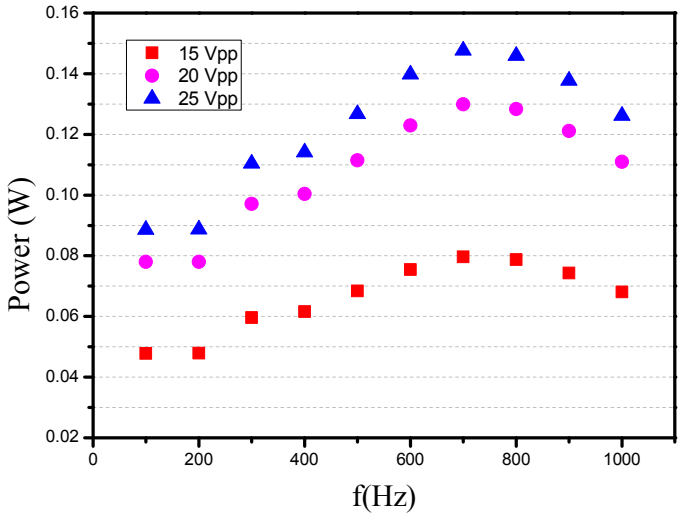

(a)

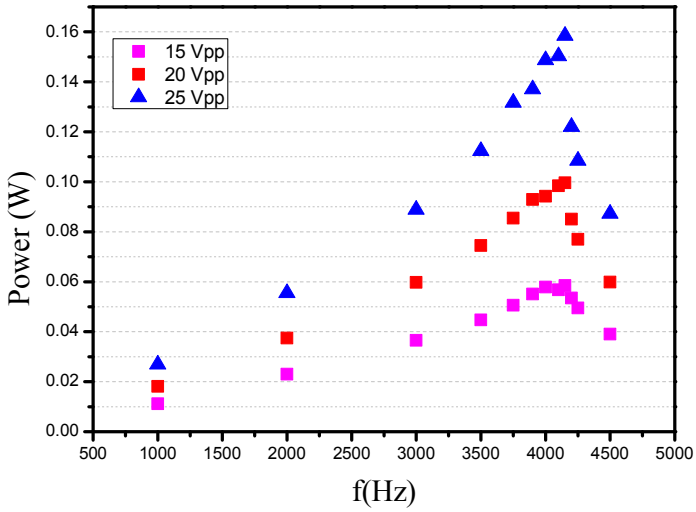

(b)

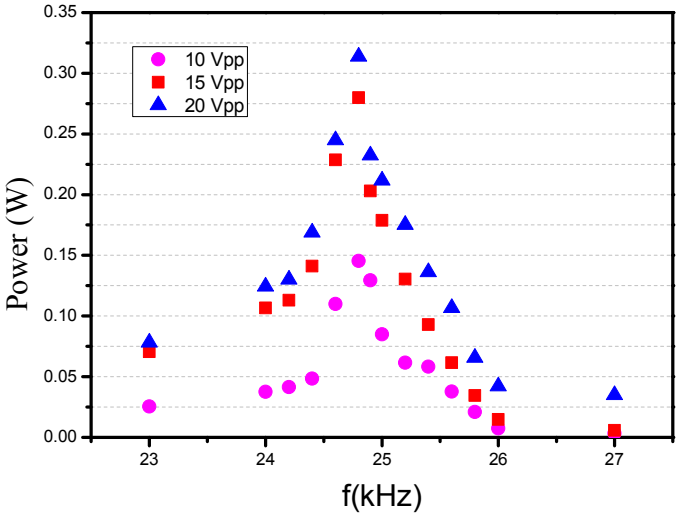

(c)

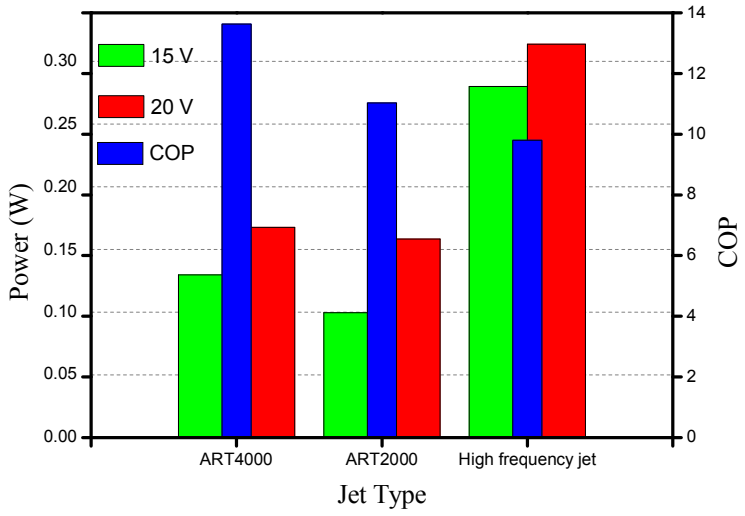

(d)

Figure 46: (a) ART4000 power consumption (b) ART2000 power consumption (c) High frequency jet power consumption (d) Power consumption comparison and COP

Figure 46 (d) shows the comparison between power consumption and COP of all three different types of synthetic jets at 15 and 20 Vpp. COP was calculated at Z/d=10. The high frequency jet drew the maximum power because it is operated at the third mode shape. The main disadvantages of operating the jet at any mode shape except for the first mode are high power consumption and less amount of deflection. The least deflection can be encountered by high frequency but high power consumption may be an issue for electronics cooling applications.

CHAPTER V

6. SUMMARY AND CONCLUSIONS

6.1. Experimental study

An experimental and computational study for predicting the cooling performance of central orifice synthetic jets impinging over a vertical surface was conducted for a range of voltages and frequencies. The effects of jet driving frequency and axial distance to heated surface on heat transfer were also investigated. The following key observations have been made from current study

- The cooling performance of synthetic jets peaks at their resonance frequency for low frequency jets and for the high frequency jet operating at structural and cavity Helmholtz resonance simultaneously.
- The effect of axial distance on the heat transfer gets more profound as the jet driving frequencies increase.
- The effect of synthetic jet actuator size was examined, and it was found that as the size decreases the operating frequency increases which has a primary role in building high frequency synthetic jet actuators.
- High frequency jet consumes more power than others because it operates at the third mode shape. The power consumption also depends on the size, shown by power consumption of ART4000 and ART2000.
- A comparison of various jets for power consumption comparison was made and COP for 40 mm jet (for central orifice jets) has the highest value while the high frequency jet has the lowest values.
- A 45 mm jet showed maximum Nu number (almost 15 at Z/d=10) and 20 mm jet

showed the weakest heat transfer capability.

- It has been observed that a high frequency jet and ART4500 has the highest heat transfer coefficient (almost 13 times of natural convection) and 20 mm jet has the lowest as heat transfer coefficient (9 times of natural convection).
- A set of heat transfer correlations were proposed for low frequency and high frequency synthetic jets with a central orifice. These correlations were based on the experimental results, and can be used to predict the heat transfer as a function of Re number, axial distance, area of heater to area of orifice and jet driving frequency.
- The correlations were presented to foretell average Nu number within ± 25%. This correlation has been developed for Re numbers less than 1200, while Z/d from 5 to 50 and normalize frequency form 0.15 to 1 for low frequency jet.
- In order to build high frequency synthetic jet it is almost impractical to operate jet at first resonance frequency. Third mode resonance is an ideal mode shape to operate high frequency jet. Operating jet third mode has two benefits, bigger size and thinner diaphragm can be used. Thin diaphragm will allow the considerable amount of deflection that can excite the air that can remove the heat.

6.2. CFD study for circular jet

A meso-scale round synthetic jet actuated with a sine-wave is studied computationally. Momentum and temperature fields are investigated at ReD_j = 1400, y/d = 2 and f = 500 Hz. Surface pressure, heat transfer coefficient, and near-wall profiles are determined and comparisons are made with impinging jet counterparts where possible. Based on the computed results, the following conclusions are drawn:

- Pressure coefficients at the stagnation point are positive for all phase angles.

Maximum pressure coefficient is obtained in the second half of the ejection phase ($\varphi = 135^{o}$). Time averaged pressure profile is of Gaussian shape and very similar to that of an impinging jet at comparable Re numbers.

- Instantaneously, pressure gradients cease at r/d = 4 for all phase angles. The maximum radial velocity obtained at this radial coordinate is at the same phase angle where maximum pressure coefficient is obtained ($\varphi = 135^{o}$).
- A small vortex ring is produced at the nozzle exit in the beginning of the ejection phase and while being attached for the entire ejection phase, it continues to grow in size and strength with the surrounding fluid entrained into the jet. It reaches the target plate in late ejection phase ($\varphi = 135^{o}$), expands radially at the beginning of the inhale phase ($\varphi = 180^{o}$) and detachment of near nozzle and near wall vortices occurs in the early inhale phase ($\varphi = 225^{o}$).
- Instantaneous wall profiles produced by this round synthetic jet are highly non-monotonic for St > 0.02. $\varphi = 135^{o}$ seems to produce the highest stagnation pressure, stagnation heat transfer coefficient, average heat transfer coefficient on the target wall and radial velocities near the wall. This phase angle is coincident with the time the vortex ring generated at the nozzle exit reaches the target plate.

6.3. Future research

In order to build high frequency synthetic jet there are two parts that should be design and make them compatible with each other, diaphragm and cavity. Following can be future research work on synthetic jet in order build high frequency one.

- Acoustic analysis for the cavity is order to build cavity having Helmholtz resonance more than 20 kHz.
- Design of piezoelectric actuator that can operate more than 20 kHz at it third

resonance.

- Mode shape measuring using scanning laser vibrometer for central orifice jet (fixed complete periphery) and slot jet (fixed partially from its periphery).
- In current study CFD study has done only for semi confined synthetic jet, fully confined and unconfined synthetic jet in order to have in-depth knowledge of flow physics and heat transfer mechanism.
- Heat sink embedded with synthetic jet should be examined for specific applications like LED street lamps and indoor lightings.

Appendix A
UNCERTAINTY ANALYSIS

V= 9.541	"Voltage"
I=0.123	"Current"
P=V*I	"power"
D=2*convert(mm,m)	"orifice diameter"
K=0.0257	"Air conductivity"
T_amb=24.757	"Ambient Temp"
T_1=59.875	"Heater Temp1"
T_2=59.884	"Heater Temp2"
T_3=60.028	"Heater Temp3"
T_4=60.292	"Heater Temp4"
T_avg=(T_1+T_2+T_3+T_4)/4	"Average Temp"
T_diff=T_avg-T_amb	"Temp Differenc"
H_loss=0.024*T_diff-0.0056	"Heat Loss"
H_front=P-H_loss	"Front Heat"
L_heater=25.4	"Length of heater"
W_heater=25.4	"Width of heater"
A=L_heater*W_heater*convert(mm^2,m^2)	"Heater Area"
h=H_front/(A*T_diff)	"Heat transfer Coefficient"
Nu=h*D/K	"Nusselt Number"

V	I	P	T_1	T_2	T_3	T_4	T_{amb}	T_{avg}	T_{diff}	Q_{loss}	Q_{heater}	H	Nu
9.541±0.01	0.123±0.001	1.174±0.00962	59.88±0.1	59.88±0.1	60.03±0.1	60.29±0.1	24.76	60.02±0.05	35.26±0.05	0.8407±0.0012	0.3328±0.009695	14.63±0.4292	1.139±0.0334
9.963±0.01	0.129±0.001	1.285±0.01005	59.9±0.1	59.89±0.1	60.03±0.1	60.26±0.1	24.75	60.02±0.05	35.27±0.05	0.8408±0.0012	0.4444±0.01012	19.53±0.4488	1.52±0.03493
10.58±0.01	0.137±0.001	1.449±0.01067	59.93±0.1	59.86±0.1	60.06±0.1	60.19±0.1	24.75	60.01±0.05	35.26±0.05	0.8406±0.0012	0.6089±0.01074	26.77±0.4777	2.083±0.03717
12.42±0.01	0.16±0.001	1.988±0.01253	59.95±0.1	59.85±0.1	60.1±0.1	60.14±0.1	24.76	60.01±0.05	35.25±0.05	0.8404±0.0012	1.147±0.01258	50.46±0.5647	3.927±0.04395
14.3±0.01	0.184±0.001	2.632±0.01442	59.97±0.1	59.84±0.1	60.16±0.1	60.04±0.1	24.87	60.01±0.05	35.14±0.05	0.8377±0.0012	1.794±0.01447	79.15±0.6574	6.16±0.05116
13.23±0.01	0.171±0.001	2.263±0.01334	59.94±0.1	59.81±0.1	60.09±0.1	60.02±0.1	24.85	59.97±0.05	35.11±0.05	0.8371±0.0012	1.426±0.0134	62.94±0.6061	4.898±0.04716
11.82±0.01	0.152±0.001	1.797±0.01192	59.96±0.1	59.87±0.1	60.07±0.1	60.08±0.1	24.82	59.99±0.05	35.17±0.05	0.8385±0.0012	0.9581±0.01198	42.23±0.5372	3.286±0.04181

10.83±0.01	0.14±0.001	1.516±0.01092	59.94±0.1	59.88±0.1	60.03±0.1	60.1±0.1	24.8	59.99±0.05	35.18±0.05	0.8388±0.0012	0.6771±0.01098	29.83±0.4903	2.321±0.03816
10.08±0.01	0.13±0.001	1.31±0.01016	59.94±0.1	59.88±0.1	60.01±0.1	60.12±0.1	24.79	59.99±0.05	35.2±0.05	0.8393±0.0012	0.4711±0.01023	20.74±0.455	1.614±0.03541
9.257±0.01	0.119±0.001	1.102±0.009333	59.96±0.1	59.89±0.1	59.98±0.1	60.14±0.1	24.78	59.99±0.05	35.21±0.05	0.8395±0.0012	0.2621±0.00941	11.54±0.4166	0.8977±0.03242
9.402±0.01	0.121±0.001	1.138±0.00948	59.97±0.1	59.9±0.1	59.99±0.1	60.16±0.1	24.78	60.01±0.05	35.23±0.05	0.8398±0.0012	0.2978±0.009555	13.11±0.4232	1.02±0.03293
9.163±0.01	0.118±0.001	1.081±0.009239	59.98±0.1	59.9±0.1	60±0.1	60.15±0.1	24.79	60±0.05	35.22±0.05	0.8396±0.0012	0.2416±0.009316	10.63±0.4122	0.8274±0.03208
9.196±0.01	0.119±0.001	1.094±0.009273	59.97±0.1	59.89±0.1	59.99±0.1	60.15±0.1	24.79	60±0.05	35.21±0.05	0.8394±0.0012	0.2549±0.00935	11.22±0.414	0.8734±0.03222
9.803±0.01	0.126±0.001	1.235±0.009884	59.98±0.1	59.91±0.1	60.02±0.1	60.16±0.1	24.8	60.02±0.05	35.22±0.05	0.8396±0.0012	0.3956±0.009956	17.41±0.4419	1.355±0.03439
10.58±0.01	0.136±0.001	1.439±0.01067	59.99±0.1	59.91±0.1	60.03±0.1	60.11±0.1	24.89	60.01±0.05	35.12±0.05	0.8373±0.0012	0.602±0.01074	26.57±0.4796	2.068±0.03732
12.46±0.01	0.161±0.001	2.007±0.01257	59.98±0.1	59.88±0.1	60.09±0.1	60.06±0.1	24.95	60±0.05	35.05±0.05	0.8357±0.0012	1.171±0.01262	51.78±0.57	4.03±0.04436
14.63±0.01	0.188±0.001	2.751±0.01475	60.01±0.1	59.85±0.1	60.2±0.1	60.01±0.1	25.07	60.02±0.05	34.95±0.05	0.8333±0.0012	1.918±0.0148	85.03±0.6772	6.617±0.0527
14.36±0.01	0.185±0.001	2.657±0.01448	59.95±0.1	59.81±0.1	60.14±0.1	60.02±0.1	24.99	59.98±0.05	34.99±0.05	0.8341±0.0012	1.823±0.01453	80.75±0.6633	6.284±0.05162
12.08±0.01	0.156±0.001	1.885±0.01218	59.96±0.1	59.88±0.1	60.08±0.1	60.1±0.1	24.98	60.01±0.05	35.03±0.05	0.8351±0.0012	1.05±0.01224	46.46±0.5522	3.616±0.04297
10.91±0.01	0.141±0.001	1.539±0.011	59.94±0.1	59.88±0.1	60.04±0.1	60.12±0.1	24.97	59.99±0.05	35.03±0.05	0.8351±0.0012	0.7038±0.01107	31.14±0.4966	2.424±0.03865
10.03±0.01	0.129±0.001	1.293±0.01011	59.94±0.1	59.88±0.1	60±0.1	60.14±0.1	24.93	59.99±0.05	35.06±0.05	0.8359±0.0012	0.4573±0.01018	20.22±0.4543	1.573±0.03535
9.318±0.01	0.12±0.001	1.118±0.009395	59.94±0.1	59.87±0.1	59.97±0.1	60.14±0.1	24.92	59.98±0.05	35.06±0.05	0.8359±0.0012	0.2823±0.009471	12.48±0.4213	0.9711±0.03279
9.517±0.01	0.123±0.001	1.171±0.009596	59.96±0.1	59.88±0.1	59.97±0.1	60.14±0.1	24.93	59.99±0.05	35.05±0.05	0.8357±0.0012	0.3349±0.009671	14.81±0.4308	1.152±0.03352
9.116±0.01	0.118±0.001	1.076±0.009192	59.98±0.1	59.91±0.1	59.99±0.1	60.14±0.1	24.97	60.01±0.05	35.04±0.05	0.8353±0.0012	0.2404±0.00927	10.63±0.4123	0.8274±0.03209
9.164±0.01	0.118±0.001	1.081±0.00924	59.98±0.1	59.91±0.1	59.99±0.1	60.14±0.1	24.97	60±0.05	35.03±0.05	0.8351±0.0012	0.2463±0.009317	10.9±0.4146	0.8481±0.03226
9.477±0.01	0.122±0.001	1.156±0.009555	60±0.1	59.93±0.1	60.02±0.1	60.14±0.1	24.99	60.02±0.05	35.03±0.05	0.8351±0.0012	0.3211±0.00963	14.21±0.4291	1.106±0.0334
10.53±0.01	0.136±0.001	1.432±0.01061	60±0.1	59.91±0.1	60.04±0.1	60.12±0.1	25.01	60.02±0.05	35.01±0.05	0.8346±0.0012	0.5971±0.01068	26.44±0.4787	2.058±0.03725
12.62±0.01	0.163±0.001	2.058±0.01273	59.99±0.1	59.89±0.1	60.1±0.1	60.07±0.1	25.07	60.01±0.05	34.94±0.05	0.833±0.0012	1.225±0.01279	54.33±0.5797	4.228±0.04511
14.58±0.01	0.188±0.001	2.74±0.0147	59.98±0.1	59.84±0.1	60.2±0.1	60.07±0.1	25.15	60.02±0.05	34.87±0.05	0.8313±0.0012	1.909±0.01475	84.85±0.6763	6.603±0.05263
14.31±0.01	0.184±0.001	2.633±0.01443	59.96±0.1	59.82±0.1	60.16±0.1	60.04±0.1	25.14	60±0.05	34.86±0.05	0.8311±0.0012	1.802±0.01448	80.12±0.6632	6.235±0.05161
11.94±0.01	0.154±0.001	1.838±0.01203	59.94±0.1	59.87±0.1	60.07±0.1	60.09±0.1	25.06	59.99±0.05	34.93±0.05	0.8328±0.0012	1.005±0.01209	44.61±0.5467	3.472±0.04254
11.1±0.01	0.143±0.001	1.587±0.01119	59.94±0.1	59.87±0.1	60.02±0.1	60.12±0.1	25.04	59.99±0.05	34.95±0.05	0.8331±0.0012	0.7535±0.01125	33.42±0.5064	2.601±0.0394
10.13±0.01	0.131±0.001	1.327±0.01021	59.95±0.1	59.89±0.1	59.99±0.1	60.09±0.1	25.11	59.98±0.05	34.87±0.05	0.8313±0.0012	0.4955±0.01028	22.02±0.4618	1.714±0.03594
9.198±0.01	0.119±0.001	1.095±0.009275	59.97±0.1	59.88±0.1	59.96±0.1	60.11±0.1	25.1	59.98±0.05	34.88±0.05	0.8316±0.0012	0.263±0.009352	11.69±0.418	0.9095±0.03253

9.342±0.01	0.12±0.001	1.121±0.009419	59.99±0.1	59.9±0.1	59.98±0.1	60.13±0.1	25.1	60±0.05	34.9±0.05	0.8321±0.0012	0.289±0.009495	12.83±0.4244	0.9987±0.03303
9.293±0.01	0.12±0.001	1.115±0.00937	59.99±0.1	59.91±0.1	59.99±0.1	60.13±0.1	25.1	60±0.05	34.91±0.05	0.8322±0.0012	0.283±0.009447	12.56±0.4221	0.9777±0.03285
9.358±0.01	0.121±0.001	1.132±0.009436	59.99±0.1	59.9±0.1	59.98±0.1	60.13±0.1	25.1	60±0.05	34.9±0.05	0.8321±0.0012	0.3003±0.009512	13.33±0.4253	1.038±0.03309
9.99±0.01	0.129±0.001	1.289±0.01007	60.03±0.1	59.95±0.1	60.05±0.1	60.17±0.1	25.12	60.05±0.05	34.93±0.05	0.8328±0.0012	0.4559±0.01014	20.23±0.4545	1.574±0.03537
12±0.01	0.155±0.001	1.86±0.0121	59.94±0.1	59.86±0.1	60.07±0.1	60.11±0.1	25.14	60±0.05	34.86±0.05	0.8309±0.0012	1.029±0.01216	45.75±0.551	3.56±0.04288
14.12±0.01	0.182±0.001	2.57±0.01424	59.98±0.1	59.85±0.1	60.15±0.1	60.02±0.1	25.27	60±0.05	34.73±0.05	0.8279±0.0012	1.743±0.01429	77.77±0.6568	6.052±0.05111
15.46±0.01	0.199±0.001	3.076±0.01559	60±0.1	59.86±0.1	60.25±0.1	60±0.1	25.36	60.03±0.05	34.67±0.05	0.8265±0.0012	2.25±0.01563	100.6±0.7245	7.827±0.05638
15.32±0.01	0.197±0.001	3.018±0.01545	60±0.1	59.85±0.1	60.22±0.1	59.99±0.1	25.31	60.01±0.05	34.7±0.05	0.8272±0.0012	2.191±0.01549	97.86±0.7168	7.615±0.05579
14.71±0.01	0.189±0.001	2.78±0.01483	59.98±0.1	59.82±0.1	60.14±0.1	59.98±0.1	25.32	59.98±0.05	34.66±0.05	0.8262±0.0012	1.954±0.01488	87.37±0.6871	6.799±0.05347
13.55±0.01	0.174±0.001	2.357±0.01366	59.96±0.1	59.84±0.1	60.11±0.1	60.02±0.1	25.28	59.98±0.05	34.7±0.05	0.8272±0.0012	1.53±0.01371	68.35±0.6288	5.319±0.04894
12.85±0.01	0.165±0.001	2.12±0.01295	59.97±0.1	59.85±0.1	60.09±0.1	60.06±0.1	25.25	59.99±0.05	34.74±0.05	0.8281±0.0012	1.291±0.01301	57.62±0.5938	4.484±0.04621
9.132±0.01	0.118±0.001	1.078±0.009208	59.98±0.1	59.91±0.1	60±0.1	60.18±0.1	25.16	60.01±0.05	34.85±0.05	0.8309±0.0012	0.2467±0.009286	10.97±0.4153	0.8537±0.03232
9.274±0.01	0.12±0.001	1.113±0.009351	59.98±0.1	59.91±0.1	60.01±0.1	60.19±0.1	25.16	60.02±0.05	34.86±0.05	0.8311±0.0012	0.2818±0.009428	12.53±0.4218	0.9748±0.03283
9.22±0.01	0.119±0.001	1.097±0.009296	59.97±0.1	59.9±0.1	59.99±0.1	60.17±0.1	25.16	60.01±0.05	34.85±0.05	0.8307±0.0012	0.2665±0.009374	11.85±0.4195	0.9224±0.03264
9.097±0.01	0.117±0.001	1.064±0.009172	59.96±0.1	59.88±0.1	59.98±0.1	60.16±0.1	25.16	60±0.05	34.84±0.05	0.8305±0.0012	0.2338±0.00925	10.4±0.4138	0.8097±0.0322
10.01±0.01	0.129±0.001	1.291±0.01009	59.97±0.1	59.9±0.1	60±0.1	60.12±0.1	25.24	60±0.05	34.76±0.05	0.8286±0.0012	0.4625±0.01016	20.62±0.4576	1.605±0.03561
12.21±0.01	0.157±0.001	1.918±0.01231	59.98±0.1	59.89±0.1	60.08±0.1	60.08±0.1	25.29	60.01±0.05	34.72±0.05	0.8277±0.0012	1.09±0.01237	48.65±0.5634	3.786±0.04385
14.17±0.01	0.182±0.001	2.579±0.01428	59.98±0.1	59.86±0.1	60.16±0.1	60.03±0.1	25.35	60.01±0.05	34.65±0.05	0.8261±0.0012	1.753±0.01433	78.39±0.6604	6.1±0.05139
15.47±0.01	0.199±0.001	3.078±0.0156	59.98±0.1	59.83±0.1	60.22±0.1	59.97±0.1	25.4	60±0.05	34.6±0.05	0.8249±0.0012	2.253±0.01564	100.9±0.7265	7.855±0.05654
15.14±0.01	0.195±0.001	2.952±0.01526	59.98±0.1	59.84±0.1	60.22±0.1	59.99±0.1	25.4	60.01±0.05	34.61±0.05	0.825±0.0012	2.127±0.01531	95.25±0.7099	7.413±0.05524
14.42±0.01	0.186±0.001	2.682±0.01454	59.95±0.1	59.82±0.1	60.15±0.1	60.02±0.1	25.35	59.99±0.05	34.63±0.05	0.8256±0.0012	1.856±0.01459	83.07±0.6734	6.465±0.0524
13.66±0.01	0.176±0.001	2.403±0.01377	59.92±0.1	59.8±0.1	60.09±0.1	60.03±0.1	25.33	59.96±0.05	34.63±0.05	0.8255±0.0012	1.578±0.01382	70.64±0.6357	5.497±0.04947
12.78±0.01	0.165±0.001	2.109±0.01289	59.94±0.1	59.84±0.1	60.08±0.1	60.07±0.1	25.32	59.98±0.05	34.66±0.05	0.8263±0.0012	1.282±0.01294	57.35±0.5921	4.463±0.04608
9.256±0.01	0.119±0.001	1.101±0.009332	59.97±0.1	59.91±0.1	60±0.1	60.18±0.1	25.25	60.01±0.05	34.77±0.05	0.8288±0.0012	0.2727±0.009409	12.16±0.4221	0.946±0.03285
9.11±0.01	0.117±0.001	1.066±0.009185	60±0.1	59.93±0.1	60.01±0.1	60.19±0.1	25.25	60.03±0.05	34.78±0.05	0.829±0.0012	0.2368±0.009263	10.56±0.4151	0.8215±0.0323
9.874±0.01	0.127±0.001	1.254±0.009955	59.98±0.1	59.91±0.1	60.01±0.1	60.13±0.1	25.33	60±0.05	34.68±0.05	0.8267±0.0012	0.4273±0.01003	19.1±0.4523	1.486±0.0352
12.03±0.01	0.155±0.001	1.865±0.01213	59.96±0.1	59.87±0.1	60.07±0.1	60.07±0.1	25.38	59.99±0.05	34.61±0.05	0.825±0.0012	1.04±0.01219	46.58±0.5566	3.625±0.04332

14.12±0.01	0.182±0.001	2.569±0.01423	59.96±0.1	59.85±0.1	60.14±0.1	60.02±0.1	25.44	59.99±0.05	34.55±0.05	0.8237±0.0012	1.746±0.01428	78.3±0.66	6.094±0.05136
15.5±0.01	0.199±0.001	3.085±0.01563	59.99±0.1	59.85±0.1	60.23±0.1	59.98±0.1	25.49	60.01±0.05	34.52±0.05	0.8229±0.0012	2.262±0.01567	101.5±0.7298	7.902±0.0568
15.24±0.01	0.196±0.001	2.986±0.01536	59.99±0.1	59.84±0.1	60.22±0.1	59.97±0.1	25.51	60±0.05	34.5±0.05	0.8223±0.0012	2.164±0.01541	97.23±0.7172	7.566±0.05581
14.64±0.01	0.188±0.001	2.753±0.01476	59.97±0.1	59.82±0.1	60.15±0.1	60.01±0.1	25.44	59.99±0.05	34.55±0.05	0.8236±0.0012	1.929±0.01481	86.56±0.6861	6.736±0.0534
13.67±0.01	0.176±0.001	2.406±0.01378	59.93±0.1	59.81±0.1	60.1±0.1	60.02±0.1	25.39	59.96±0.05	34.57±0.05	0.8242±0.0012	1.582±0.01384	70.92±0.6374	5.519±0.04961
12.64±0.01	0.163±0.001	2.06±0.01274	59.95±0.1	59.84±0.1	60.08±0.1	60.07±0.1	25.38	59.98±0.05	34.61±0.05	0.825±0.0012	1.235±0.0128	55.29±0.586	4.303±0.04561
9.405±0.01	0.121±0.001	1.138±0.009483	59.99±0.1	59.92±0.1	60.01±0.1	60.18±0.1	25.31	60.02±0.05	34.71±0.05	0.8274±0.0012	0.3106±0.009558	13.87±0.4298	1.079±0.03345
8.962±0.01	0.116±0.001	1.04±0.009037	60±0.1	59.92±0.1	60.01±0.1	60.19±0.1	25.32	60.03±0.05	34.71±0.05	0.8275±0.0012	0.2121±0.009116	9.473±0.4091	0.7372±0.03184
8.997±0.01	0.116±0.001	1.044±0.009071	59.98±0.1	59.91±0.1	60±0.1	60.17±0.1	25.31	60.01±0.05	34.7±0.05	0.8272±0.0012	0.2165±0.00915	9.67±0.4108	0.7525±0.03197
9.041±0.01	0.117±0.001	1.058±0.009116	59.97±0.1	59.9±0.1	59.98±0.1	60.15±0.1	25.32	60±0.05	34.68±0.05	0.8266±0.0012	0.2312±0.009195	10.33±0.4132	0.8041±0.03216
11.87±0.01	0.153±0.001	1.816±0.01197	80.04±0.1	79.91±0.1	80.05±0.1	80.08±0.1	25.4	80.02±0.05	54.62±0.05	1.305±0.0012	0.5103±0.01203	14.48±0.3428	1.127±0.02668
12.66±0.01	0.163±0.001	2.064±0.01276	80.04±0.1	79.93±0.1	80.1±0.1	80.11±0.1	25.41	80.04±0.05	54.64±0.05	1.306±0.0012	0.7579±0.01282	21.5±0.3661	1.673±0.02849
13.48±0.01	0.173±0.001	2.332±0.01359	80±0.1	79.86±0.1	80.13±0.1	80.08±0.1	25.38	80.02±0.05	54.63±0.05	1.306±0.0012	1.026±0.01364	29.11±0.3902	2.265±0.03037
15.59±0.01	0.2±0.001	3.117±0.01571	79.99±0.1	79.82±0.1	80.21±0.1	79.99±0.1	25.48	80±0.05	54.52±0.05	1.303±0.0012	1.815±0.01576	51.59±0.4541	4.014±0.03534
17.89±0.01	0.229±0.001	4.096±0.01803	80.01±0.1	79.79±0.1	80.36±0.1	79.94±0.1	25.53	80.02±0.05	54.49±0.05	1.302±0.0012	2.794±0.01807	79.47±0.524	6.184±0.04078
16.65±0.01	0.214±0.001	3.563±0.01678	79.99±0.1	79.79±0.1	80.26±0.1	79.92±0.1	25.52	79.99±0.05	54.47±0.05	1.302±0.0012	2.261±0.01683	64.34±0.4867	5.007±0.03787
14.61±0.01	0.188±0.001	2.746±0.01473	79.99±0.1	79.83±0.1	80.15±0.1	79.96±0.1	25.45	79.98±0.05	54.53±0.05	1.303±0.0012	1.443±0.01478	41.01±0.4247	3.192±0.03305
13.7±0.01	0.176±0.001	2.412±0.01382	79.96±0.1	79.86±0.1	80.1±0.1	80.01±0.1	25.44	79.98±0.05	54.54±0.05	1.303±0.0012	1.108±0.01387	31.5±0.3977	2.452±0.03095
12.85±0.01	0.165±0.001	2.12±0.01295	79.96±0.1	79.86±0.1	80.06±0.1	80.05±0.1	25.45	79.98±0.05	54.53±0.05	1.303±0.0012	0.8164±0.01301	23.2±0.3723	1.806±0.02897
11.86±0.01	0.153±0.001	1.815±0.01196	79.98±0.1	79.87±0.1	80.02±0.1	80.09±0.1	25.4	79.99±0.05	54.6±0.05	1.305±0.0012	0.51±0.01202	14.48±0.3428	1.127±0.02668
11.69±0.01	0.15±0.001	1.754±0.01179	80±0.1	79.89±0.1	80.04±0.1	80.12±0.1	25.39	80.01±0.05	54.62±0.05	1.305±0.0012	0.4486±0.01185	12.73±0.3376	0.9906±0.02627
11.85±0.01	0.152±0.001	1.801±0.01195	80±0.1	79.88±0.1	80.04±0.1	80.11±0.1	25.38	80.01±0.05	54.63±0.05	1.306±0.0012	0.4956±0.01201	14.06±0.3422	1.094±0.02663
11.92±0.01	0.153±0.001	1.824±0.01202	79.98±0.1	79.87±0.1	80.03±0.1	80.1±0.1	25.39	80±0.05	54.61±0.05	1.305±0.0012	0.5194±0.01208	14.74±0.3445	1.147±0.02681
12.34±0.01	0.159±0.001	1.963±0.01244	80±0.1	79.89±0.1	80.07±0.1	80.13±0.1	25.39	80.02±0.05	54.63±0.05	1.305±0.0012	0.657±0.0125	18.64±0.3568	1.451±0.02777
13.39±0.01	0.172±0.001	2.302±0.0135	80±0.1	79.88±0.1	80.11±0.1	80.11±0.1	25.44	80.02±0.05	54.59±0.05	1.304±0.0012	0.998±0.01355	28.34±0.3879	2.205±0.03019
16.39±0.01	0.21±0.001	3.441±0.01652	79.94±0.1	79.8±0.1	80.19±0.1	79.98±0.1	25.53	79.98±0.05	54.44±0.05	1.301±0.0012	2.14±0.01656	60.92±0.4788	4.741±0.03726
18.63±0.01	0.239±0.001	4.452±0.01878	79.96±0.1	79.76±0.1	80.37±0.1	79.9±0.1	25.67	80±0.05	54.33±0.05	1.298±0.0012	3.154±0.01882	89.98±0.5485	7.002±0.04268

17.79±0.01	0.228±0.001	4.056±0.01794	79.95±0.1	79.75±0.1	80.31±0.1	79.91±0.1	25.65	79.98±0.05	54.33±0.05	1.298±0.0012	2.758±0.01798	78.68±0.5227	6.123±0.04068
15.36±0.01	0.197±0.001	3.025±0.01548	79.97±0.1	79.83±0.1	80.17±0.1	79.98±0.1	25.6	79.99±0.05	54.39±0.05	1.3±0.0012	1.725±0.01553	49.17±0.4483	3.826±0.03488
13.95±0.01	0.179±0.001	2.497±0.01407	79.96±0.1	79.87±0.1	80.11±0.1	80.03±0.1	25.57	79.99±0.05	54.43±0.05	1.301±0.0012	1.197±0.01412	34.08±0.4059	2.652±0.03159
12.87±0.01	0.165±0.001	2.123±0.01297	79.97±0.1	79.88±0.1	80.06±0.1	80.06±0.1	25.51	79.99±0.05	54.48±0.05	1.302±0.0012	0.8214±0.01303	23.37±0.3733	1.819±0.02905
11.81±0.01	0.152±0.001	1.795±0.01191	80.01±0.1	79.89±0.1	80.04±0.1	80.08±0.1	25.56	80±0.05	54.45±0.05	1.301±0.0012	0.4943±0.01197	14.07±0.3423	1.095±0.02664
11.99±0.01	0.154±0.001	1.846±0.01209	80.01±0.1	79.89±0.1	80.03±0.1	80.08±0.1	25.56	80±0.05	54.44±0.05	1.301±0.0012	0.5455±0.01215	15.53±0.3476	1.209±0.02705
11.74±0.01	0.151±0.001	1.773±0.01184	80.01±0.1	79.89±0.1	80.03±0.1	80.08±0.1	25.57	80±0.05	54.43±0.05	1.301±0.0012	0.4723±0.0119	13.45±0.3403	1.047±0.02648
11.68±0.01	0.15±0.001	1.753±0.01178	80±0.1	79.89±0.1	80.03±0.1	80.08±0.1	25.57	80±0.05	54.42±0.05	1.301±0.0012	0.452±0.01184	12.87±0.3386	1.002±0.02635
12.37±0.01	0.159±0.001	1.967±0.01247	80.02±0.1	79.91±0.1	80.08±0.1	80.1±0.1	25.59	80.03±0.05	54.44±0.05	1.301±0.0012	0.6662±0.01253	18.97±0.3589	1.476±0.02793
13.33±0.01	0.171±0.001	2.28±0.01344	79.99±0.1	79.88±0.1	80.09±0.1	80.06±0.1	25.6	80.01±0.05	54.4±0.05	1.3±0.0012	0.9797±0.01349	27.91±0.3876	2.172±0.03016
15.58±0.01	0.2±0.001	3.115±0.0157	79.98±0.1	79.81±0.1	80.2±0.1	79.96±0.1	25.67	79.99±0.05	54.31±0.05	1.298±0.0012	1.817±0.01575	51.86±0.4556	4.036±0.03546
18.56±0.01	0.238±0.001	4.417±0.01871	79.97±0.1	79.76±0.1	80.36±0.1	79.87±0.1	25.83	79.99±0.05	54.16±0.05	1.294±0.0012	3.122±0.01875	89.37±0.5481	6.955±0.04265
18.22±0.01	0.233±0.001	4.245±0.01837	79.98±0.1	79.77±0.1	80.31±0.1	79.89±0.1	25.78	79.99±0.05	54.21±0.05	1.295±0.0012	2.95±0.01841	84.34±0.537	6.564±0.04179
15.3±0.01	0.196±0.001	3±0.01543	79.98±0.1	79.84±0.1	80.19±0.1	79.99±0.1	25.7	80±0.05	54.3±0.05	1.298±0.0012	1.702±0.01548	48.58±0.4474	3.781±0.03482
13.89±0.01	0.178±0.001	2.472±0.014	79.96±0.1	79.86±0.1	80.11±0.1	80.02±0.1	25.64	79.99±0.05	54.35±0.05	1.299±0.0012	1.173±0.01405	33.44±0.4045	2.603±0.03148
12.73±0.01	0.163±0.001	2.074±0.01283	79.99±0.1	79.9±0.1	80.09±0.1	80.08±0.1	25.65	80.01±0.05	54.37±0.05	1.299±0.0012	0.7751±0.01289	22.1±0.3698	1.72±0.02878
11.92±0.01	0.153±0.001	1.824±0.01202	80±0.1	79.88±0.1	80.03±0.1	80.07±0.1	25.62	80±0.05	54.38±0.05	1.299±0.0012	0.5245±0.01208	14.95±0.3459	1.163±0.02692
11.71±0.01	0.15±0.001	1.756±0.0118	80.01±0.1	79.89±0.1	80.04±0.1	80.08±0.1	25.61	80.01±0.05	54.39±0.05	1.3±0.0012	0.4559±0.01186	12.99±0.3394	1.011±0.02642
12.02±0.01	0.154±0.001	1.851±0.01212	80.02±0.1	79.89±0.1	80.03±0.1	80.08±0.1	25.61	80±0.05	54.39±0.05	1.3±0.0012	0.5514±0.01218	15.71±0.3488	1.223±0.02714
11.73±0.01	0.151±0.001	1.77±0.01182	80.02±0.1	79.89±0.1	80.03±0.1	80.07±0.1	25.62	80±0.05	54.38±0.05	1.3±0.0012	0.4709±0.01188	13.42±0.3401	1.044±0.02647
12.71±0.01	0.163±0.001	2.072±0.01282	80.01±0.1	79.9±0.1	80.08±0.1	80.07±0.1	25.63	80.01±0.05	54.38±0.05	1.3±0.0012	0.7726±0.01287	22.02±0.3693	1.714±0.02874
15.41±0.01	0.198±0.001	3.05±0.01553	79.99±0.1	79.85±0.1	80.18±0.1	80.01±0.1	25.69	80.01±0.05	54.32±0.05	1.298±0.0012	1.752±0.01558	50±0.4504	3.891±0.03505
17.87±0.01	0.229±0.001	4.091±0.01801	79.95±0.1	79.78±0.1	80.31±0.1	79.94±0.1	25.76	79.99±0.05	54.23±0.05	1.296±0.0012	2.795±0.01805	79.89±0.526	6.217±0.04093
19.3±0.01	0.247±0.001	4.767±0.01946	79.96±0.1	79.76±0.1	80.42±0.1	79.85±0.1	25.85	79.99±0.05	54.14±0.05	1.294±0.0012	3.473±0.01949	99.42±0.5711	7.737±0.04444
19.89±0.01	0.255±0.001	5.072±0.02005	79.98±0.1	79.76±0.1	80.42±0.1	79.82±0.1	25.89	80±0.05	54.11±0.05	1.293±0.0012	3.779±0.02009	108.3±0.59	8.424±0.04591
18.27±0.01	0.234±0.001	4.275±0.01842	80.02±0.1	79.79±0.1	80.36±0.1	79.88±0.1	25.88	80.01±0.05	54.13±0.05	1.294±0.0012	2.982±0.01846	85.37±0.5394	6.644±0.04198
17.61±0.01	0.225±0.001	3.962±0.01775	79.99±0.1	79.8±0.1	80.29±0.1	79.93±0.1	25.79	80.01±0.05	54.22±0.05	1.296±0.0012	2.667±0.01779	76.23±0.5182	5.933±0.04033

16.02±0.01	0.205±0.001	3.284±0.01615	79.97±0.1	79.8±0.1	80.21±0.1	80±0.1	25.74	79.99±0.05	54.26±0.05	1.297±0.0012	1.987±0.01619	56.77±0.4694	4.418±0.03653
11.69±0.01	0.15±0.001	1.754±0.01179	80.01±0.1	79.9±0.1	80.05±0.1	80.13±0.1	25.67	80.02±0.05	54.36±0.05	1.299±0.0012	0.4547±0.01185	12.97±0.3393	1.009±0.0264
11.64±0.01	0.149±0.001	1.734±0.01173	80.01±0.1	79.9±0.1	80.06±0.1	80.12±0.1	25.66	80.02±0.05	54.36±0.05	1.299±0.0012	0.4347±0.01179	12.4±0.3376	0.9647±0.02627
11.88±0.01	0.152±0.001	1.806±0.01198	79.99±0.1	79.87±0.1	80.03±0.1	80.1±0.1	25.66	80±0.05	54.34±0.05	1.299±0.0012	0.5071±0.01204	14.46±0.3449	1.126±0.02684
11.91±0.01	0.153±0.001	1.822±0.012	79.98±0.1	79.86±0.1	80.01±0.1	80.09±0.1	25.66	79.98±0.05	54.32±0.05	1.298±0.0012	0.5235±0.01206	14.94±0.3459	1.163±0.02692
12.97±0.01	0.166±0.001	2.153±0.01307	79.98±0.1	79.88±0.1	80.06±0.1	80.08±0.1	25.71	80±0.05	54.28±0.05	1.297±0.0012	0.8555±0.01313	24.43±0.3776	1.901±0.02938
15.05±0.01	0.193±0.001	2.905±0.01518	79.98±0.1	79.84±0.1	80.18±0.1	80.03±0.1	25.76	80.01±0.05	54.25±0.05	1.296±0.0012	1.609±0.01522	45.97±0.4404	3.578±0.03427
17.51±0.01	0.224±0.001	3.922±0.01765	79.95±0.1	79.79±0.1	80.32±0.1	79.94±0.1	25.83	80±0.05	54.17±0.05	1.294±0.0012	2.628±0.01769	75.21±0.5157	5.853±0.04013
19.39±0.01	0.248±0.001	4.807±0.01954	79.95±0.1	79.75±0.1	80.43±0.1	79.86±0.1	25.92	80±0.05	54.08±0.05	1.292±0.0012	3.515±0.01958	100.7±0.5745	7.84±0.04471
19.69±0.01	0.252±0.001	4.963±0.01985	79.97±0.1	79.76±0.1	80.44±0.1	79.86±0.1	25.93	80.01±0.05	54.08±0.05	1.292±0.0012	3.67±0.01989	105.2±0.5841	8.186±0.04545
18.52±0.01	0.236±0.001	4.371±0.01867	79.97±0.1	79.75±0.1	80.33±0.1	79.88±0.1	25.83	79.98±0.05	54.15±0.05	1.294±0.0012	3.077±0.01871	88.09±0.5469	6.855±0.04256
17.34±0.01	0.222±0.001	3.85±0.01748	79.98±0.1	79.79±0.1	80.27±0.1	79.94±0.1	25.83	79.99±0.05	54.16±0.05	1.294±0.0012	2.555±0.01752	73.13±0.5106	5.691±0.03973
15.83±0.01	0.202±0.001	3.198±0.01596	80.01±0.1	79.83±0.1	80.24±0.1	79.99±0.1	25.88	80.02±0.05	54.14±0.05	1.294±0.0012	1.904±0.01601	54.52±0.4647	4.243±0.03616
12.06±0.01	0.155±0.001	1.87±0.01216	80.02±0.1	79.9±0.1	80.05±0.1	80.12±0.1	25.73	80.02±0.05	54.29±0.05	1.297±0.0012	0.5723±0.01222	16.34±0.3507	1.272±0.02729
11.92±0.01	0.153±0.001	1.824±0.01202	80.02±0.1	79.91±0.1	80.05±0.1	80.1±0.1	25.76	80.02±0.05	54.26±0.05	1.297±0.0012	0.5274±0.01208	15.06±0.3467	1.172±0.02698
12.84±0.01	0.164±0.001	2.105±0.01294	80±0.1	79.89±0.1	80.07±0.1	80.08±0.1	25.78	80.01±0.05	54.23±0.05	1.296±0.0012	0.8091±0.013	23.12±0.374	1.8±0.0291
15.01±0.01	0.192±0.001	2.882±0.01514	79.97±0.1	79.84±0.1	80.17±0.1	80±0.1	25.84	79.99±0.05	54.16±0.05	1.294±0.0012	1.588±0.01518	45.46±0.4399	3.538±0.03423
17.73±0.01	0.226±0.001	4.006±0.01787	79.99±0.1	79.82±0.1	80.32±0.1	79.92±0.1	25.94	80.01±0.05	54.08±0.05	1.292±0.0012	2.714±0.01791	77.79±0.5231	6.054±0.04071
19.27±0.01	0.246±0.001	4.74±0.01943	79.99±0.1	79.79±0.1	80.44±0.1	79.85±0.1	26	80.02±0.05	54.02±0.05	1.291±0.0012	3.45±0.01946	98.99±0.5715	7.703±0.04448
19.65±0.01	0.252±0.001	4.952±0.01981	80±0.1	79.78±0.1	80.45±0.1	79.85±0.1	26.03	80.02±0.05	53.99±0.05	1.29±0.0012	3.662±0.01985	105.1±0.5839	8.181±0.04544
18.55±0.01	0.238±0.001	4.416±0.01871	80.02±0.1	79.79±0.1	80.36±0.1	79.89±0.1	25.93	80.01±0.05	54.08±0.05	1.292±0.0012	3.123±0.01874	89.51±0.5487	6.966±0.0427
17.45±0.01	0.224±0.001	3.908±0.01759	79.99±0.1	79.79±0.1	80.27±0.1	79.9±0.1	25.89	79.99±0.05	54.1±0.05	1.293±0.0012	2.615±0.01763	74.93±0.5145	5.831±0.04004
16.05±0.01	0.206±0.001	3.305±0.01618	79.99±0.1	79.82±0.1	80.22±0.1	79.97±0.1	25.86	80±0.05	54.14±0.05	1.294±0.0012	2.012±0.01622	57.59±0.4713	4.482±0.03668
11.68±0.01	0.15±0.001	1.752±0.01177	80.03±0.1	79.9±0.1	80.05±0.1	80.11±0.1	25.76	80.02±0.05	54.26±0.05	1.297±0.0012	0.4549±0.01183	13±0.3395	1.011±0.02642
11.87±0.01	0.152±0.001	1.803±0.01196	80.02±0.1	79.89±0.1	80.05±0.1	80.13±0.1	25.76	80.02±0.05	54.26±0.05	1.297±0.0012	0.5068±0.01202	14.48±0.345	1.127±0.02685
11.86±0.01	0.152±0.001	1.802±0.01195	80±0.1	79.88±0.1	80.03±0.1	80.1±0.1	25.77	80±0.05	54.24±0.05	1.296±0.0012	0.5062±0.01201	14.47±0.3449	1.126±0.02684
11.73±0.01	0.151±0.001	1.772±0.01183	79.99±0.1	79.88±0.1	80.02±0.1	80.09±0.1	25.76	80±0.05	54.23±0.05	1.296±0.0012	0.4758±0.01189	13.6±0.3414	1.058±0.02656

REFERENCE

[1] A. Bar-Cohen, "Computer-Related Thermal Packaging at the Millennial Divide," *Electronics Cooling,* 2000.

[2] B. L. Smith and A. Glezer, "The formation and evolution of synthetic jets," *Physics of Fluids*, vol. 10, no. 9, p. 2281, 1998.

[3] "http://www3.villanova.edu/latfs/research/res02a.html." .

[4] R. G. Bryant, R. T. Effinger, I. Aranda, B. M. Copeland, E. W. Covington, and J. M. Hogge, "Radial Field Piezoelectric Diaphragms," *Journal of Intelligent Materials Systems and Structures*, vol. 15, no. 7, pp. 527–538, Jul. 2004.

[5] K. Mossi and R. Bryant, "CHARACTERIZATION OF PIEZOELECTRIC ACTUATORS FOR FLOW CONTROL OVER A WING," no. June, pp. 14–16, 2004.

[6] K. Mossi and R. Bryant, "Piezoelectric Actuators for Synthetic Jet Applications," *Mat. Res. Soc. Symp. Proc. Vol. 785 © 2004 Materials Research Society D11.8.1*, vol. 785, pp. 1–6, 2004.

[7] M. Hyer, M., and Schultz, "A Morphing Concept Based on Unsymmetric Composite Laminates and Piezoceramic MFC Actuators (AIAA)," *AIAA*, vol. 2004–1806, 2004.

[8] K. M. Mossi, G. V Selby, and R. G. Bryant, "Thin-layer composite unimorph ferroelectric driver and sensor properties," no. April, pp. 39–49, 1998.

[9] F.-J. Chen and G. B., "Virtual Shaping of a Two-dimensional NACA 0015 Airfoil Using Synthetic Jet Actuator," pp. 1–11, 2002.

[10] R. Chen, F., Yao, C., Beeler, G., Bryant, R., and Fox, "Development of synthetic jet actuators for active flow control at NASA Langley (AIAA)," *AIAA*, vol. 2000–2405, 2000.

[11] N. Paul, "Non-Road Cooling System Design," in *Agricultural Equipment Technology Conference Atlanta, Georgia , USA*, 2011.

[12] R. Mahalingam, N. Rumigny, and A. Glezer, "Thermal Management Using Synthetic Jet Ejectors," *IEEE Transactions on Components and Packaging Technologies*, vol. 27, no. 3, pp. 439–444, Sep. 2004.

[13] M. J. Lighthill, "Acoustic streaming," *J. Sound Vib.*, 1978.

[14] A. James, R. D., Jacobs, J. W. & Glezer, "A Round Turbulent Jet Produced by an Oscillating Diaphragm," *Phys. Fluids,* 1996.

[15] A. G. Barton L Smith, "Vectoring and small-scale motions effected in free shear flows using synthetic jet actuators," *AIAA Journal*, p. 213, 1997.

[16] A. B. C. A. W. Cary L. D. Kral, J. F. Donovan, "Numerical simulation of synthetic jet actuators," *AIAA Journal*, vol. 97–1824, p. 15, 1997.

[17] A. G. B L Smith, M A Trautman, "Controlled interactions of adjacent synthetic jets," *AIAA Journal*, 1999.

[18] B. Smith and G. Swift, "Synthetic jets at large Reynolds number and comparison to continuous jets," *15th AIAA Computational Fluid Dynamics Conference*, pp. 1–19, Jun. 2001.

[19] D. S. Kercher, O. Brand, M. G. Allen, and a. Glezer, "Microjet cooling devices for thermal management of electronics," *IEEE Transactions on Components and Packaging Technologies*, vol. 26, no. 2, pp. 359–366, Jun. 2003.

[20] J. Maddox, P. Mane, K. Mossi, and R. Bryant, "PIEZOELECTRIC SYNTHETIC JETS AS VIRTUAL," in *10th International Conference on New Actuators*, 2006, no. June, pp. 14–16.

[21] Y. Liang, Y. Kuga, and M. Taya, "Design of membrane actuator based on ferromagnetic shape memory alloy composite for synthetic jet applications," *Sensors and Actuators A: Physical*, vol. 125, no. 2, pp. 512–518, Jan. 2006.

[22] R. G. Bryant, R. L. Fox, J. T. Lachowicz, and F. Chen, "Piezoelectric Synthetic Jets for Aircraft Control Surfaces," vol. 3674, no. March, 1999.

[23] H. Nagib, J. Kiedaisch, D. Greenblatt, I. Wygnanski, and A. Hassan, "Effective Flow Control for Rotorcraft Applications at Flight Mach Numbers Hassan Nagib 31 st AIAA Fluid Dynamics Conference & Exhibit 11-14 June 2001 / Anaheim , CA EFFECTIVE FLOW CONTROL FOR ROTORCRAFT APPLICATIONS AT," *AIAA 2001-2974*, no. June, 2001.

[24] M. Sheplak, R. Holman, L. Cattafesta, Q. Gallas, B. Carroll, and T. Nishida, "Lumped Element Modeling of Piezoelectric-Driven Synthetic Jet Actuators," *AIAA Journal*, vol. 41, no. 2, pp. 240–247, 2003.

[25] Y. Utturkar, R. Mittal, P. Rampunggoon, and L. Cattafesta, "Sensitivity of synthetic jets to the design of the jet cavity," *40th AIAA Aerospace Sciences Meeting & Exhibit*, Jan. 2002.

[26] C. Seeley, M. Arik, R. Hedeen, T. Wetzel, Y. Utturkar, and M.-Y. Shih, "Coupled Acoustic and Heat Transfer Modeling of a Synthetic Jet," *47th AIAA/ASME/ASCE/AHS/ASC Structures, Structural Dynamics, and Materials*

*Conference
 14th AIAA/ASME/AHS Adaptive Structures Conference
 7th*, no. May, pp. 1–13, May 2006.

[27] K. Navaratnam, D.-D. Lee, and S. Parameswaran, "Application of a Novel Moving-Grid Methodology to Model the Interaction of a Synthetic Jet with a Turbulent Boundary Layer," *Numerical Heat Transfer, Part B: Fundamentals*, vol. 49, no. 2, pp. 105–123, Aug. 2006.

[28] M. Arik, "Local Heat Transfer Coefficients of a High-Frequency Synthetic Jet during Impingement Cooling over Flat Surfaces," *Heat Transfer Engineering*, vol. 29, no. Taylor & Francis, pp. 763–773, Sep. 2008.

[29] P. K. and L. D. M. El-Alti, V. Chernoray, "Experimental Investigation of a Simple Synthetic Jet actuator for active flow control purposes," 2009.

[30] D. a. Lockerby, P. W. Carpenter, and C. Davies, "Is Helmholtz Resonance a Problem for Micro-jet Actuators?," *Flow, Turbulence and Combustion*, vol. 78, no. 3–4, pp. 205–222, Feb. 2007.

[31] D. C. Durán and O. D. López, "Computational Modeling of Synthetic Jets," *COMSOL Conference, Boston*, 2010.

[32] G. Krishnan and K. Mohseni, "An Experimental and Analytical Investigation of Rectangular Synthetic Jets," *Journal of Fluids Engineering*, vol. 131, no. 12, p. 121101, 2009.

[33] G. Krishnan and K. Mohseni, "Axisymmetric Synthetic Jets: An Experimental and Theoretical Examination," *AIAA Journal*, vol. 47, no. 10, pp. 2273–2283, Oct. 2009.

[34] M. Chaudhari, B. Puranik, and A. Agrawal, "Heat transfer characteristics of synthetic jet impingement cooling," *International Journal of Heat and Mass Transfer*, vol. 53, no. 5–6, pp. 1057–1069, 2010.

[35] M. Chaudhari, G. Verma, B. Puranik, and A. Agrawal, "Frequency response of a synthetic jet cavity," *Experimental Thermal and Fluid Science*, vol. 33, no. 3, pp. 439–448, Mar. 2009.

[36] D. Jagannatha, R. Narayanaswamy, and T. T. Chandratilleke, "Analysis of a Synthetic Jet-Based Electronic Cooling Module," *Numerical Heat Transfer, Part A: Applications*, vol. 56, no. 3, pp. 211–229, Aug. 2009.

[37] M. Jain, B. Puranik, and A. Agrawal, "A numerical investigation of effects of cavity and orifice parameters on the characteristics of a synthetic jet flow," *Sensors and Actuators A: Physical*, vol. 165, no. 2, pp. 351–366, Feb. 2011.

[38] P. Valiorgue, T. Persoons, A. McGuinn, and D. B. Murray, “Heat transfer mechanisms in an impinging synthetic jet for a small jet-to-surface spacing,” *Experimental Thermal and Fluid Science*, vol. 33, no. 4, pp. 597–603, Apr. 2009.

[39] T. Persoons, “General Reduced-Order Model to Design and Operate Synthetic Jet Actuators,” *AIAA Journal*, vol. 50, no. 4, pp. 916–927, Apr. 2012.

[40] T. Persoons, A. Mcguinn, and D. B. Murray, “A general correlation for the stagnation point Nusselt number of an axisymmetric impinging synthetic jet,” *International Journal of Heat and Mass Transfer*, vol. 54, no. 17–18, pp. 3900–3908, Aug. 2011.

[41] R. Rusovici, C. Offord, and C. Phelps, “A Coupled Field Finite Element Modeling Procedure for Design of a Synthetic-Jet Actuators,” *Journal of Intelligent Material Systems and Structures*, vol. 22, no. 2, pp. 161–173, Jan. 2011.

[42] M. Arik and T. Icoz, “Predicitng Heat Transfer from Unsteady Synthetic Jets,” *Journal of Heat Transfer*, vol. doi:10.111, p. 134(8), 2012.

[43] V. Tesař and J. Kordík, “Transition in synthetic jets,” *Sensors and Actuators A: Physical*, vol. 187, pp. 105–117, Nov. 2012.

[44] Z. Trávníček, V. Tesař, & Z. B., and K. Peszyński, “Annular Impinging Jet Controlled by Radial Synthetic Jets,” no. August, pp. 37–41, 2014.

[45] X. U. Yang, F. Lihao, Y. Xu, and L. Feng, “Influence of orifice-to-wall distance on synthetic jet vortex rings impinging on a fixed wall,” *Science China Technological Sciences*, vol. 56, no. 7, pp. 1798–1806, May 2013.

[46] A. Eastman, M. Kimber, A. Hirata, and G. Kamitani, “Thermal analysis of a low flow piezoelectric air pump,” *International Journal of Heat and Mass Transfer*, vol. 55, no. 9–10, pp. 2461–2471, Apr. 2012.

[47] M. Arik, R. Sharma, J. Lustbader, and X. He, “Steady and Unsteady Air Impingement Heat Transfer for Electronics Cooling Applications,” *Journal of Heat Transfer*, vol. 135, no. 11, p. 111009, Sep. 2013.

[48] Y. Yu, T. W. Simon, M. Zhang, T. Yeom, M. T. North, and T. Cui, “Enhancing heat transfer in air-cooled heat sinks using piezoelectrically-driven agitators and synthetic jets,” *International Journal of Heat and Mass Transfer*, vol. 68, pp. 184–193, Jan. 2014.

[49] D. Luca, N. Federico, and D. Ingegneria, “Modeling and Experimental Validation of the Frequency Response of Synthetic Jet Actuators1`,” *AIAA Journal*, vol. 52, no. 8, pp. 1733–1748, 2014.

[50] O. Ghaffari, M. B. Dogruoz, and M. Arik, “An investigation into momentum and temperature fields of a meso-scale synthetic jet,” in *Fourteenth Intersociety*

Conference on Thermal and Thermomechanical Phenomena in Electronic Systems (ITherm), 2014, pp. 889–896.

[51] O. Ghaffari, M. B. Dogruoz, M. Arik, and S. Jose, "An Investigation Into Momemtum And Temperature Fields of a Meso-Sale Slot Synthetic Jet for a small jet-to-surface spacing," in *Proceedings of the 15th International Heat Transfer Conference, IHTC-15*, 2014, no. Kyoto, Japan, pp. 1–12.

[52] M. Ikhlaq, O. Ghaffari, and M. Arik, "Effect of Actuator Deflection on Heat Transfer for Low and High Frequency Synthetic Jets," in *Thermal and Thermomechanical Phenomena in Electronic Systems (ITherm), 2014 IEEE Intersociety Conference*, 2014, pp. 882 – 888.

[53] and M. S. Suryanarayana A. N. Prasad, Quentin Gallas, Stephen Horowitz, Brian Homeijer, Bhavani V. Sankar, Louis N. Cattafesta, "Analytical Electroacoustic Model of a Piezoelectric Composite Circular Plate," *AIAA*, vol. 44, no. 10, pp. 2311–2318, 2006.

[54] S. Structures, "ME 493 Introduction to Smart Structures and Materials, SPRING 2011, METU, Ankara Dr. Gökhan O. ÖZGEN," pp. 1–13, 2011.

[55] K. Chandrashekhara, *Theory of Plates*. .

[56] R. D. Belvins and F. Krieger, Malabar, *Formulas for Natural Frequency and Mode Shapes*. 1995.

[57] Q. Gallas, "On the Modeling and Design of Zero-Net Mass Flux Actuators," 2005.

[58] E. Buckingham, "Illustrations Of The Dimensional Equations," in *On Physically Similar Systems*, 1914, pp. 345–376.

[59] "http://www.comsol.com/showcase/mems." .

[60] *ANSYS, User's Guide, Fluent v14.5, Canonsburg, PA, (2012)*. .

[61] M. S. Kang, a. B. Stanbridge, T. G. Changh., and H. S. Kim, "Measuring Mode Shapes With a Continuously Scanning Laser Vibrometer —Hilbert Transform Approach," *Mechanical Systems and Signal Processing*, vol. 16, no. 2–3, pp. 201–210, Mar. 2002.

[62] "http://www.lb-acoustics.at/lb-acoustics_de/wp-content/uploads/2014/06/vibsoft.pdf." .

[63] "http://www.rfcafe.com/references/electrical/sinewave-voltage-conversion.htm." .

[64] "Lab View 2013, National Instruments, Inc., 2103." .

[65] R. J. Moffat, “Describing the uncertainties in experimental results,” *Experimental Thermal and Fluid Science*, vol. 1, no. 1, pp. 3–17, Jan. 1988.

[66] “http://www.ima.org.uk/viewItem.cfm-cit_id=383396.html.” .

[67] D. K. Kurihara, Kiyoshi, Masaaki Fujisaki, “United States Patent Fujisaki et al. Patent N0.: (45) Date of Patent: US 8,596,998 B2 Dec. 3, 2013,” 2013.

[68] M. Arik and T. Icoz, “Predicting Heat Transfer From Unsteady Synthetic Jets,” *Journal of Heat Transfer*, vol. 134(8), 08, no. ASME, pp. 081901–8, 2012.

[69] J. Garg, M. Arik, S. Weaver, and S. Saddoughi, “Micro Fluidic Jets for Thermal Management of Electronics,” in *Volume 4*, 2004, no. San Francisco, California, USA, pp. 647–654.

[70] D. P. D. Theodore L. Bergman, Adrienne S. Lavine, Frank P. Incropera, *Fundamentals of Heat and Mass Transfer*, Sixth edit. Jhon Wiley and Sons, 2011.

[71] S. A. Solovitz and M. Arik, “Understanding the performance metrics for advanced cooling methodologies,” in *2010 12th IEEE Intersociety Conference on Thermal and Thermomechanical Phenomena in Electronic Systems*, 2010, pp. 1–7.